MICROCOPY RESOLUTION TEST CHART

NATIONAL BUREAU OF STANDARDS-1963-A

AFWAL-TR-86-2060

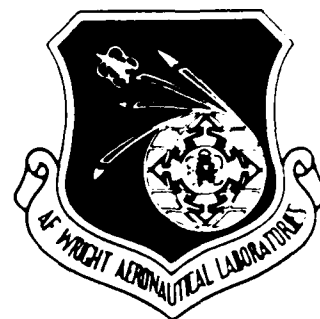# EVALUATION OF IMPROVED ENGINE COMPARTMENT OVERHEAT DETECTION TECHNIQUES

R. C. FOSTER
C. BARKER
D. W. GOODWIN
V. ROWE
C. E. PORCHER

GENERAL DYNAMICS
Fort Worth Division

AD-A173 960

August 1986
Final Technical Report for Period August 1985 — August 1986

Approved for public release; distribution unlimited

DTIC FILE COPY

AERO PROPULSION LABORATORY
AIR FORCE WRIGHT AERONAUTICAL LABORATORIES
AIR FORCE SYSTEMS COMMAND
WRIGHT-PATTERSON AIR FORCE BASE, OHIO 45433-6563

NOV 1 4 1986
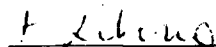
NOTICE

When Government drawings, specifications or other data are used
for any purpose other than in connection with a definitely relat-
ed Government procurement operation, the United States Government
thereby incurs no responsibility nor any obligation whatsoever;
and the fact that the Government may have formulated, furnished,
or in any way supplied the said drawings, specifications, or other
data, is not to be regarded by implication or otherwise as in any
manner licensing the holder or any other person or corporation, or
conveying any rights or permission to manufacture, use, or sell
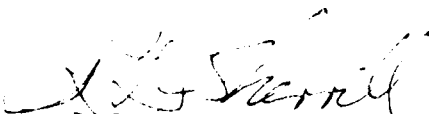any patented invention that may in any way be related thereto.

This report has been reviewed by the Office of Public Affairs
(ASD/PA) and is releasable to the National Technical Information
Service (NTIS). At NTIS, it will be available to the general
public, including foreign nations.

This technical report has been reviewed and is approved for
publication.

P. Liberio   R. Clodfelter
Project Engineer   Chief, Fire Protection Branch

FOR THE COMMANDER

R. Sherrill
Chief, Fuels and Lubrication Division

If your address has changed, if you wish to be removed from our
mailing list, or if the addressee is no longer employed by your
organization please notify AFWAL/POSH, WPAFB, OH 45433 to help
us maintain a current mailing list.

Copies of this report should not be returned unless return is
required by security considerations, contractual obligations,
or notice on a specific document.

REPORT DOCUMENTATION PAGE

REPORT SECURITY CLASSIFICATION UNCLASSIFIED		1b. RESTRICTIVE MARKINGS *A173960*
2a. SECURITY CLASSIFICATION AUTHORITY		3. DISTRIBUTION/AVAILABILITY OF REPORT Approved for Public Release ; Distribution Unlimited
2b. DECLASSIFICATION/DOWNGRADING SCHEDULE		
4. PERFORMING ORGANIZATION REPORT NUMBER(S) FZM-7415		5. MONITORING ORGANIZATION REPORT NUMBER(S) AFWAL-TR-86-2060
6a. NAME OF PERFORMING ORGANIZATION General Dynamics Fort Worth Division	6b. OFFICE SYMBOL (If applicable)	7a. NAME OF MONITORING ORGANIZATION Aero Propulsion Laboratory (AFWAL/POSH)
6c. ADDRESS (City, State and ZIP Code) Fort Worth, Texas 76101		7b. ADDRESS (City, State and ZIP Code) AF Wright Aeronautical Laboratories Wright-Patterson AFB, Ohio 45433-6563
8a. NAME OF FUNDING/SPONSORING ORGANIZATION	8b. OFFICE SYMBOL (If applicable)	9. PROCUREMENT INSTRUMENT IDENTIFICATION NUMBER F33615-85-C-2548

8c. ADDRESS (City, State and ZIP Code)	10. SOURCE OF FUNDING NOS.			
	PROGRAM ELEMENT NO.	PROJECT NO.	TASK NO.	WORK UNIT NO.
11. TITLE (Include Security Classification) Evaluation of Improved Engine Compartment Overheat Detection Techniques	62203F	3048	07	04

12. PERSONAL AUTHOR(S)
R. C. Foster, C. Barker, D. W. Goodwin, V. Rowe, C. E. Porcher

13a. TYPE OF REPORT Final	13b. TIME COVERED FROM 8/1985 TO 8/1986	14. DATE OF REPORT (Yr., Mo., Day) 1986 August	15. PAGE COUNT 162

16. SUPPLEMENTARY NOTATION

17	COSATI CODES		18. SUBJECT TERMS (Continue on reverse if necessary and identify by block number)
FIELD	GROUP	SUB. GR.	Aircraft Overheat Detection, Infrared Detection,
17	05		Bleed Air Leaks, Engine Nacelle

19. ABSTRACT (Continue on reverse if necessary and identify by block number)

A study was conducted to evaluate the feasibility of utilizing infrared
(IR) sensor technology to detect leaks from failed aircraft bleed ducts.
Improved overheat detection system requirements were defined and detection
concepts were formulated based on these requirements. An IR detection
concept was shown to exhibit potential for improvement over other concepts
formulated and existing cable type detection elements. A nacelle/bleed
duct simulator was designed and fabricated in order to conduct tests of IR
detection concepts. Radiation detection instrumentation was designed for
installation in the nacelle/bleed duct simulator. Tests were conducted
utilizing the IR instrumentation and a Systron-Donner element to detect
simulated bleed leaks at three different flight conditions. The test data
(Continued)

20. DISTRIBUTION/AVAILABILITY OF ABSTRACT	21. ABSTRACT SECURITY CLASSIFICATION
UNCLASSIFIED/UNLIMITED ☐ SAME AS RPT. ☒ DTIC USERS ☐	UNCLASSIFIED

22a. NAME OF RESPONSIBLE INDIVIDUAL Ms. Patricia Liberio	22b. TELEPHONE NUMBER (Include Area Code) (513) 255-6918	22c. OFFICE SYMBOL AFWAL/POSH

DD FORM 1473, 83 APR   EDITION OF 1 JAN 73 IS OBSOLETE.

19. Abstract (Continued)

was analyzed to evaluate the feasibility of IR detection techniques and the relative performance of the IR techniques with respect to cable-type elements was determined.

SUMMARY

The requirements for improved overheat detection systems were formulated. Requirements considered functional, environmental, maintainability, and reliability aspects of system design and 10 separate requirements were identified. Four concepts were formulated, including one based on the use of infrared (IR) detection, and the concepts were evaluated and compared to currently used Systron-Donner cable-type elements. The IR detection concept was deemed to exhibit potential for improvement over the other concepts identified and cable-type elements based on this evaluation. A computer model was developed to define detection requirements for IR detectors from evaluation of the radiation exchange within a nacelle/bleed duct enclosure.

A bleed duct/nacelle simulator was designed and constructed based on a typical F-111 aircraft nacelle configuration. The nacelle incorporated a simulated engine case surface, simulated internal fuel tank surface, and a 2.0-inch bleed duct. A 0.25-inch-diameter hole was drilled into the wall of the bleed duct to simulate a failed/cracked bleed duct. The nacelle also incorporated provisions for simulation of various leakage flowrates and nacelle airflows corresponding to the flight condition of interest. Provisions were also provided to allow installation of IR radiation detection instrumentation in the nacelle simulator.

Radiation detection instrumentation was developed by HTL K West Systems to evaluate the feasibility of utilizing IR sensor technology to detect bleed duct air leaks. The instrumentation consisted of three separate packages, two packages containing four individual sensors each and one package with a single sensor. The sensors incorporated different types of sensing elements, selective filtering to limit the detected radiation to specific wavelength bands, and specified fields of view.

Simulated bleed leak tests were conducted in the nacelle/ bleed duct simulator discussed in the previous paragraph. Bleed leaks and nacelle flow conditions were simulated for three different conditions: ground static (idle power), M=0.75 (40.0K ft.), and M=1.2 (sea level). Leak detectability was evaluated for these conditions utilizing both IR radiation detection instrumentation and the cable type overheat detection element, manufactured by Systron-Donner, installed in the F-111 engine nacelle.

We concluded that the detection of bleed leaks utilizing IR technology is feasible and offers enhanced area coverage over currently used cable type detection elements. In addition, we recommend that a prototype IR overheat detection system be developed and evaluated to verify its detection capability in a realistic nacelle environment.

FOREWORD

This report documents an experiment to evaluate the feasibility of utilizing infrared (IR) sensor technology to detect leaks from failed or leaking aircraft bleed air ducts. The research was performed by conducting tests, with IR instrumentation, of simulated bleed leak conditions in a bleed duct/ nacelle test fixture which simulated F-111 aircraft characteristics.

TABLE OF CONTENTS

TABLE OF CONTENTS (Cont'd)

LIST OF FIGURES

LIST OF FIGURES (CONT'D)

LIST OF FIGURES (CONT'D)

LIST OF FIGURES (CONT'D)

LIST OF FIGURES (CONT'D)

LIST OF TABLES

SECTION 1

INTRODUCTION

The detection of fire and overheat conditions (resulting from leaks from failed bleed ducts) in aircraft engine nacelles is essential to insure satisfactory aircraft operational capability. Present-day aircraft engine compartment detection systems utilize the thermally sensitive elements. One type of cable system relies on changing electrical resistance as a function of temperature to trigger the appropriate warning mechanism. A later generation of cable elements uses pneumatic principles to indicate increasing temperature. Both types of cable systems rely on convective and conductive heat transfer to achieve their detection threshold level, thus the systems must be installed in the immediate area where the temperature increase (for example from a fire) is occurring. This can lead to excessive detector response times since a fire may have to exist or even grow in size over a long period of time before the thermal cable can sense the fire. Not only can this lead to overwhelming damage (which many times leads to loss of the aircraft), but may be one reason why a large number of fires are undetected. Furthermore, many of the cables are susceptible to false alarms and are therefore a burden to the required maintenance activities in the engine compartment. When these thermal cables are used as overheat detector systems, the operational problems can be even more severe. Even though the output signal is adjusted to trigger at a lower temperature, an overheat condition can result from such small leaks that to sense the hazard the cable must be even closer to the source of the leak than when used as a fire detector. Thus, the aircraft designer must be able to identify (almost to the nearest inch) where the most damaging overheat conditions may develop. The thermal-sensing cable can then be routed into these areas, assuming it is compatible with the aircraft engine installation.

A significant advancement in fire detection technology was achieved through a program sponsored by the AFWAL Aero Propulsion Laboratory and conducted by General Dynamics to develop and flight test a fire detection system using ultra-violet (UV) technology (Reference 1). Successful development and flight testing of the system in the engine bays of an F-111 aircraft demonstrated that UV/microprocessor technology can provide significant advancements over existing thermal-cable-type fire detectors. The UV/micro-processor provides virtually 100 percent optical coverage in the engine bay. In addition, redundancy, fast response, high reliability, and an automatic self-check feature round out the major advancements of the UV/microprocessor system. One of the major shortcomings of this system, however, is that it does not incorporate an overheat detection capability.

To provide complete hazard detection in the engine bay and other critical areas, there remains a need for improved detection of overheat conditions from failed or leaking engine hot air bleed ducts. On some aircraft the thermal-cable-type detectors are also used to detect failures of engine bleed air ducts in critical areas. However, they have experienced limited success because they cannot provide full coverage around the hot air duct. Service experience of the present overheat detection systems on the F-111 (between November 1978 and May 1981) showed that 39 percent (3 out of 8) of the critical overheat conditions were not detected. These incidents resulted in significant structural damage to the aircraft and the potential for loss of the aircraft. Further research and development of an improved overheat detection system is therefore clearly warranted. This study evaluates improved methods of overheat detection with primary emphasis on the utilization of IR sensors/technology. Ultimately, it is envisioned that an optical detection system (fire and overheat) could be developed based on the use of IR sensors for overheat detection and UV technology for fire detection.

IR sensors have been used for a variety of applications, including missile detection of aircraft and temperature measurement applications. The sensors produce an output voltage that is proportional to the irradiance (watts/cm^2) incident upon the sensor plane. The sensitivity of the sensor is strongly dependent on the wavelength band of incident radiation; therefore, sensor elements are selected to give maximum response in the wavelength band of interest.

To detect radiation induced from bleed leaks in aircraft nacelle sections, the bleed-induced irradiance at the detector must exceed the background irradiance of the nacelle/compartment by an amount which is above the minimum sensitivity of the detector element. The background irradiance for a given sensor view orientation is a function of the temperatures of the surroundings (engine case, bleed duct, nacelle wall), the emissivity of the enclosure surfaces, and the geometry of the enclosure surfaces with respect to the sensor. The bleed-induced irradiance is a function of the leak temperature, area and emissivity of surfaces heated by the bleed leak, as well as orientation of the heated surfaces to the detector. Since the background irradiance varies with flight conditions, it is essential that the associated variation in irradiance be evaluated to establish thresholds in order to prevent false alarm indications.

Recent studies (Reference 2) in overheat detection in aircraft nacelle compartments incorporating insulated bleed ducts indicate promising potential for the use of IR detectors to sense overheat conditions.

The application of IR sensor technology to leak detection in the presence of uninsulated bleed ducts, as utilized in the F-111, presents the most severe test of this concept and must be evaluated to ensure proof of concept for aircraft application.

3

Our research was, therefore, directed toward evaluation of IR technology to detect simulated bleed leaks based on F-111 aircraft characteristics. The objectives of the research were to: (1) define improved overheat system requirements and concepts, (2) design and fabricate a bleed duct/nacelle simulator, (3) develop and fabricate IR detection instrumentation (by HTL Systems), (4) conduct tests to evaluate the feasibility of IR detection techniques, and (5) evaluate the performance of IR techniques with respect to conventional overheat detection methods.

SECTION 2

DEFINITION OF IMPROVED OVERHEAT SYSTEM
REQUIREMENTS AND CONCEPTS

The generalized requirements for overheat detection concepts were formulated and are discussed in this section. Concepts are formulated based on these requirements and the relative merits of the concepts, with respect to conventional cable-type elements, are also discussed. In addition, the development of a computer model to predict the radiation exchange within the nacelle/bleed duct simulator is discussed.

2.1 General Requirements

The requirements for bleed leak detection systems were formulated in order to define and evaluate improved leak detection concepts. The following separate requirement categories were identified and are discussed herein:

- o area coverage
- o leak orientation
- o leak size
- o leak temperature
- o installation
- o discrimination
- o reliability
- o maintainability
- o leak location
- o environmental compatibility.

A bleed leak detection system should provide total coverage over the entire area of the nacelle in which bleed air ducts are routed. A total length of 19 ft. of Systron-Donner cable element, for example, is provided in the F-111 aircraft engine nacelle to

5

provide this coverage. While some total coverage is required over large areas such as the nacelle, it would be highly desirable to provide enhanced coverage over smaller areas in which the presence of an undetected leak could result in possible loss of the aircraft. An example of such an area would be the areas of the F-111 fuel tanks which might be exposed to leaks from bleed air ducts.

Potential bleed leak detection concepts should also provide the capability to detect leaks occurring anywhere around the circumference of the bleed duct or, in terms of angular leak orientation, this would correspond to 360 degrees around the bleed duct. This requirement is believed to be the primary "short-coming" of the currently used cable-type elements. These elements will detect leaks which directly impinge upon the element but will not detect leaks which occur at other orientations to the cable elements.

Candidate concepts must also be able to detect leaks of a very small size. The size and configuration of the leakage area may vary considerably, but bleed duct cracks on the order of 0.5 in. by 0.01 in. have been observed (Reference 3). This implies that very small areas of exposure of the detector element must produce a measurable output which may be utilized to activate an overheat detection alarm. The current Systron-Donner element, for reference, requires heating of a 6.0-inch length of the cable to 650 F to initiate the overheat alarm.

The concepts should be able to detect leaks at temperatures which correspond to the minimum bleed temperatures expected for aircraft operation. These temperatures would occur under ground static (idle power) engine operating conditions and would be 400 F for the F-111 aircraft for hot-day conditions. The detection of leaks under ground static conditions is desirable since overheat conditions could be detected and the flight aborted if overheat conditions were detected during ground operations.

6

Potential concepts must also exhibit capability for installation in the engine nacelle compartment. Installation considerations, of course, vary with the particular location in the nacelle, but in general the detector element must be small and compact in order to be installed in the very limited space available in the nacelle area. A primary consideration in the installation is that the installation not impact the capability for removing the engine for periodic maintenance.

Potential concepts should incorporate the capability to distinguish between overheat and fire conditions. The ultimate goal in the general area of overheat/fire detection in aircraft nacelles is to develop a single system that would detect both overheat and fires. This capability is currently provided by three separate Systron-Donner elements in the F-111 nacelle: two fire detection elements and one overheat detection element. This discrimination between overheat and fire conditions is especially important since it will influence the corrective action taken by the pilot. In addition, it would not be advisable to release fire suppressants if an overheat condition exists and be vulnerable to fires at some later time in the flight.

Viable concepts should also exhibit a high degree of reliability. To insure reliable operation of the detector over its operational life, a "self-test" feature should be incorporated for periodic checkout of the detector in a timely manner while in service. This checkout should include provisions whereby signals utilized by the detector to detect an overheat condition may be simulated in the aircraft and monitored to insure satisfactory operation of the system. This self-test feature should be automated for utilization by the pilot as part of the preflight checkout. In addition, the detector should not give an indication of overheat conditions as a result of system malfunctions; i.e. system design should minimize the number of false warnings produced by the detection system.

7

Overheat detection concepts should also exhibit a high degree of maintainability. This implies that the detector should be accessible and easy to maintain. This requirement also implies that the detector should be "nondestructive", i.e. it should not require maintenance or replacement after exposure to overheat conditions. This requirement also implies, in the case of optical detection techniques, that "blockage" of the sensor window by dust, grease, etc. should be a consideration in the evaluation of the concept.

Concepts should also incorporate the capability to identify the location (at least to the compartment level) of the leak. This implies that the specific system employed should use independent sensors to provide coverage over various compartments (nacelle, wheel well, etc.). The coverage of large areas, such as the nacelle, could be divided into zones with a specific element dedicated to each zone.

Improved overheat detection concept must also be capable of satisfying the environmental requirements (temperature, pressure, vibration, etc.) for operation in an aircraft nacelle compartment. The environmental requirements for the current Systron-Donner cable elements are described in Reference 4 and include such categories as altitude, rate of climb, humidity, vibration, mechanical shock, high and low temperature, and temperature shock evaluations. The nacelle air temperature extremes range from +300 F to -60 F while the operating pressures range from 15.3 psia to 0.65 psia. In addition, the rate-of-climb requirements of Reference 4 specify a maximum rate-of-climb of 20,000 ft. per minute. Candidate concepts must, therefore, satisfy a wide range of requirements in order to provide satisfactory operation in the engine nacelle environment.

2.2 Concepts Formulation

Concepts were formulated for improved overheat detection techniques based on the requirements defined in Section 2.1 and are discussed in the following paragraphs.
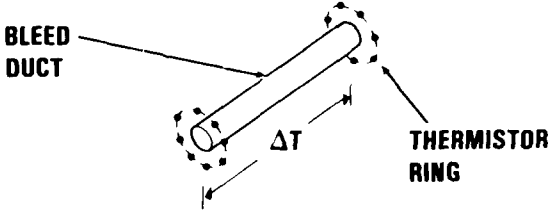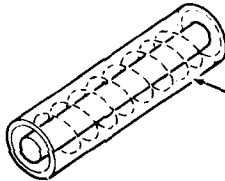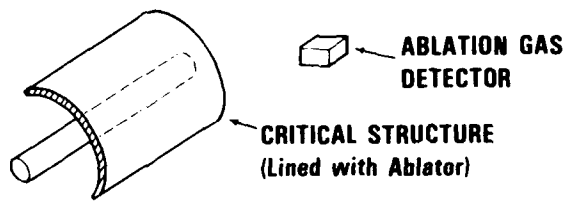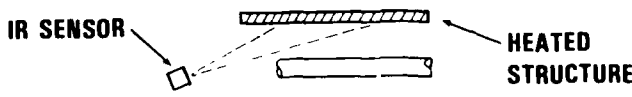
Four concepts were formulated and are presented in Table 1.

The differential temperature concept incorporates two circular rings which are located at a fixed distance apart. Each ring surrounds the bleed duct in question and contains six different thermistors spaced at equal distances around the ring. The concept would be based on detecting the difference between the average temperature of the six thermistors in one ring and the average temperature of the six thermistors in the other ring. Leaks, therefore, initiating at any point between the two rings would increase the temperature of the nacelle flow and generate a detectable signal between the two ring elements. A number of these systems could be installed at critical locations in the nacelle to provide the required coverage.

The electrical resistance concept would incorporate a fine wire imbedded in a matrix material as shown in the sketch of Table 1. The wire and matrix material form a cylindrical element which would surround the bleed duct as shown in the sketch of Table 1. The wire would form an electrical circuit such that a leak initiating anywhere around or along the duct would melt the wire and create a circuit discontinuity which could be monitored to detect the presence of a leak.

The ablative gas concept would incorporate the coverage of critical structure with an ablative material and an ablation gas detector located downstream of the location of the ablator. A leak would cause ablation (transformation of ablation material from a solid to a gas phase) which would be detected by a sensitive gas detector system located downstream of the leak.

TABLE 1.   IMPROVED OVERHEAT DETECTION CONCEPTS.

CONCEPT	DESCRIPTION
DIFFERENTIAL TEMPERATURE	BLEED DUCT / ΔT / THERMISTOR RING
ELECTRICAL RESISTANCE	MATRIX WITH FINE WIRE IMBEDDED
ABLATIVE GAS	ABLATION GAS DETECTOR / CRITICAL STRUCTURE (Lined with Ablator)
IR SENSOR	IR SENSOR / HEATED STRUCTURE

RF 1

10

The IR detection concept would utilize an IR detector to sense a net change in radiation from the structure in the proximity of the leak due to heating of the structure by the leak. The IR detector could incorporate sensing of radiation at discrete wavelengths and limitation of the sensor field-of-view to enhance its detection capability.

The concepts defined in the previous paragraphs and the conventional Systron-Donner element are evaluated with respect to the requirements defined in Section 2.1, and the results of the evaluation are summarized in Table 2. A ($\checkmark$) in Table 1 indicates the requirement is satisfied while an (X) indicates the requirement is not satisfied. This evaluation is necessarily qualitative in nature since only preliminary definition of the concepts was accomplished.

The IR detection concept appears superior to the other concepts formulated in the categories of installation, discrimination, reliability, and maintainability. The differential temperature, electrical resistance, and ablative gas concepts would be very difficult to install for realistic bleed duct applications primarily because of the configuration required to detect leaks at all possible leak orientations. The IR sensor concept should be relatively easy to install, and while it is not expected to provide coverage over all possible orientations of the leak, it is projected to provide coverage over a wide range of possible orientations. None of the three concepts exhibit potential for discriminating between overheat and fire conditions, although the IR concept combined with the UV fire detection system (Reference 1) would seem to exhibit potential for a complete optical detection system. That any of the other three concepts could satisfy the reliability requirement in terms of incorporation of a "self-test" feature is highly improbable. A "self-test" feature was incorporated into the UV system by providing for the input of an artificial radiation signal to the

TABLE 2.   EVALUATION OF OVERHEAT DETECTION CONCEPTS.

DETECTION TECHNIQUE	AREA		ORIENT	LEAK SIZE	LEAK TEMP.	INSTL.	DISC.	REL.	MAINT. (Non Destruct)	LEAK LOCATION	ENVIRON. COMP.
	TOTAL	LIMITED									
• EXISTING											
SYSTRON-DONNER	✓		X	X	X	✓	✓	X	✓	X	✓
• CONCEPTS											
DIFFERENTIAL TEMPERATURE	X	✓	✓	X	✓	X	X	X	✓	✓	✓
ELECTRICAL RESISTANCE		✓	✓	✓	✓	X	X	X	X	✓	✓
ABLATIVE GAS	X	✓	X	✓	✓	X	X	X	X	X	✓
IR SENSOR	X	✓	✓	✓	✓	✓	✓*	✓	✓	✓	?

*Combined with UV Fire Detect System

12

sensor simulating the radiation input from an actual fire. A similar feature could be incorporated into an IR detection system. The electrical resistance and ablative gas concepts do not satisfy the maintainability requirement because they incorporate "destructive" detection techniques and would need to be replaced after detection of a leak.

The IR sensor concept should not require replacement after detection of leak conditions; therefore it exhibits superior potential to the other concepts.

The IR sensor concept also exhibits potential for improvement over the Systron-Donner cable elements in several areas as illustrated in Table 1. Although some improvement is anticipated for the IR sensor concept in terms of leak size and temperature, the primary advantage of the IR concept is believed to be associated with the requirement to detect leaks over a wider range of orientations than is currently capable with the cable-type elements. The cable elements require that the leak impinge directly on the cable for detectability; hence are severely limited in the leak orientations that may be detected. The IR sensor concept, on the other hand, provides coverage over a range of possible leak exposure orientations which is only limited by the sensors field-of-view. The principal concerns for the IR system are: (1) the ability of the sensor to detect small changes in irradiance in the presence of high "background" radiation levels, (2) the number of sensors required to provide coverage over the entire engine nacelle, and (3) the compatibility of the IR sensors with the environmental requirements (temperature, pressure, vibration, etc.) of the engine nacelle.

IR sensors were deemed to exhibit sufficient potential to warrant their evaluation as a detection concept, and this study was directed toward evaluating the feasibility of these devices to detect overheat conditions in a simulated nacelle environment.

2.3 Prediction of Radiation Exchange in Nacelle Enclosure

A numerical model was developed to define the requirements for detection of bleed duct leaks in a nacelle enclosure utilizing IR sensors. The numerical procedure incorporated the capability to predict the change in incident radiation on a detector resulting from a bleed duct leak within the enclosure, based on arbitrary sensor location and characteristics. This procedure was utilized to: (1) provide guidelines for development of the sensors, (2) aid in defining sensor placement within the simulator for the test program, and (3) conduct post-test analysis of the IR detection results.

The numerical procedure was based on predicting the radiant energy exchange within the enclosure by considering the radiation interaction between all surfaces comprising the nacelle enclosure and bleed duct. The numerical code considers the radiative exchange in the simulator facility to be strictly a surface phenomenon problem. The hot air flowing in the nacelle enclosure is assumed to be a nonparticipating medium (medium that does not absorb, emit, or scatter radiation). This is a good assumption since air (with no contaminants) is virtually transparent to thermal radiation in most of the IR spectrum for the operating temperature ranges of the nacelle/bleed duct environment between 100 to 900 F.

The "zone analysis method", described in References (5) and (6) was used in the numerical procedure to investigate the radiative exchange of incoming and outgoing radiation transfer from the surfaces of the nacelle and bleed duct. The outgoing radiative energy leaving the walls of the nacelle and bleed duct depend on the temperature and the radiation properties (emissivity and reflectivity) of the surface. The first task of the numerical procedure is to investigate the radiosity (radiative heat flux leaving defined surface region) of the nacelle and bleed duct

before and after the leaks occurs. The next task in the numerical procedure investigates the change in the irradiance contributed by the simulated hot air leaks, from the bleed duct, that is detectable with the IR sensor. The capability of the IR sensor to detect the radiant energy leaving the walls of the nacelle and bleed duct depends on the location and orientation of the IR sensor in the simulator facility, the field-of-view (FOV), and the band region of detectability in the infrared spectrum. Each of these detector characteristics are considered in the numerical procedure and will be discussed in detail in the following paragraphs.

In using the "zone analysis technique," the nacelle duct and the bleed duct enclosure are defined into a discrete number of rectangular zones. The nacelle/bleed duct enclosure is discussed in Section 3 and is shown schematically in Figure 1. The nacelle enclosure is rectangular (24 in. by 6 in.) in cross section and 10 feet long. It incorporates a 2.0-in.-diameter bleed duct located in the center of the enclosure and spanning the entire length of the enclosure. The bleed duct leak will be located 2.0 ft from one end of the nacelle enclosure and will impinge on the upper surface of the nacelle enclosure. The radiation exchange in the nacelle/bleed duct enclosure was evaluated by developing a radiation model of the enclosure based on the "zone analysis" technique mentioned previously. In using this technique the bleed duct and nacelle are divided into a number of discrete rectangular zones as shown in Figure 1. The nacelle is divided into five sections along its length, each section being 2.0 feet in length. The first four sections are identical and consist of six zones each: four zones represent the top and bottom surface (each 2 ft by 1.0 ft), and two zones represent the side walls of the enclosure. The section located directly above the leak is divided differently to incorporate a fine zone size on the upper surface which will be heated by the leak. The upper surface of this section, in the area directly above the leak, is divided into 36 zones with each zone being 1.0 inch by 1.0 inch. The remainder of
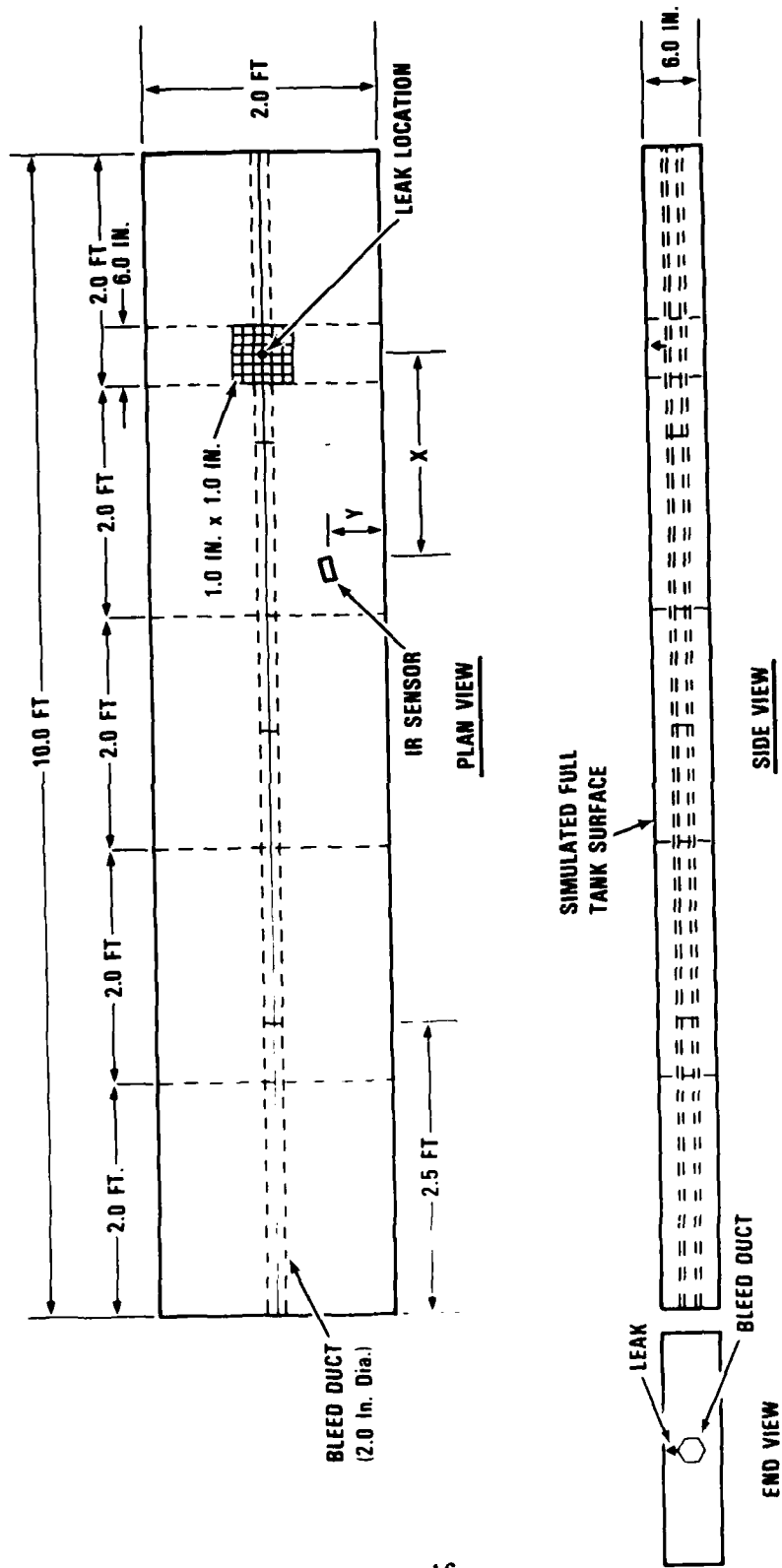
Figure 1. Nacelle/bleed duct radiation analysis configuration.

16

the upper surface in this section consists of four zones: two
identical zones adjacent to the leak area with dimensions of 6.0
inches by 9.0 inches and two zones with dimensions of 18.0 inches
by 12.0 inches. Each side wall of this section is divided into
two zones: one zone with dimensions of 6.0 inches by 6.0 inches
and one zone with dimensions of 6.0 inches by 18.0 inches. The
bottom surface of this section is divided into four zones: two
zones with dimensions of 18.0 inches by 12.0 inches and two zones
with dimensions of 6.0 inches by 12.0 inches. Each end section
(24.0 in. by 6 in.) of the simulator was also defined as two
discrete zones. The nacelle simulator was, therefore, divided
into 36 small zones (1.0 in. by 1.0 in.) and 40 larger zones for a
total of 76 discrete zones. The 2.0-inch-diameter bleed duct was
also divided into a number of discrete zones. The total duct
length of 10 feet was divided into four sections, the length of
each section being 2.5 feet. The circular cross section of the
duct was approximated by six rectangular facets, each facet
representing a discrete zone. The bleed duct, therefore, was
divided into 24 zones. The nacelle/bleed duct enclosure was
therefore divided into 100 individual zones to formulate the
radiation exchange within the enclosure.

To significantly simplify the analysis of the radiative heat
exchange in the nacelle/bleed duct enclosure the following
assumptions are made for each zone surface:

   o Zone surfaces are opaque.
   o Surfaces are diffuse emitters and reflectors.
   o Temperature and radiosity are spatially uniform within
      each zone.
   o Radiative properties are spatially uniform and
      independent of direction.
   o The enclosure is filled with a nonparticipating medium
      (For this problem: hot nacelle and bleed duct air).

At certain regions in the nacelle/bleed duct simulator, a

17

large variation in the temperature and surface properties from point-to-point along a small area of the surface is expected. The spatial variation in the radiosity will be nonuniform in distribution in that region. The zone analysis method assumes the temperature and radiation properties to be spacially uniform within each zone, but can vary across the different zones. To consider an accurate analysis of the nonuniform radiosity distribution, the region must be defined into a fine grid of zones. The top surface of the nacelle duct, as shown in Figure 1, has a small region where there is a large temperature gradient produced by the hot air impingement from the simulated bleed duct leak. Therefore, this hot air impingement region of the nacelle surface is divided into 36 small zones as mentioned previously, each zone having an area of one square inch.

Another assumption considered in the numerical procedure, is that the nongray radiation properties (surface reflectivity or surface emissivity) of the nacelle and bleed duct facility can be defined by the multiband rectangular box model. The band model assumes the spectral region of the infrared spectrum, in which the IR sensor can detect thermal radiation, can be broken up into a smaller number of wavelength bands $\Delta\lambda_K$, k=1,2,3 ..., such that the radiation properties are defined uniformly over each band.

With the above conditions defined in this problem, the radiosity ($R_{i,k}$) or the outgoing radiative heat flux leaving a zone surface (i) in a wavelength band region (k) is defined as:

$$R_{i,k}(\vec{r}_i) = \epsilon_{i,k} \pi I_{b,k}(T_i(\vec{r}_i)) + \rho_{i,k} \sum_{j=1}^{N} R_{j,k}(\vec{r}_j) F_{Ai-Aj} \qquad (1)$$

where $\epsilon_{i,k}$ is the surface emissivity, $\rho_{i,k}$ is the surface reflectivity, and $I_{b,k}$ is the Planck's Black body intensity.

The determination of the radiosity in equation (1) consists of evaluating the radiative heat flux diffusely emitted from the surface and the incident radiative heat flux diffusely reflected from the surface. The incident radiative heat flux that is reflected from a specified zone depends on knowing the fraction of the radiosity, leaving the other zones, that will be incident upon the specified zone. This is accomplished by evaluating the radiation view factor between individual zones.

The view factor F_{Ai-Aj} is defined in general terms as the fraction of the diffuse uniform radiative energy leaving a zone surface (i) that strikes another zone surface (j). The view factors of all the enclosure must be evaluated, so that the incident radiative heat flux entering each zone can be determined.

With the view factors describing every possible radiative exchanges between the surfaces calculated, the radiosities for a total of N zones describing the nacelle/bleed duct enclosure can be evaluated by solving N linear radiosity equations in the form:

$$\sum_{j=1}^{N} \left(\frac{\delta_{ij} - \rho_{i,k} F_{Ai-Aj}}{\pi \epsilon_{i,k}} \right) R_{j,k} = I_{b,k}(T_i) \qquad (2)$$

for i=1.2.3 .... .N

where,

$$\delta_{ij} = \begin{cases} 1 & \text{for } i = j \\ 0 & \text{for } i \neq j \end{cases}$$

Equation (2) can be written in matrix form as,

$$[M][R] = [I_b] \qquad (3)$$

And using a matrix inversion method to solve for $[M]^{-1}$, the

19

radiosities $R_{i,k}$ are then evaluated from:

$$[R] = [M]^{-1}[I_b] \qquad (4)$$

The view factor F_{Ai-Aj} defined from a rectangular zone surface (i) to another rectangular zone surface (j), for an arbitrary location and orientation on the simulator facility is illustrated in Figure 2 and can be numerically evaluated by investigating the elemental view factors $dF_{dAi-dAj}$. The elemental view factor $dF_{dAi-dAj}$ by definition is defined as the ratio of radiative energy leaving the surface element dA_i that hits surface element dA_j divided by the total amount of radiative energy leaving surface dA_i in all directions. For a diffuse surface, the elemental view factor is defined as:

$$dF_{dAi-dAj} = \frac{dQ_i}{Q_i} = \frac{\cos\theta_i \cos\theta_j}{\pi r_{ij}^2} dA_j \qquad (5)$$

which depends on only the geometric parameters described in Figure 2.

The view factor F_{Ai-Aj} is evaluated by integrating the elemental view factor over the surface area of zone (i) and zone (j) or:

$$F_{Ai-Aj} = \frac{1}{A_i} \int_{Ai} \int_{Aj} dF_{dAi-dAj} dA_i \qquad (6)$$

$$= \frac{1}{A_i} \int_{L2i} \int_{L1i} \int_{L2j} \int_{L1j} \frac{\cos\theta_i \cos\theta_j}{\pi r_{ij}^2} \qquad (7)$$

$$\times dL2j \, dL1j \, dL2i \, dL1i$$

The configuration factor in equation (7) is numerically integrated across the lengths of the rectangular sides of both zone surfaces

20
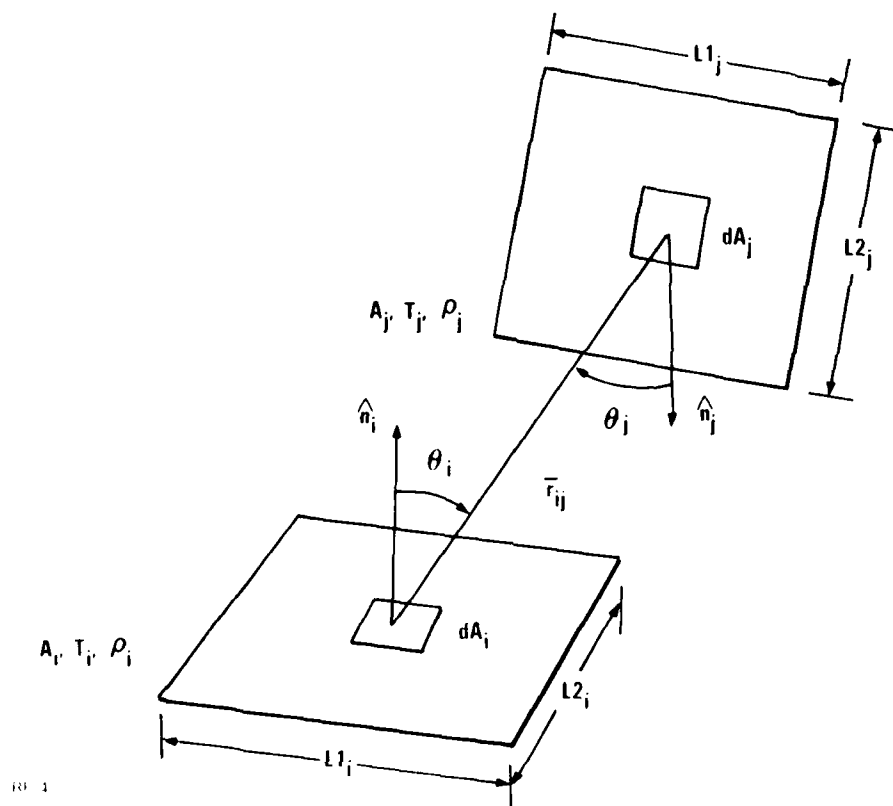
Figure 2. Radiation view factor configuration.

by applying the 10-point Guassian Quadrature Method (Reference 7).

This numerical procedure requires a considerable amount of computer time, since it requires the integration of 10,000 different elemental view factors to find one view factor F_{Ai-Aj} from zone surface (i) to zone surface (j). With the application of the reciprocity relation,

$$A_j F_{A_j} - A_i = A_i F_{A_i} - A_j \qquad (8)$$

the computational time was reduced by factor of two. The time it required to numerically investigate the hundred view factors describing radiative exchange for the entire nacelle/bleed duct enclosure was over 10 hours of execution time on the VAX 8600 computer system.

The important advantage in using this numerical view factor procedure is its accuracy in evaluating the configuration factor between two zone surfaces (i) and (j) that are being partially blocked by another surface as shown in Figure 3. With the bleed duct placed in the middle of the nacelle enclosure, many zone surfaces on the nacelle duct are being partially or completely obstructed from one another. To investigate the configuration factor between two zones with surface obstruction, the elemental view factors evaluated in the integration procedure would either be:

$$dF_{dAi-dAj} = \begin{cases} 0 & \text{(Blocked)} \\ \dfrac{\cos \theta_i \cos \theta_j}{\pi r_{ij}^2} dA_j & \text{(Not Blocked)} \end{cases} \qquad (9)$$

To examine if the elemental surfaces, dAi and dAj, are being blocked by another surface, the point of intersection on the plane of the obstructing surface is first determined. The inter-
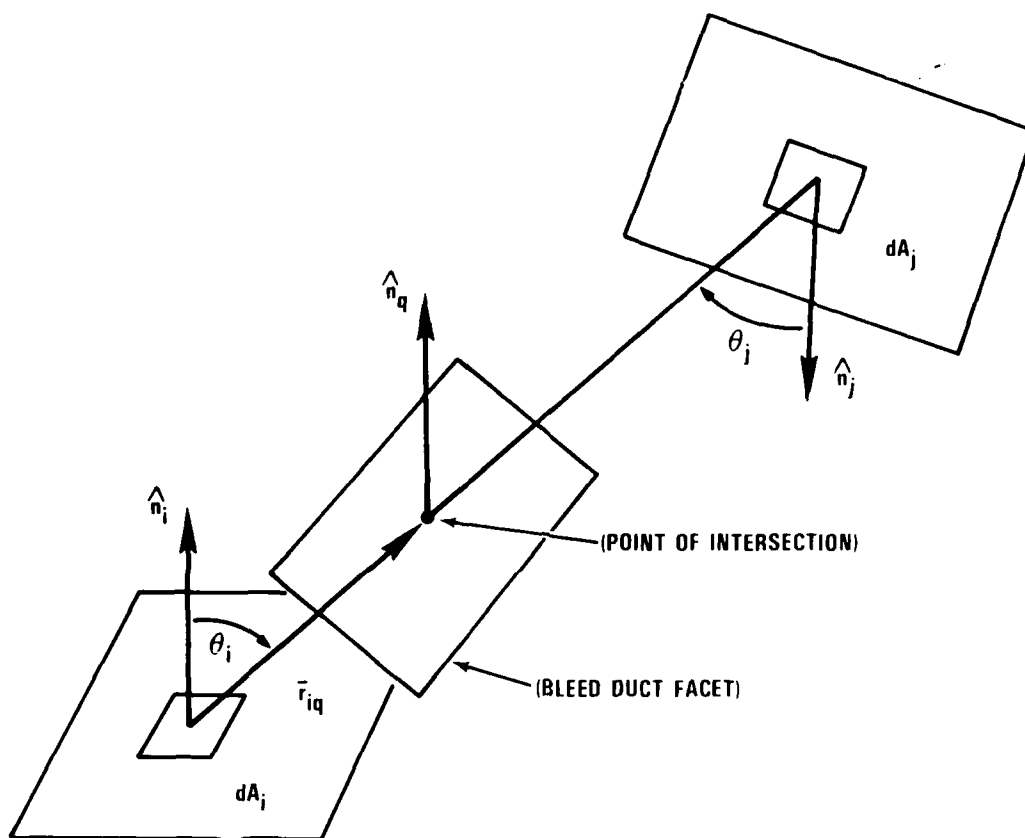
Figure 3. Surface Blocking by bleed duct.

section point is then checked for containment within the obstructing surface. After completing this test, the elemental surfaces on the two zones that are not obstructed is integrated to find the view factor F_{Ai-Aj}.

The fractional amount of radiative energy an IR sensor detects leaving a defined surface region of the nacelle/bleed duct enclosure depends on the IR sensor location and orientation, field-of-view, and spectral band region of detectability. With the radiosity $R_{j,k}$ of each zone surface (j) of the nacelle/bleed duct enclosure evaluated for the IR sensor's band region of detectability (k), the incident radiative energy detected from an IR sensor with an elemental area dA_{det} is defined as:

$$Q_{det.k} = \sum_{j=1}^{N} Aj \, R_{j.k} \, dF_{Aj-dA_{det}} \tag{10}$$

And by applying the reciprocity relation,

$$Aj \, F_{Aj-dA_{det}} = dA_{det} \, F_{dA_{det}-Aj} \tag{11}$$

to equation (3), the irradiance (incident radiative heat flux) $q_{det,k}$ detected from the IR sensor can be defined by:

$$q_{det.k} = \frac{Q_{det.k}}{dA_{det}} = \sum_{j=1}^{N} R_{j.k} \, dF_{dA_{det}-Aj} \tag{12}$$

where the view factor $dF_{dA_{det}-Aj}$ is determined by:

$$dF_{dA_{det}-Aj} = \int_{Aj} dF_{dA_{det}-dAj} \tag{13}$$

24

The 10-point Guassian Quadrature method is used in numerically integrating the configuration factor defined in equation (13).

To consider an IR sensor with a limited field-of-view as shown in Figure 4, the elemental view factor $dF_{dAdet-dAj}$ will either have a value:

$$
dF_{dA_{det}-dAj} = \begin{cases} 0 & \theta_{det} > \theta_{fov} \qquad (14) \\ \dfrac{\cos\theta_{det}\,\cos\theta j}{\pi\, r_{det}^{\,2}}\, dAj & \theta_{det} < \theta_{fov} \end{cases}
$$

If the elemental area on Zone (j) does not fall within the detector angular field-of-view θ_{det}, as shown in Figure 4, the elemental view factor $dF_{dAdet-dAj}$ is defined as zero and not integrated.

A radiation detection code was developed to incorporate the analysis presented in the preceeding paragraphs. The computer code implemented the theory for the "Zone Analysis Method" and defined the radiant energy exchange in the nacelle/bleed duct enclosure by calculating the view factors and the radiosities for each zone surface. The numerical code incorporated the capability to determine the irradiance detected by an IR sensor for arbitrary location and detector characteristics. The numerical program was written in Fortran 77 for the VAX 11-750 or the VAX 8600 computer system.

The code was used to predict irradiance trends for an IR sensor located in the nacelle/bleed duct enclosure during

25
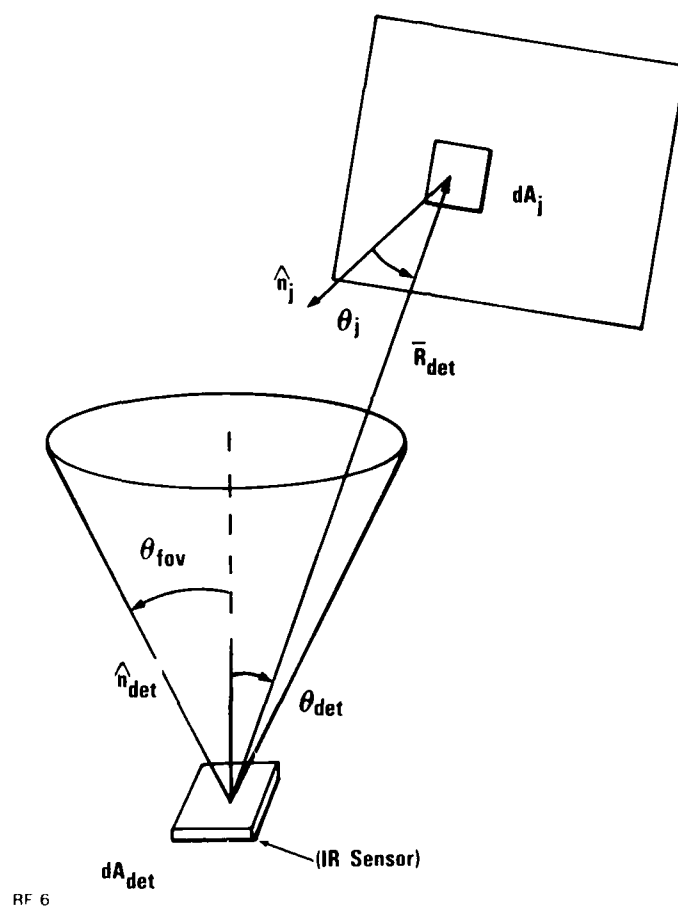
Figure 4. Detector field of view geometry.

simulated leak conditions in order to provide guidelines for sensor development and location of the sensors for the test program. The predictions were based on the M=0.0 (Idle Power) condition described in Section 3 (Table 3).

A hot air leak from the bleed duct is assumed to impinge on the top center region of the nacelle and heat only a small four-square-inch area to a steady-state temperature of 400 F. Before the leak occurs, the impingement region is assumed to be the same temperature of the nacelle airflow, or 100 F. The top surface of the nacelle, representing the inner surface of F-111 fuel tank, is made out of stainless steel and has a reflectivity of 0.8 for the IR sensors band range of detectability. The IR sensor range of detectability is assumed to be limited to a band of 2 to 4 microns. The bottom surface of the nacelle, representing the heated engine case, is assumed to have a temperature of 200 F and a surface reflectivity of 0.1.

The irradiance change detected with an IR sensor as a function of its distance from the leak region and its field-of-view was evaluated for this condition and the results are presented in Figure 5. The X and Y positions defining the IR sensor's location is illustrated on the plan view of the simulator facility in Figure 1. The IR sensor, for this evaluation, was defined three positions: X=2.0, 4.0, and 6.0 feet. At each of these positions, the detector is fixed at Y=0.5 feet from the right side wall of the nacelle and Z=0.25 feet from the bottom surface of the nacelle duct. At each position, the IR sensor is "looking" directly at the center leak region on the top surface of the nacelle section. The IR detector's field-of-view (FOV) was evaluated for the half-angle range from 5 to 30 degrees.

Figure 5 shows the irradiance change observed from the IR sensor when the surface temperature and radiosities of the nacelle/bleed duct environment change as a result of the simulated hot air bleed leak. The predicted results show, for any FOV,

27

BAND: 2–4 MICRONS
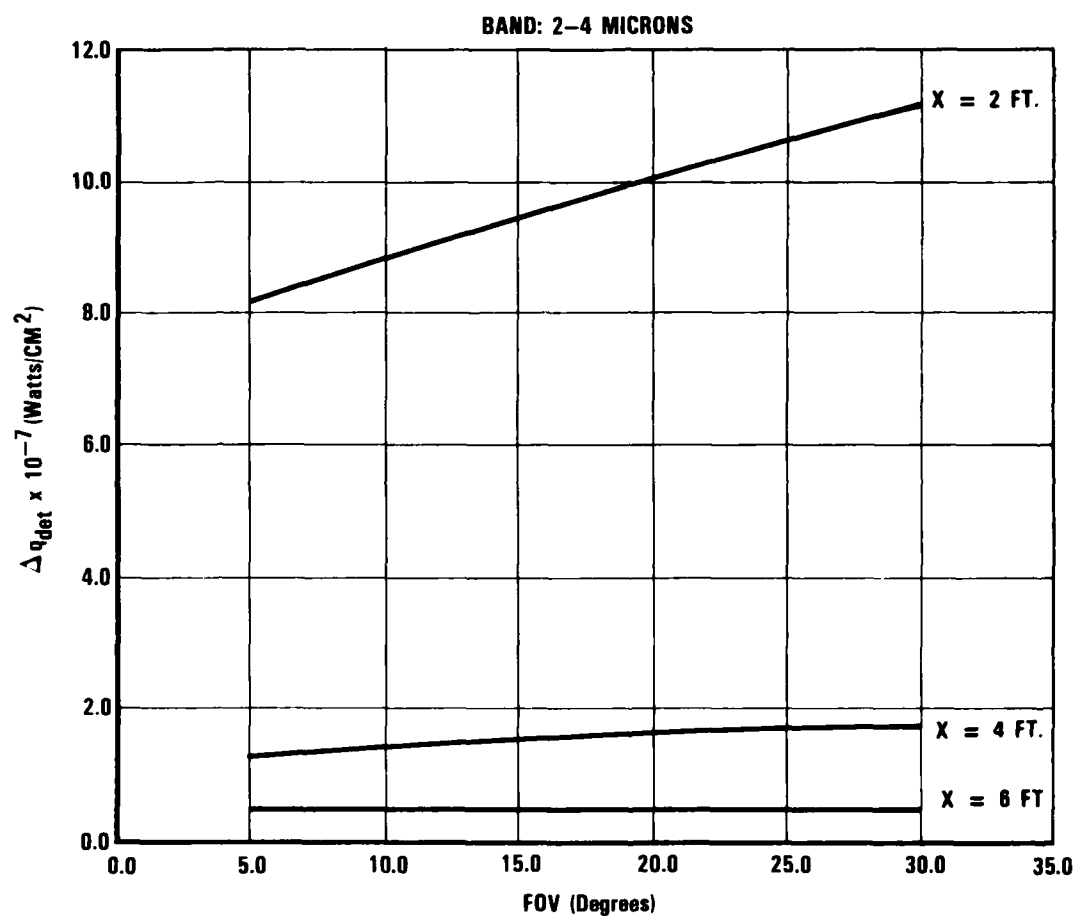
Figure 5.   Effect of position on detector irradiance.

RF 18

28

there is a considerable decrease in the irradiance change detectable from the IR sensor when placed at X=4 feet from the leak compared to X=2 feet from the leak. The magnitude of the difference in the detectable irradiance change from the two detector locations is approximately a factor of 10.

The numerical prediction of the view factors, which describe the fractional amount of the radiative energy leaving the surfaces of the leak region that arrives to the detector location, are observed to diminish considerably when moving the sensor from X=2 feet to X=4 feet from the leak. These results show that the sensors view of the radiosity change at the leak region diminishes rapidly as the detector is initially moved away from the hot air impingement region. As the detector is moved further back from X=4 feet to X=6 feet from the leak region, there is a similar trend in the drop of the irradiance change detected from the sensor, but the drop in the detector performance is not as significant.

In increasing the sensor's field-of-view at any of the three locations in the nacelle enclosure, Figure 5 shows, as expected, an increase in the detectable irradiance change. The slope of the irradiance change with respect to the field-of-view angle is noticeably large for the sensor nearest the leak region, at X=2 feet. The slope decreases to a small value as the sensor is moved back to a position X=6 feet from the leak region. For a fixed FOV angle (the sensor at X=2 feet does not observe as much of the surrounding surfaces affected by the hot air leak), as the sensor would if positioned at X=4 and X=6 feet. The sensor, positioned at X=2 feet as compared to the other two locations, detects a larger increase in surface area affected by the hot air leak impingement because the FOV increases from 5 to 30 degrees.

Figure 6 shows the irradiance detected by the IR sensor from only the nacelle leak region of 36 zones (1 in. by 1 in.) after the leak occurred. The detectable irradiance trend with respect

29
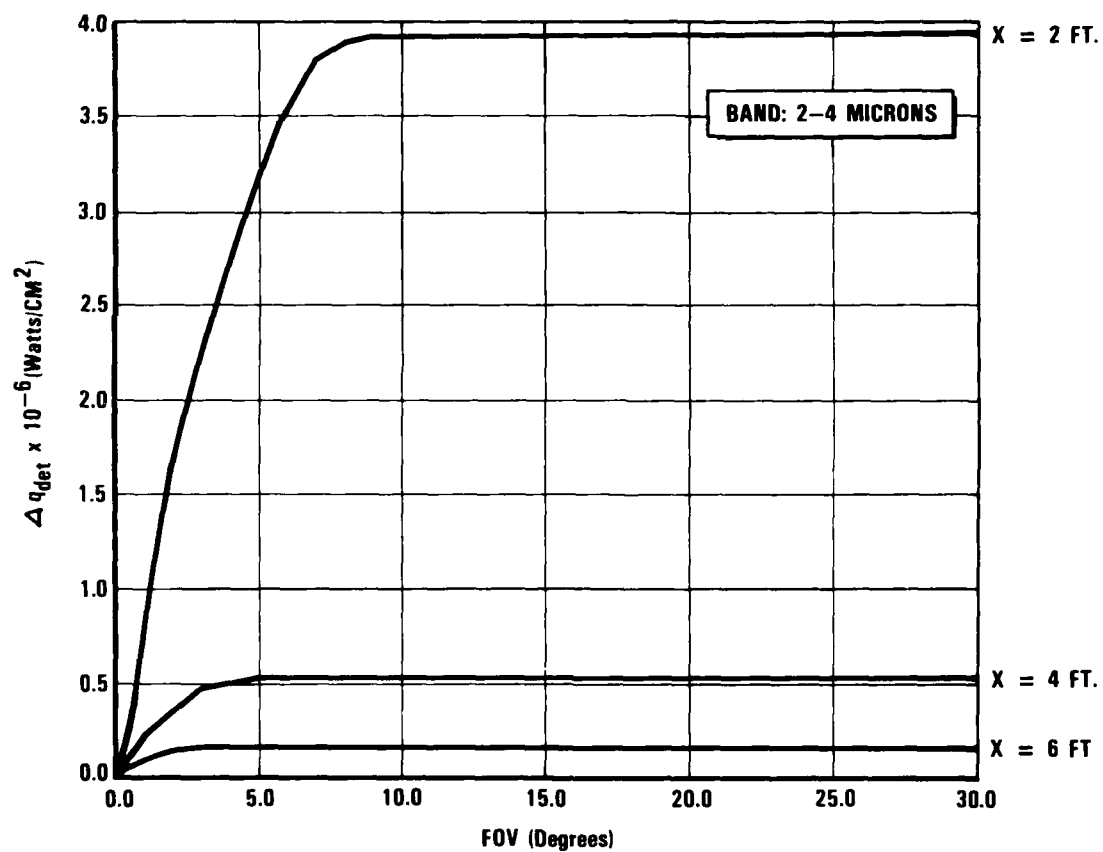
Figure 6. Effect of leak area on detector irradiance.

to the sensors distance from the leak are similar to the results in Figure 5. As expected from the graph, the detected irradiance is zero if the sensor's FOV is zero. For the sensor closest to the leak (at X=2 feet), there is a sharp increase in the irradiance detection when the FOV angle is initially increased from 0 degrees. Eventually the sensor will view the entire leak, and the irradiance detected from that region will not change with the increase in FOV. A sensor further away (at X=6 feet) will view the whole leak region with the smallest FOV angle. As illustrated from the Figure 5, the sensor views the entire leak at a FOV angle of 8 degrees for X=2 feet, at a FOV angle of 5 degrees for X=4 feet, and at a FOV angle of 3 degrees at X=6 feet.

The results of the analysis presented in Figures 5 and 6 were used to define the location of the IR instrumentation for the simulated bleed leak tests. We decided to locate the instrumentation at a distance of 2.0 feet from the leak, as will be discussed in Section 3, to maximize detection capability and extend the area coverage to as large an area as possible. We felt that this selection of location would represent a reasonable test of the IR detection concept. In addition, the results of the analysis were transmitted to HTL K West Systems to aid in the design of the radiation detection instrumentation. The numerical procedure was also used to conduct post-test analysis of the IR test results. The results of this analysis are presented in Section 5.3.2.

SECTION 3

DESIGN OF BLEED DUCT/NACELLE SIMULATOR

A bleed duct/nacelle simulator was designed based on consideration of the actual F-111 nacelle cavity in the vicinity of F.S. 650.

The F-111 engine, nacelle cavity, and surrounding structure is shown schematically in Figure 7. Engine bleed air required for various aircraft subsystems (ECS, ejectors, etc.) is supplied from the engine bleed port (located on the side of each engine near F.S. 650) and routed via a crossover duct on the top of each engine to a bleed duct distribution system which branches into forward and aft sections. The bleed ducts in this area are uninsulated and are constructed of stainless steel with diameters ranging from 2.5-in. to 1.0-in. Fuel tanks are located above each engine and in the center section of the fuselage in this area. The outer surface of the fuel tank consists of a thin sheet of stainless steel, backed with an insulation blanket. Bleed leaks in this area are especially critical since they have, based on past experience, penetrated the stainless steel/insulation structure and created hazardous fire conditions.

The distance between the outer surface of the engine and the upper fuel tank surface areas varies considerably in this area, but a distance of 6.0 in. was selected as a representative value for use in the design of the bleed duct/nacelle simulator.

The design objective was therefore to design a nacelle section which simulated the actual F-111 nacelle structure. The simulator was to incorporate the engine surface, nacelle flow area, fuel tank surface, and a representative bleed duct. In addition, only one quadrant (90 degrees) of the engine/nacelle cross section was incorporated to minimize size and nacelle flow

(a) LH SIDE VIEW OF F-111A

(b) VIEW LOOKING AFT F-111A
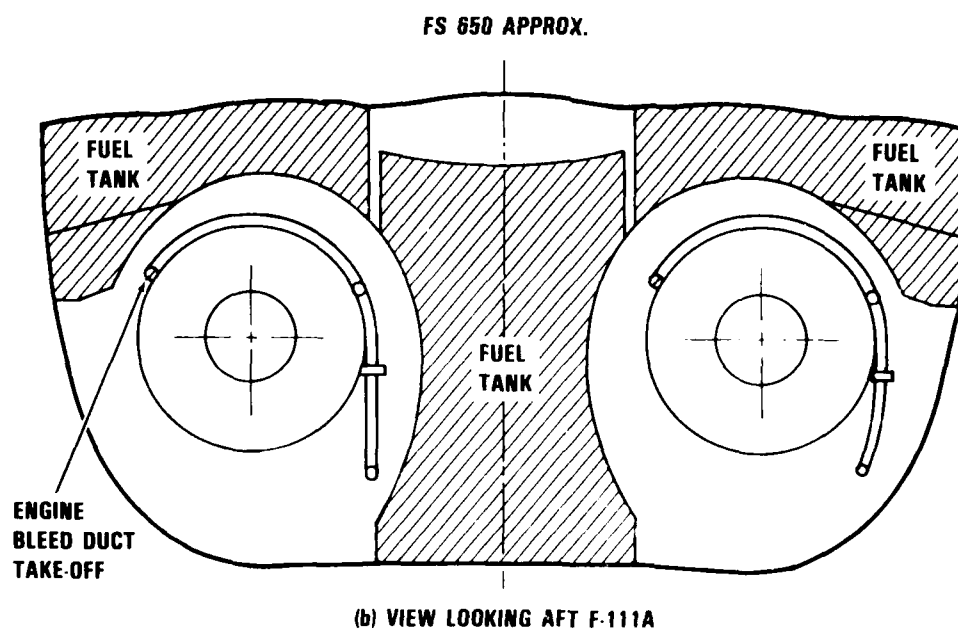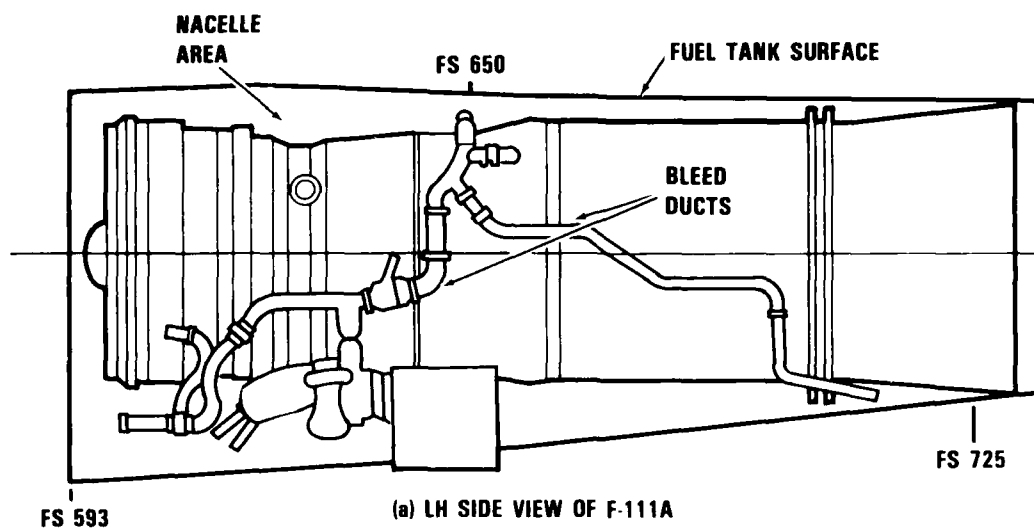
Figure 7. F-111 nacelle configuration.

requirements of the simulator. The engine case arc length, based on an engine diameter of 36.0 inches, is 28 inches. To minimize manufacturing costs, curved surfaces of the engine case and fuel tank surface were not incorporated in the simulator. The nacelle cross section was, therefore, rectangular in geometry with dimensions of 6.0 inches by 24.0 inches.

The configuration of the bleed duct/nacelle simulator is shown schematically in Figure 8. The nacelle section is 10.0 ft. in length and is constructed from 0.25 inch aluminum. A 2.0-inch-O.D. stainless steel duct is positioned in the center of the nacelle and runs the entire length of the nacelle. A hole is located in the 2.0-inch duct, 2.0-ft. from the nacelle air outlet, to simulate the bleed leak. Provisions are incorporated in the duct to allow simulation of bleed leaks at various angles (±) from the normal to the fuel tank surface. The fuel tank surface is constructed of 0.06-inch stainless steel separated from the basic aluminum structure by 0.25 inch of insulation.

A 1.0-ft. by 1.0-ft. cutout section in the stainless steel is provided directly above the leak to provide access to the leak. An array of 28 iron-constanton thermocouples are located on this cutout surface to measure the thermal response of the fuel tank surface to the leak. Heaters are installed on the simulated engine case surface to maintain the temperature of this surface 100 F above the nacelle air temperature. A detailed description of the simulator, including a discussion of bleed air supply for the 2.0-inch duct and simulated leak, is presented in Section 5.1.

Figure 8 shows the locations of the radiation detection instrumentation and Systron-Donner cable elements. The two radiation packages shown are located upstream (with respect to the nacelle flow) of the leak to minimize any possible convective heating from the leak on the radiation detection packages. The Systron-Donner element is included to provide a comparative evaluation of the current overheat element system utilized on the
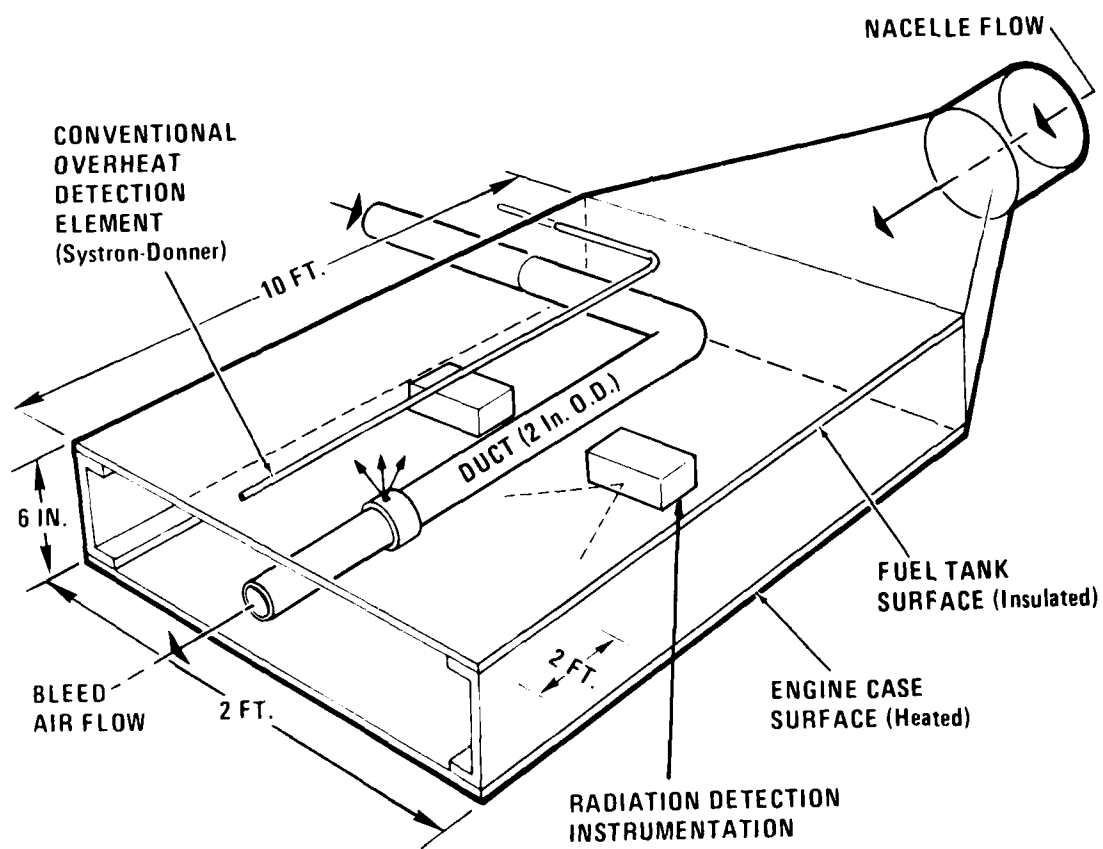
Figure 8.   Nacelle/bleed duct simulator.

F-111 to the IR concepts being evaluated. The detailed location of both the radiation detection instrumentation and cable-type element will be discussed in Section 5.1.

The flight conditions to be simulated in the tests were:

o   M=0.0, Sea Level
o   M=1.2, Sea Level
o   M=0.75, 40K Altitude

and provisions were therefore incorporated in the nacelle/bleed duct flow system to simulate nacelle flow characteristics, bleed flow characteristics, and leakage rates for these conditions.

The nacelle flow system was designed to simulate the airflow characteristics (temperature and air velocity) which would exist in the F-111 nacelle for the specified flight conditions to be evaluated in the tests. The static air temperature in the nacelle was assumed to be the total temperature of the external airflow for the specified flight condition where the total temperature is given by:

$$\frac{T_T}{T_\infty} = 1 + \frac{K-1}{2} M^2 \tag{15}$$

where,

T_T - Total Temperature - $^\circ$R
T_∞ - Ambient Temperature at Altitude - $^\circ$R
        (per MIL-STD-210A Hot-Day Conditions)
k -   1.4; Ratio of Specific Heat for Air
M -   Flight Mach No.

The nacelle air temperature, for example, for a M=1.2 (sea level) hot day condition (based on an ambient temperature of 103 F (563 R)) is obtained from equation (15) and has a value of 265 F. The nacelle airflow temperature for other flight conditions was evaluated in a similar manner. The nacelle airflow velocity

37

varies with flight condition and with location in terms of fuselage station in the nacelle for a particular flight condition (Reference 8). Values of nacelle airflow velocity were selected for the test, based on providing a realistic simulation of airflow effects within the limitations of the test lab airflow facility to provide the required air flowrates. The velocities selected for the M=0.0 (sea level), M=0.75 (40K ft.), and M=1.2 (sea level) conditions were 7, 50, and 80 ft/sec, respectively. The velocities were simulated in the test section by supplying nacelle airflow at the required flowrate for the particular flight condition. The flowrate was calculaced from:

$$\dot{m} = \rho V A \qquad (16)$$

where,

$\dot{m}$ – nacelle airflow rate – lb/min.

ρ – density of air based on nacelle air temperatures and pressure – lb/ft^3

A – cross-sectional area of nacelle – ft^2

$\quad = \dfrac{6 \text{ in. x } 24 \text{ in.}}{144}$

$\quad = 1.0 \text{ ft}^2$

The required flowrate, for example, to simulate an airflow velocity of 80 ft/sec. (M=1.2, sea level condition) was evaluated based on an air density evaluated at 265 F and 14.7 psia from equation (16) and found to be 263 lb/min. The required flowrates for the other flight conditions were determined in a similar manner.

Engine bleed conditions were based on the Pratt and Whitney TF30-P-9 engine data (Reference 9) and are listed below for the three flight conditions to be evaluated:

FLIGHT CONDITION	P (PSIA)	T ($^{\circ}$F)
o M=0.0, Sea Level (Idle Power)	44	400
o M=0.75, 40K ft.	40	600
o M=1.2, Sea Level	384	1080

Aircraft duct failure modes which induce bleed leaks include a wide range of possibilities. The size of the opening produced by the duct failure may range from small cracks on the order of 0.5 by 0.01 inch (as discussed previously in Section 2.0) to larger openings associated with failure of weld joints between branching ducts or duct couplings. Considerable uncertainty exists, therefore, with respect to size of the bleed duct leakage area to be simulated in the tests. We arbitrarily decided to simulate a bleed leak opening with a hole having a diameter of 0.25 inch in the 2.0-inch duct. The flow area of this hole, for reference purposes, would correspond to a rectangular opening having dimensions of 2.50 inches by 0.02 inch.

The leakage flow rates to be utilized in the testing were determined based on consideration of the size of the leak and the pressure and temperature corresponding to the individual flight condition. The leakage flow was calculated by assuming the flow to be choked, i.e. Mach No. equal to 1.0, in the 0.25-inch-diameter hole. The flow was then calculated from:

$$\frac{\dot{W}\sqrt{T}}{PA} = 0.532 \qquad (17)$$

where,

$\dot{W}$ - flow rate - lb/sec.

P - duct presure - lb/ft^2

T - duct air temperature - $^{\circ}$R

A - area of 0.25-in.-diameter hole - ft^2
  = 3.40 x 10^{-4} ft^2

The leakage flow for the M=1.2, Sea Level, condition based on a bleed temperature of 1082 F and a bleed pressure of 384 psia is found from equation (16) to be 15 lb/min. Leakage flow rates for the other flight conditions were calculated in a similar manner.

The nacelle flow characteristics (temperature and flow rate), bleed air temperature and pressure, and leakage flow rates utilized in the design of the simulator, are summarized for the flight conditions to be evaluated in Table 3.

TABLE 3. NACELLE/BLEED AIR CHARACTERISTICS.

FLIGHT CONDITION	BLEED AIR		NACELLE		LEAKAGE RATE LB/MIN
	P PSIA	T °F	FLOW LB/MIN	T °F	
M = 0.0, SL. (Idle Power)	44	395	30	100	2.4
M = 1.2 SL	384	1082*	263	265	15.0
M = 0.75 40K	40	600	248	75 (Room Temp.)	1.90

*Limitations of Laboratory System Will Limit Temperature to ~ 800 F

RF 11

SECTION 4

RADIATION DETECTION EQUIPMENT

Two types of optical detection instrumentation were developed for use during the test series. One type was used solely for spectral analysis purposes; the other type was intended to demonstrate the feasibility of operating infrared detectors and their associated electronics in a high-temperature ambient (i.e., an environment simulating an aircraft hot engine environment).

4.1 Spectral Analysis Instrumentation

The spectral analysis measurements were performed by two similar Radiometric Analysis Packages (RAPs). The two packages were dimensionally identical, (8.0 in. by 8.0 in. by 4.0 in.), each housing up to four infrared detectors and their associated amplification electronics. Each package was fabricated from aluminum with a stainless steel rear cover plate. High-temperature gasket material was used to seal the entire package, ensuring no leakage of water into the internal electronic circuits or out to the laboratory environment. Each package had two high-temperature electrical connectors, one carrying regulated electrical power and one carrying the (amplified) electrical analog signals from each of the infrared detectors. Regulated electrical power was supplied from a remote (outside the test fixture environment) power supply, providing positive and negative DC power (+24VDC, OV, -24VDC) via high-temperature cable harnesses and connectors. The amplified electrical analog detector signals were input into a junction box (which contained the regulated power supplies), also via high-temperature cable harnesses and connectors. At this location the analog signals were output on conventional BNC instrumentation connectors, suitable for inter-connection to the data capture instrumentation. Further details of the test instrumentation are displayed on Figure 9.

43
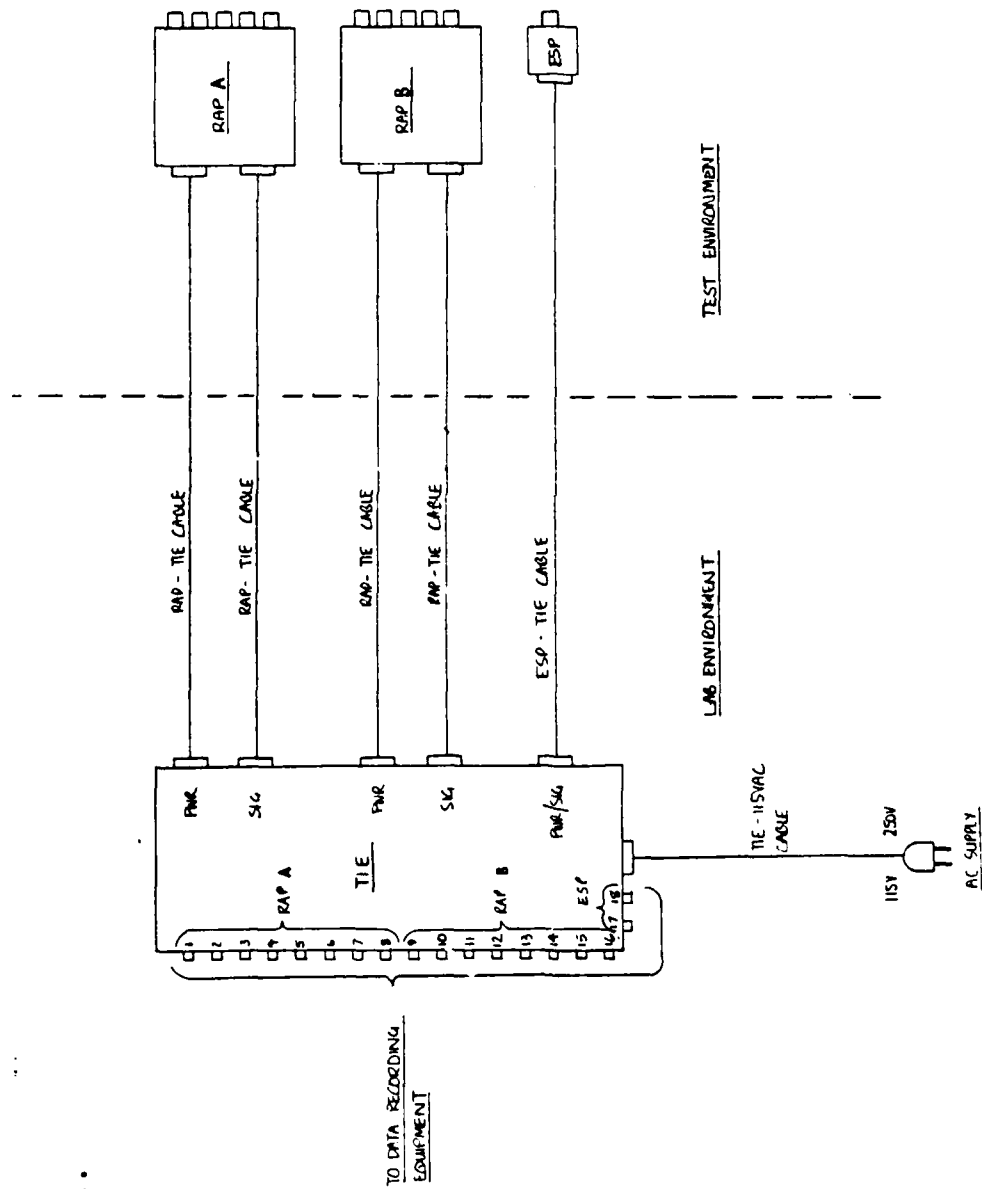
Figure 9. Optical test instrumentation interface.

Each RAP had two water-cooling connections, one input, and one output. Water was supplied on a continuous-flow basis and was drawn from a conventional tap supply via high-temperature hoses. The hoses were affixed to the RAPs with cramp-type fittings.

One RAP, RAP A, was designed to contain four thermopile detectors, each with an unfiltered sensitivity essentially flat from the ultra-violet to the far infrared (from 200 nanometers or less, to 15 microns or more). The other RAP, RAP B, contained two thermopiles (similar to RAP A device), a lead selenide (PbSe) detector, and a pyroelectric detector (lead zironate titanate). The lead selenide device had an unfiltered response which peaks at approximately 4 microns and is useful from approximately 1 to 5 microns (at 77 F). The pyroelectric device had an unfiltered response essentially flat from 1 to 15 microns or greater. The relative responsivities of the different optical detectors is approximately as follows: lead selenide 1500 volts per watt (V/W); pyroelectric 250 V/W; thermopile 50 V/W.

Lead selenide and pyroelectric detectors were employed (recognizing their inherent temperature and rate of change dependencies respectively), because of their higher responsivities compared to thermopiles. Both detectors' outputs were connected to AC-coupled amplifiers; thus, any long-term (with respect to the AC filter's time-constant) temperature-related drift mechanisms could be neglected.

The thermopile devices were employed because of their broad-band sensivity, relative insensitivity to ambient temperature, and ability to measure constant levels of irradiance (unlike the pyroelectric device). The thermopile devices were connected to both DC and AC coupled amplifiers; any long-term "background" irradiance (normal engine operating conditions such as high-temperature nacelle air, bleed duct temperature, etc) and temperature related drift mechanisms were effectively reduced to zero by the AC-coupled amplifiers. All constant levels of

radiation, incident on the thermopiles and converted into electrical signals, were amplified by the DC amplifiers. Their outputs represented the totality of the observed irradiance independent of time rate-of-change.

AC amplifiers were designed in case the introduction of the leak in addition to the background radiation caused rapidly changing (increasing) irradiance levels. Signal-to-noise ratio would be artificially enhanced therefore, as the preexisting background irradiance and its associated detector signal would be filtered out by the capacitor coupled components acting as a high pass filter. The supposedly rapidly changing (with respect to the capacitive filter's time constant) leak-induced signal would pass through the high pass filter to be identified as a notable event.

DC amplifiers were designed to measure the absolute (with respect to the thermopile cold junctions) irradiance caused by both the background ambient and the effects of the leak itself. Optical signal-to-noise ratios could be empirically determined from the resultant data.

The calibration curves for each type detector/amplifier combination are shown in Appendix A. In the case of the lead selenide and pyroelectric detector/amplifier combinations, the curves represent instantaneous response calibrations. Any long-term irradiance would be filtered by the high-pass AC-coupling filters in the amplifier sections. Only one curve is shown for the six thermopile detectors; the unit-to-unit thermopile sensitivity variance amounts to less than 10%.

The RAP detectors were calibrated, using a Heimann Blackbody Radiator and a Moletron PR200 Pyroelectric Radiometer. Calibrations were performed at various source/detector distances. In addition measurements were made at two blackbody temperatures and cross-referenced for increased accuracy. The irradiance levels

46

were established using the Moletron radiometer and were confirmed by theoretical calculation assuming a blackbody source. The calibration of the Moletron radiometer is traceable to the National Bureau of Standards.

A diverse selection of infrared filters was available, thus permitting a wide variety of individual wavelength bands to be analyzed during a test. Each detector location on the respective RAP was capable of accepting one filter. Filters, once installed, could be interchanged freely by the removal of a threaded location ring which locked the individual filters into place. The center wavelengths, half-power bandwidths, and transmissions of each filter were chosen in an attempt to discretely map a partial spectral signature (between 2 to 14 microns) for the nacelle/bleed leak environment. However, since limited detectors were available on the RAPs, not all the discrete wavebands could be investigated. The filters which were used and and their location on the respective RAPs is detailed in Figure 10. The transmission and bandwidth data for the filters are displayed in Appendix B. The channel number that the detector outputs were recorded on and the average transmission coefficient are also shown for each filter in Appendix B.

Two RAPs were used (as opposed to one) due to the internal size constraints of the test fixture. The RAPs were symmetrically placed about the 2.0-inch bleed air duct (see Figure 10), viewing the expected location of the bleed air leak from a distance of 24.0 inches (measured to the center of each RAP package). Each package was water cooled to maintain the infrared detectors and their associated electronics at temperatures considerably below the high nacelle temperatures. Cooling of the RAPs provided two major benefits. One benefit was the provision of a stable operating temperature for each infrared detector. Infrared detector sensitivity is affected by ambient temperature, and drastic changes in temperature can produce error signals. The other benefit was a reduction in the overall electronic circuit
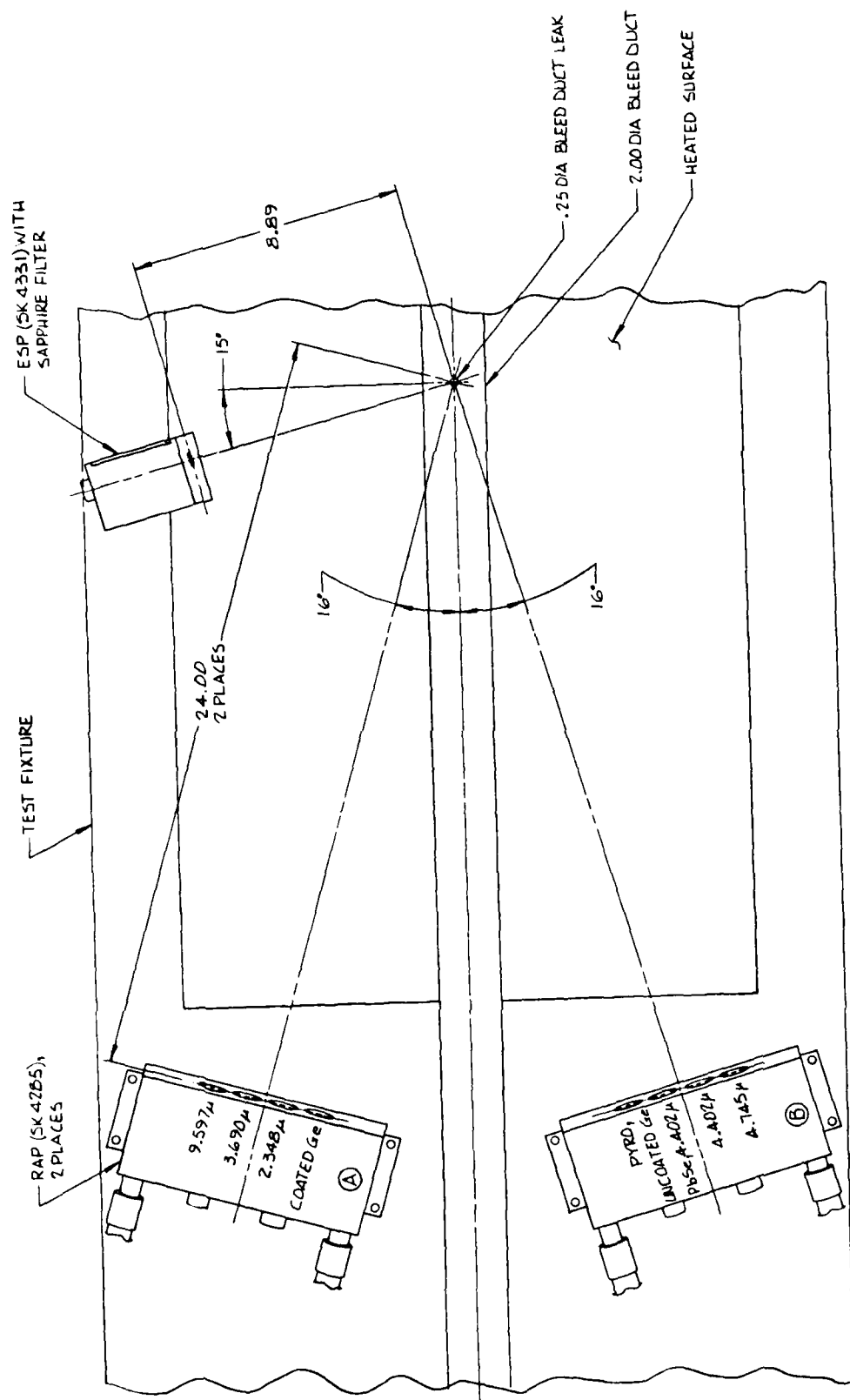
Figure 10. Filter location on RAPs as orientated in the test fixture.

48

noise and voltage offsets, also achieved by operation in a more benign temperature ambient. Although the water input to the RAPs had a temperature of approximately 50 to 60 F, measurements indicated that the exterior of the RAP packages was approximately 150 F during the tests when nacelle air temperature was approximately 265 F. This measurement is indicative of the cold junction temperature of the thermopile devices. Because thermopile devices measure the difference in temperature between their hot junctions (where the incoming infrared radiation is absorbed) and their cold junctions (generally the chasssis or case), the irradiance measurement is dependent on the cold junction being maintained at a constant and known temperature. A corrected irradiance measurement is therefore based on the recorded value plus a correction factor dependent on cold junction temperature.

Each detector had an intrinsic field-of-view (FOV). All of the RAP detectors had FOVs between 95 degrees and 110 degrees. FOV limitation was considered as one means whereby signal-to-noise ratio might be artifically enhanced in an actual production overheat sensor. In the case of the RAPs, FOV limiting was used during this testing for a number of reasons. Detector configuration can determine the extent of the FOV, as well as its adherence to the maximum theoretical (cosine) response. For example, the location of the sensing area, the size of the sensing area, the thickness of the window material, the refractive index of the window material, and the size of the detector aperture all jointly determine the overall detector FOV. Due to their construction, it is a characteristic of many infrared filters to change their absorbtion parameters as a function of angle of incidence for the incoming radiation. The filters which were used follow a theoretical cosine response out to an approximately 60-degree solid angle ($\pm$ 30 degrees). We therefore decided to limit the FOV to an approximately 40-degree solid angle ($\pm$ 20 degrees). FOV limiters would also act as re-emitters of infrared radiation, once heated; each detector output would therefore have a component

49

due solely to the FOV limiter. The two major emission sources in the RAPs' FOV were the 2.0-inch bleed air duct (not the leak) and the air-heated nacelle test fixture. The leak, once introduced, would be observed from an oblique angle around five degrees.

4.2 High-Temperature-Operating Sensor

An Environmentally Suitable Package (ESP), capable of operating at sustained high ambient temperatures, was also designed and used during the test series. This package (3.0 in. by 3.0 in. by 2.0 in.) contained a high temperature thermopile and associated amplifier electronics, similar to the RAPs. The package was an environmentally sealed aluminum casting. A single electrical connector carried both electrical power and amplified analog electrical signals from the single infrared detector. As with the RAPs, electrical power was supplied from the same remote power supply, and the detector analog signal was inputted to the junction box, via a combined power/signal high-temperature cable harness and connectors. The analog signal was also output on a BNC instrumentation connector.

The ESP had no water-cooling connectors; ESP temperature reached the ambient extremes rapidly due to its low mass and lack of cooling.

The ESP contained a high-temperature thermopile with a sapphire window; the sapphire window was essentially flat from ultra-violet to middle infrared (about 200 nanometers to 6 microns however, there is no particular significance for choosing this window's bandwidth). The sapphire window was selected for its durability over the temperature extremes, its resistance to contaminants, and as a sealing membrane for the thermopile detector. In an actual production overheat sensor, sapphire would probably not be used as the window (or "filter"). The shorter wavelength response would probably be undesirable, as sunlight, arc welding and visible light could cause large detection signals.

50

However, for the purposes of the controlled test environment, we felt it to be adequate. Also, being of a wideband nature, we presupposed that if a particularly interesting waveband (within the pass band of sapphire) was observed during the actual test, that an additional suitable external filter might be added to improve signal-to-noise ratio to investigate that particular waveband (much as was done with the RAPs). No opportunity presented itself to add an extra filter to the ESP detector during the test, so the above stated passband was monitored by the ESP throughout the tests. The thermopile detector was similar to the type used in the RAPs. The approximate responsivity of the detector was 50 V/W as with the RAP thermopiles. No calibration curve is provided, but the ESP response to the irradiance stated in the RAP thermopile curve would be approximately 5.7 times less electrical output for the same irradiance (this is purely a function of the reduced gain DC amplifier used in the ESP). This statement is only true at temperatures close to room temperature (70 F). We must be restate that the thermopile device generates a voltage which is proportional to the difference in temperature between its hot junction and its cold junction. Its hot junction is heated by the radiation received from an emission source (such as the 2.0-inch bleed air duct at 500 F). Its cold junction temperature is dependent on the case temperature of the detector case and ultimately on the temperature of the sensor housing. The sensor housing is maintained at a relatively constant temperature by the nacelle air flow. If the nacelle air flow temperature is raised (from room temperature to 265 F), the sensor case (and detector cold junction) temperature will be raised. Provided the detector hot junction temperature remains constant (the emission source remains constant), if the cold junction temperature is raised, then the temperature difference between hot and cold junctions will be less. If the difference in temperature is reduced, the detector output will be similarly reduced. The overall effect of this is to reduce the detector's electrical output response to the background (without the leak) irradiance. For example, suppose the ESP cold junction was maintained at 100 F

while exposed to the 265 F ambient caused by the nacelle air flow (like the RAPs). Suppose also that the observed irradiance from the emission sources within the ESP's FOV appeared to represent a composite blackbody temperature source of 400 F. The difference in temperature between the cold junction (at 100 F) and the hot junction (viewing 400 F) would be some delta temperature, Dt1. Now suppose that the ESP cold junction was allowed to rise to the 265 F ambient (caused by the nacelle air flow). The difference in temperature between the cold junction (at 265 F) and the hot junction (viewing 400 F would now be some lower delta temperature, Dt2. As the detector electrical output is proportional to its hot and cold junction temperature difference, DT2 would cause a lower electrical output than Dt1. Therefore, when operating the ESP at higher (than room) ambient temperatures, its electrical output will be less to the observed (constant) background radiation.

The ESP was located away from the RAPs so as not to become a dominant source or obstruction within the FOVs of the RAPs. To achieve this, the ESP was located off to the side of the intended leak location and slightly upstream of the leak (to minimize convective heating of the detector by leaking hot air). The net distance between the ESP and the expected leak location was approximately nine inches (see Figure 10).

No FOV limiters were used with the ESP; the FOV was therefore approximately 95 degrees solid angle (± 47.5 degrees). The two major emission sources in the FOV of the ESP were almost certainly the 2.0-inch bleed air duct itself (not the leak) and the air-heated nacelle test fixture. The leak, once introduced, would certainly be more visible to the ESP than either RAP package, but would still be observed from an ablique angle (10 degrees).

4.3 Data-Capture Instrumentation

Electrical signals output by the RAPs and the ESP were input to a junction box or Test Interface Equipment (TIE). This TIE

52

also housed the regulated power supplies for the optical measure-
ment devices. The TIE passed each electrical analog signal to a
BNC connector. Of the total available signals, only the RAPs'
thermopile DC-coupled and the ESP signal were connected via BNC
shielded cables to a RACAL Store 14 DS magnetic tape recorder.
The RAPs' thermopile AC-coupled signals, together with the RAP B
lead selenide and pyroelectric signals, were not recorded because
the rise time of the leak event was long and of similar duration
to any other temperature change effect (as will be discussed in
Section 5.3.2.1).

The RACAL tape recorder was capable of recording DC
electrical signals (by EM encodement) for a wide range of
frequency bandwidths and test durations. Tape speed was adjusted
to provide suitable bandwidth while not using many feet of tape
during each test. Tape speed was set for the most part to 15/16
inch per second. The tape recorder had signal input gain
adjustments, so that signal-to-noise could be maximized for any
given signal into the tape recorder. Recording of captured data
on this medium renders subsequent analysis significantly more
facile. Time histories may be condensed or expanded, as may
amplitude. "Hidden" data can be extracted without the necessity
to rerun a particular test.

Data, once recorded on the tape recorder, were replayed onto
a conventional chart recorder at the desired speed and with the
desired amplification. Calibration voltages measured by a
National Bureau of Standards(NBS) traceable digital voltmeter were
injected into the tape recorder in place of the optical analog
signals so that subsequent analysis of output voltages could be
scaled.

SECTION 5

SIMULATED BLEED LEAK TESTS

Simulated bleed leak detection tests were conducted utilizing both IR instrumentation and a conventional Systron-Donner cable element. This section covers the test setup, test procedure, and test results.

5.1 Test Setup and Instrumentation

The tests were conducted in a nacelle/bleed duct simulator section (see Figure 11) which was fabricated based on the design requirements formulated in Section 3. The nacelle section was rectangular (6.0 in. by 24.0 in.) in cross section and 10.0 feet in length and was constructed of 0.25-inch aluminum. The interior surface of the nacelle (simulated fuel tank surface) consisted of a sheet of stainless steel having a thickness of 0.06 inch and backed with 0.25 inch of insulation. A cutout section (1.0 ft. by 1.0 ft.) was located directly above the leak to provide for temperature measurement of the stainless steel surface directly above the leak. The exterior surface of the cutout section was instrumented with an array of 28 iron-constantan thermocouples (20 gage) attached by welding the junctions to the surface of the stainless steel. The locations of the individual thermocouples are shown in Figure 12. The output of the thermcouples was monitored by two Honeywell- Brown Electronik recorders.

The lower surface of the nacelle was heated over an area of 2.0 ft. by 4.0 ft. (see Figure 11) to simulate the engine case surface temperature (nominally 100 F above the nacelle air temperature). The heating was accomplished by attaching three 500-watt Chromalox strip-type electrical resistance heaters to the bottom surface of the aluminum nacelle structure which had a
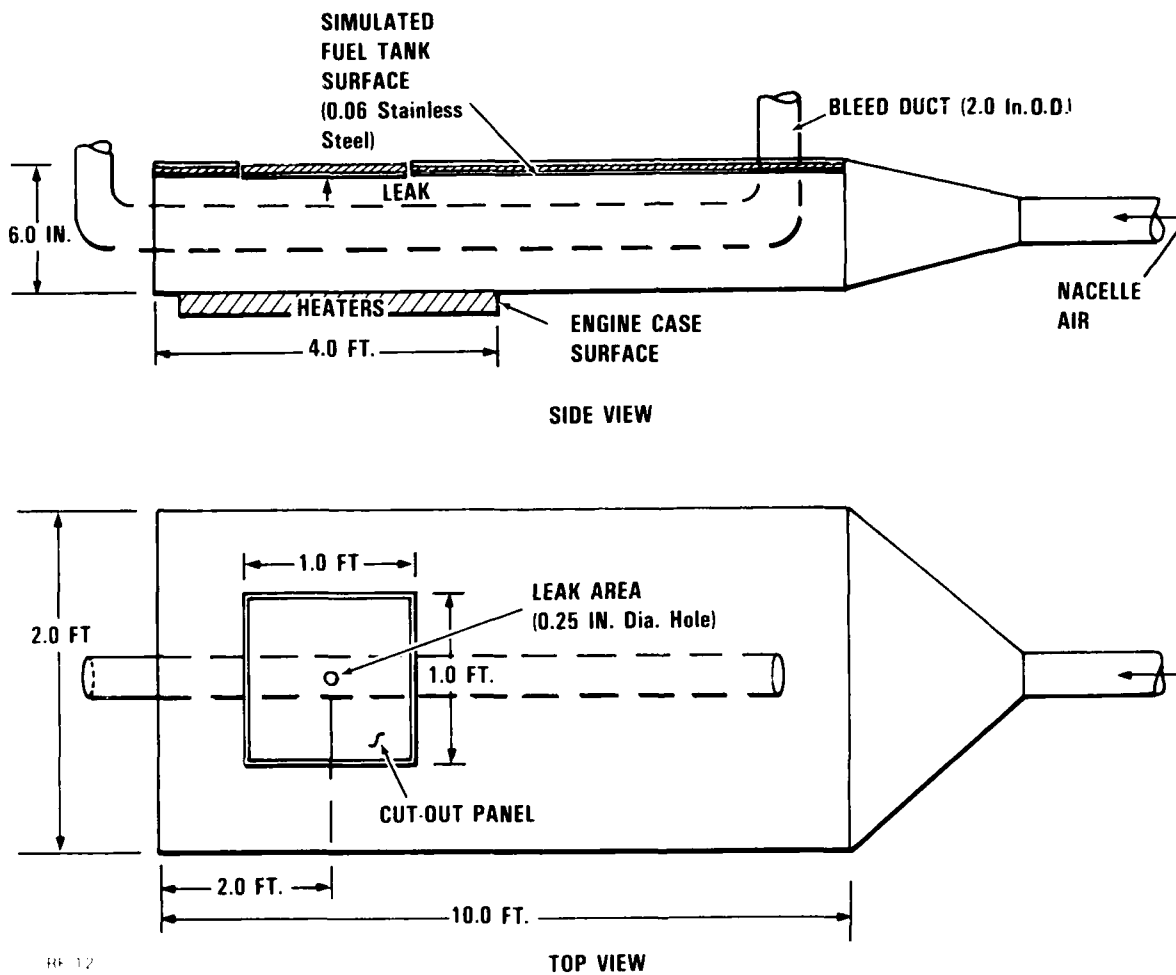
55

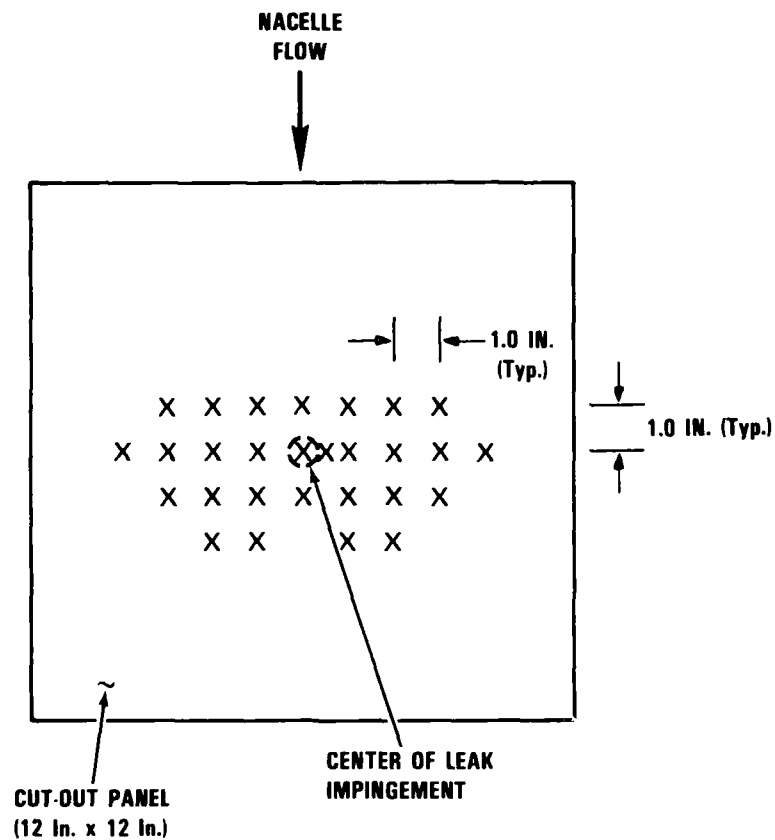Figure 11. Bleed duct/nacelle test configuration.

Figure 12.   Thermocouple locations on stainless steel plate.

maximum capacity of 1500 watts. The surface temperature of this section was monitored by five copper-constantan thermocouples (20 gage) spaced uniformily over the 2.0 ft. by 4.0 ft. surface area. The output of these thermocouples was monitored by a Honeywell-Brown Electronik recorder.

The supply air system for the rectangular nacelle section consisted of a 3.0-in.-O.D. supply line (23 feet in length) and a diffuser section having a length of 8.0 feet. The supply line provided the interface between the laboratory air distribution system and the nacelle section. Heating of the nacelle air was accomplished by mixing hot air from the laboratory heater system with ambient air to provide the required temperature of the nacelle flow.

The flowrate of the nacelle air was measured with a calibrated venturi (throat diameter of 2.3 in.) which was located in the supply line upstream (13.0 ft) of the nacelle section. The flowrate was determined by measuring the inlet pressure and temperature to the venturi for the high flowrates in which the venturi was operated in a choked condition and the pressure difference between inlet and throat conditions when the venturi was not choked. The measured pressures were then used to determine the flowrate from calibration curves developed for the venturi. The upstream pressure was measured with an Acco Helicoid (100 psia, full scale) gage for the choked conditions and the pressure difference was measured with a Trimount mercury manometer (80.0 in.) for the unchoked conditions.

The temperature of the supply air was monitored by an Omega copper-constantan temperature probe and a digital display unit which was located 6.0 inches upstream of the flow measurement venturi.

The IR instrumentation described in Section 4.0 utilized in the tests consisted of three separate packages installed in the

58

nacelle section as shown in Figure 13. The two larger radiometric analysis packages (RAP), each having dimensions of 4.0 in. by 8.0 in. by 3.0 in., were attached to the lower surface of the nacelle section and located 2.0 feet upstream of the simulated leak. The packages were orientated as shown in Figure 11. Cooling water was supplied to each of these packages from the laboratory water supply system. The smaller environmentally suitable package (ESP) which had dimensions of 3.0 in. by 3.0 in. by 2.0 in. was mounted on the sidewall of the nacelle section and positioned 9.0 inches from the leak location. The voltage output of the three instrumentation packages was monitored by a Racal Store 14DS magnetic tape recorder system. A Gould 2400 strip-chart recorder (Model No. 11-6402-11) was also incorporated into the data collection system such that outputs from the magnetic tape system, in terms of sensor output voltage versus time, could be displayed in graphic form for evaluation of the radiometric data.

A photograph of the test setup is presented in Figure 14.

The bleed duct and simulated leak system is shown schematically in Figure 15. A 2.00-in.-O.D. stainless steel duct is located in the center of the interior of the nacelle section and spans the entire length (10 feet) of the simulator. The simulated leak opening consists of an 0.25-in.-diameter hole in the 2.0-inch duct which is located 2.0 ft. from the nacelle air exhaust. The orientation of the hole is such that leaks introduced through the hole will impinge on the center of the cutout section (1.0 ft. by 1.0 ft.) shown in Figure 12 which is the simulated fuel tank surface. Leakage flow is supplied to the 0.25-in.-diameter hole via a 0.5-inch, stainless steel tube which was located inside the 2.00-inch duct and which spanned the entire length of the 2.0-inch duct. The 0.5-inch, stainless steel tube was welded to a stainless steel coupling which, in turn, was welded to the interior of the 2.00-inch duct in the line with the 0.25-inch-diameter hole. This configuration was selected to provide for simultaneous bleed flow through the 2.0-inch duct (to
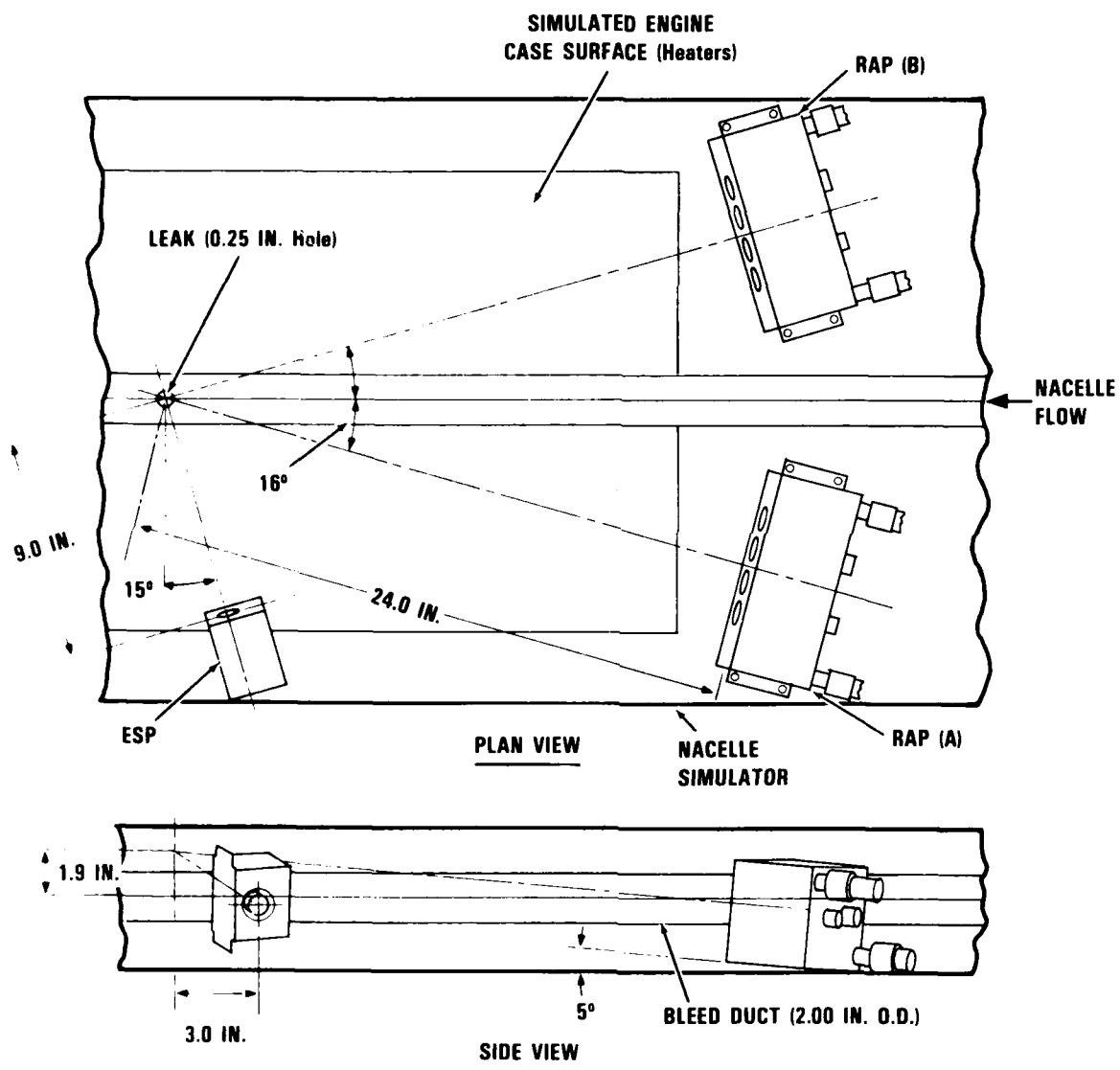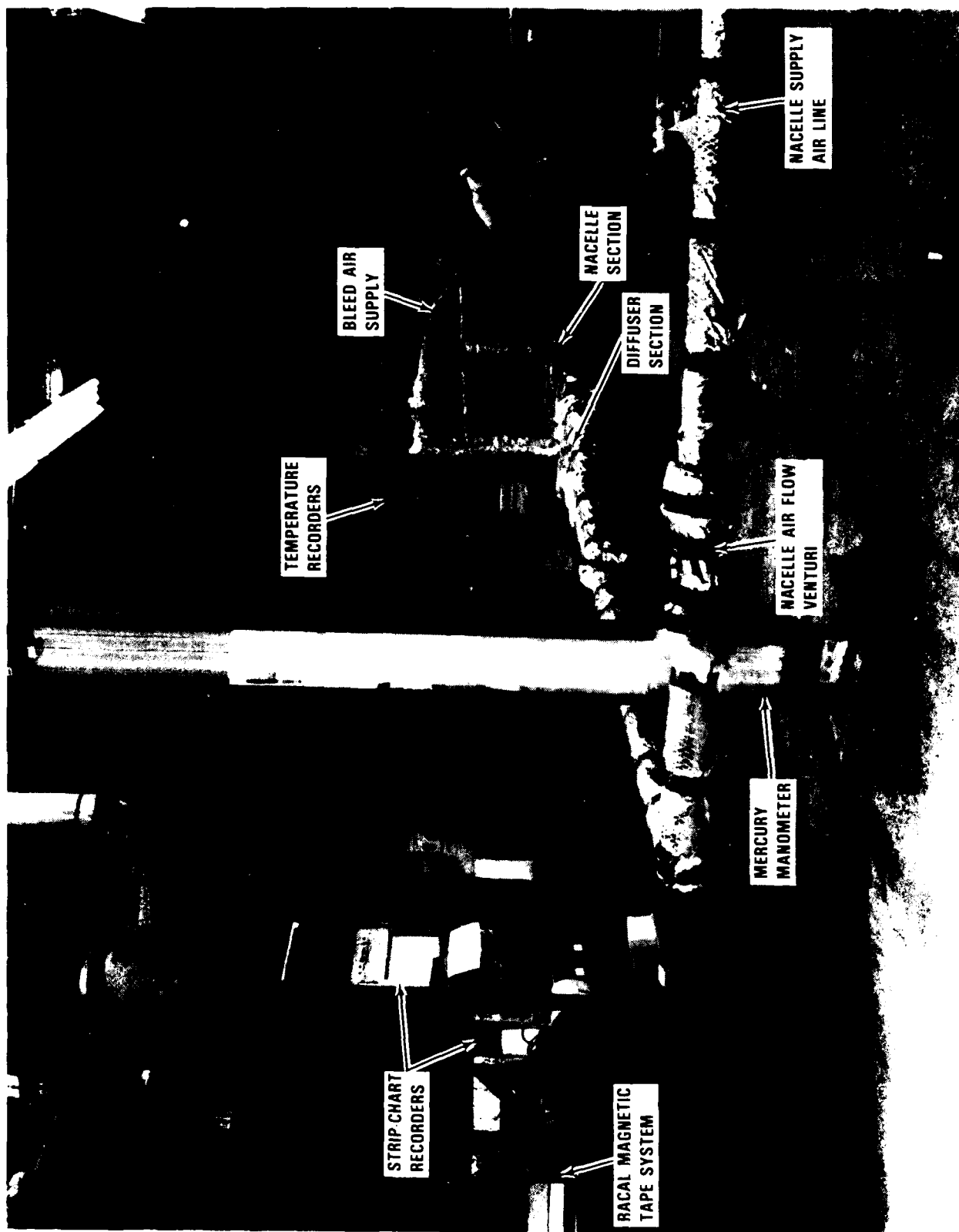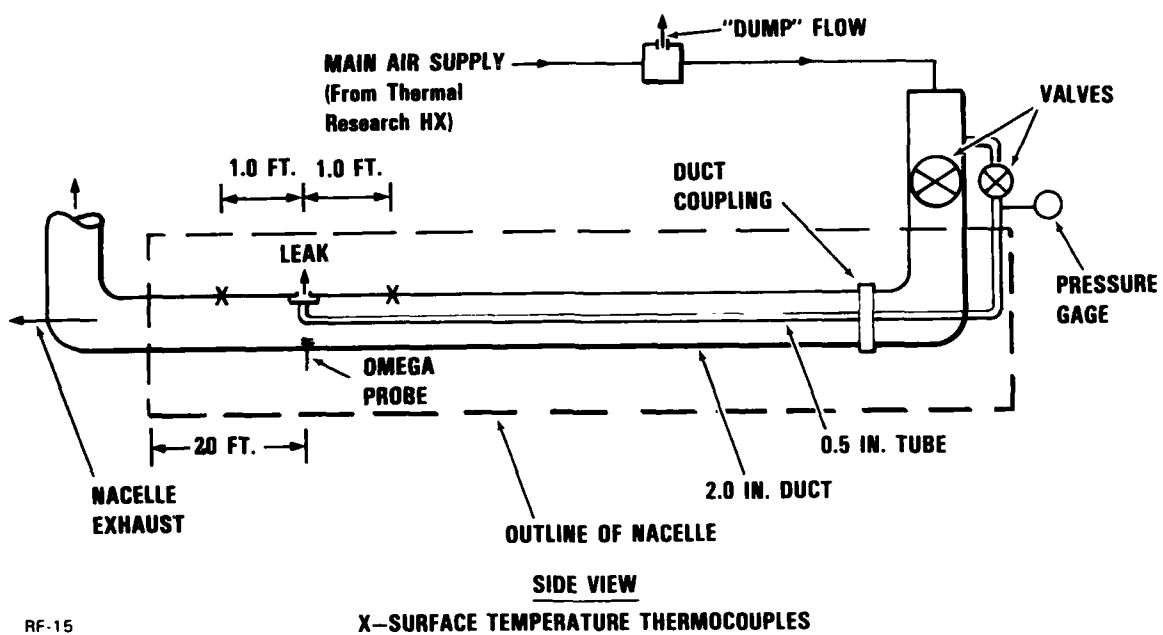
Figure 13. Radiation detection instrumentation locations.

Figure 14. Test setup.

Figure 15.   Bleed/leakage air system.

62

simulate the realistic duct surface temperatures) and independent introduction of leakage flow at specified flowrates. The flow through the 2.0-inch duct and leakage flow were controlled by valves which were located in each line upstream of the line inlet locations to the simulator. The high-temperature/high-pressure simulated bleed air is supplied from the laboratory system which incorporates a Joy compressor (500-psia maximum capability) and a Thermal Research (model 1010) heat exchanger. Bleed air at pressures of 400 psia and 800 F can be obtained from this system. Bleed air was supplied for the 2.0-inch duct and simulated leakage flow by this system via a line which incorporated a "dump" orifice. The orifice was provided to allow a fraction of the total flow (equal to the required leakage flow) to be discharged or "dumped" when flow was supplied to the 2.00-inch duct. When leakage flow was required, a valve at the "dump" orifice was closed such that the flow could be maintained at a reasonably uniform value in the 2.0-inch duct when the leakage flow was introduced. This minimized, therefore, the variation in surface temperature of the 2.00-inch duct.

The leakage flowrate was determined by calibrating (utilizing standard flow nozzle techniques) the 0.5 inch line with the 0.25-inch outlet installed in the end of the line such that the flowrate through the line could be determined from measurement of the inlet pressure (from pressure gage in Figure 15) and temperature.

The surface temperature of the 2.0-inch duct was monitored by two iron-constantan thermocouples welded to the outer surface of the 2.0-inch duct. These thermocouples were located along the centerline of the 0.25-inch leak opening and spaced 1.0 ft. upstream and downstream of the leak location. The temperature of the bleed air (2.0-inch duct and leakage air) was monitored by an Omega iron-constantan temperature probe positioned in the 2.00-inch duct near the leakage outlet. The positions of these temperature locations are shown in Figure 15.

Leaks could be simulated at various orientations by loosening the duct coupling on the 2.00-inch duct (see Figure 15) and rotating the forward portion of the 2.0-inch duct to the desired position.

5.2 TEST PROCEDURE

The test procedure utilized for both the IR and Systron-Donner tests will be discussed in the following sections.

5.2.1 IR Tests

The test procedure for these tests was initiated by completing basic pretest procedures. The temperature recorders were turned on and the run number and chart speed were recorded on the chart paper for the individual test run. The Racal magnetic tape recording system was activated and cooling water was supplied to the IR instrumentation (RAP) packages. Power was supplied to the heaters attached to the bottom section of the nacelle assembly (simulated engine case surface) and the Thermal Research heat exchanger system was activated. The high pressure and temperature air from this system was allowed to discharge to the laboratory ambient through the "dump" orifice.

The required nacelle flowrate and temperature were then established. The bleed valve in the 2.00-inch duct was then opened and bleed flow at the required temperature was introduced through the 2.00-inch duct. The nacelle surface temperatures, bleed duct surface temperatures, and heater surface temperatures were then allowed to reach equilibrium. The background radiation level, as measured with the IR instrumentation, was recorded at this stabilized condition. The required leakage flowrate was then introduced through the 0.5-inch-diameter line. The "dump" valve was closed as the leakage flow was introduced in order to maintain essentially constant flow through the 2.00-inch duct and minimize changes in surface temperature of the 2.00-inch duct. This provision is not incorporated in the original test runs (Runs 1-(1-C) of Table 4) and the flow changed drastically in the 2.00-inch duct when the leak was introduced. This condition resulted in a significant drop in duct surface temperature, and the "dump" valve provision was incorporated beginning with Run 1-D. This

65

procedure was not totally effective but did significantly reduce the variation in duct surface temperature when the leak was introduced. The leakage flow as allowed to impinge on the upper nacelle surface (simulated fuel tank surface) until equilibrium, was established as indicated by the output from the 28 thermocouples attached to this surface. The leakage flow was then "turned-off," and the heated surface was allowed to cool and return to its initial value. The output of the radiation detection instrumentation was recorded continuously from the time of the initial background reading until the system temperatures again stabilized after the leak was removed.

Tests were conducted utilizing this procedure, and the test conditions are summarized in Table 4. Three flight conditions were evaluated; M=1.2 (sea level), M=0.75 (40K ft.), and M=0.0 (idle power). The M=1.2 condition was evaluated at three different leak orientations: normal, +45 degrees, and -45 degrees with respect to the simulated fuel tank surface. The other two conditions were evaluated only for the normal orientation. Runs (5, 6, 8, 9) were originally included in the test plan to evaluate the M=0.0 (idle power) and M=0.75 (40K feet) conditions at angular leak orientations of ±45 degrees. These runs were not conducted since the normal leak orientations at these conditions did not appear to yield significant results.

Certain modifications to the basic test procedure were implemented for selected test runs. These modifications will be discussed in the following paragraphs.

After completion of Run 1 (Table 4) we verified that the effects of the high temperature (267 F) ambient environment were influencing the output of the IR instrumentation as expected. The IR detectors in the RAP packages were therefore fitted with protective blanking covers (Runs 1-A and 1-B) to prevent exposure of the sensors to incident radiation in order to evaluate effects of ambient temperature on sensor output.

66

TABLE 4. IR TEST CONDITIONS.

FLIGHT CONDITION	RUN NO.	BLEED TEMP. °F	LEAKAGE FLOW RATE LB/MIN.	NACELLE		HEATER SURFACE °F	LEAK ORIENT.	COMMENTS
				FLOW RATE LB/MIN.	T °F			
M = 1.2, S.L.	1	810	12.3	263	267	307	NORMAL	TEMP. OF 2.00 IN DUCT CHANGED
	1-A	825	12.2	263	267	340		IR DETECTORS "BLOCKED" OFF
	1-B	800	12.0	260	266	?40		IR DETECTORS "BLOCKED" OFF
	1-C	825	11.8	263	263	338		TEMP. OF 2.00 IN DUCT CHANGED
	1-D	825	11.7	266	266	339		TEMP. OF 2.00 IN DUCT STABLE
	1-E	−	−	−	−	−		•
	1-F	840	11.3	263	267	357		REPEAT OF RUN 1-D
	1-G	875	10.4	134	265	346		NACELLE FLOW REDUCED
M = 0.75, 40K	2	595	1.9	248	75	167		−
M = 0.0, S.L.	3	435	2.4	34	90	218		TEMP. OF 2.0 IN DUCT CHANGED
	3-A	400	2.4	58	120	192		NACELLE FLOW INCREASED
M = 1.2, S.L.	4	790	11.5	264	265	345	+ 45°	TOWARD ESP PKG.
	4-A	765	11.4	266	263	345	+ 45°	REPEAT OF RUN 4
	7	790	11.5	263	267	355	−45°	AWAY FROM ESP PKG.

*Series of Tests to Isolate Magnitude of Individual Radiation Sources, i.e., Leak, 2.0 In. Duct, Nacelle Background, Heater Surface

RF 20

67

After completion of Run 1-D, we decided to isolate and quantify the magnitude of the individual radiation sources, i.e. surface heated by the leak, 2.00-inch duct, nacelle background, and heater surface (simulated engine case surface). Run 1-E was conducted to evaluate these individual effects. This test (Run 1-E) was conducted immediately after the leak was introduced in Run 1-D and resulting surface temperatures were allowed to stabilize. The test incorporated the following sequence of events: (1) leakage flow was turned off and heated surface above leak was allowed to stabilize, (2) 2.00-inch duct flow was turned off, (3) heaters (simulated engine case surface) were turned off, (4) nacelle flow was reduced to 50 lb/min and temperature of nacelle flow was reduced to room temperature, (5) the leakage flow was reintroduced and then turned off, (6) flow was introduced in the 2.00 inch duct and then turned off, and (7) heaters (engine case surface) were turned on and surface allowed to stabilize. The output of the radiation detection instrumentation was monitored continuously throughout this sequence of events. The contribution of individual radiation levels associated with leak impingement, 2.00-inch duct, and heater surface were therefore isolated in events (1) thru (3). A room temperature background was established in event (4) such that the change in irradiance associated with individual radiation sources within the nacelle enclosure could be identified in events (5) through (7).
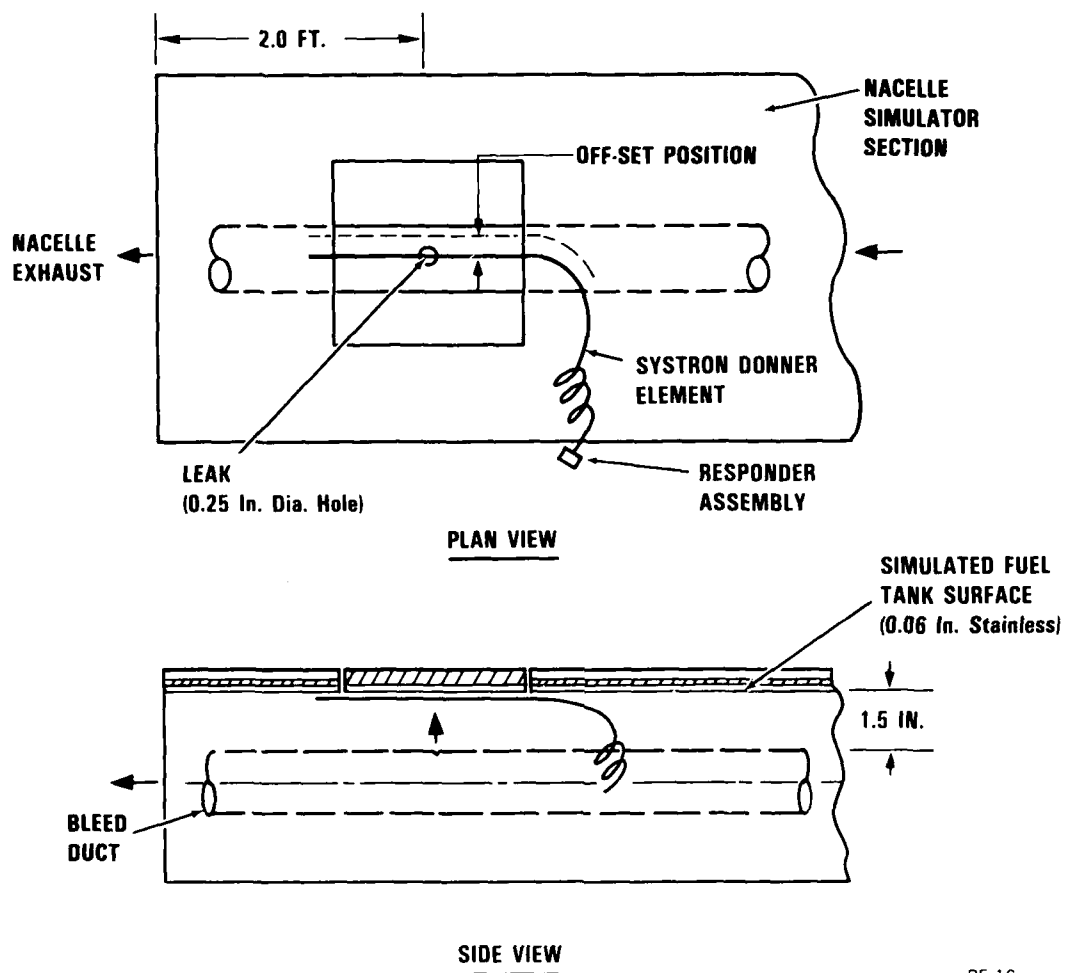
5.2.2 Systron-Donner Tests

The Systron-Donner element (Serial No. 2797) utilized in the tests were supplied by Mr. B. Nichols (Sacramento ALC) and incorporated an enhanced sensitivity over the original elements utilized in the F-111 engine nacelle. The current elements will indicate an overheat condition when heated to 675 F over an element length of 6.0-inches. The original elements, for reference, required heating of an 18.0-inch length to 675 F to indicate an overheat condition. In addition, the element will

68

detect an overheat condition when heated to a temperature of 350 F over its entire length.

The element consists of a responder assembly and sensor element. The responder assembly contains the pressure-activated electrical switches and the electrical connector for system interface and serves to actuate the warning device when the sensor element detects an alarm condition. The sensor element consists of a sealed tube containing a fixed amount of ambient helium gas and a central gas-releasing core wire. The sensor element is assembled to the responder to create a sealed assembly for containment of the helium gas. The sensor element has a diameter of 0.03-inch and a length of 19.0 feet.

The element was subjected to a functional checkout test before installation in the nacelle/bleed duct simulator, to insure that the unit was operational and to verify that the technique utilized to establish leak detectability was well-established before actual usage of the element to evaluate leak detection. The resistance of the element was measured at room temperature with a Hewlett-Packard 3465-A digital multimeter (200 KOHMS full scale) and found to be 98.0 KOHMS. The element was then placed in a furnace and heated to a temperature of 350 F. When the temperature of the element reached 350 F, the resistance of the element changed abruptly to zero OHMS which indicated that the pressure switch in the responder assembly had closed, and would have indicated an overheat condition if connected to the F-111 cockpit alarm system. This functional checkout procedure was recommended by the element manufacturer as a reliable checkout procedure for the element.

The Systron-Donner element was then installed in the bleed duct/nacelle simulator as shown schematically in Figure 16. Approximately one foot of the element was attached to the upper surface of the simulated fuel tank surface (0.06-in. stainless steel) and the remaining length (18.0 feet) was coiled such that

Figure 16. Systron-Donner test installation.

it was exposed to the nacelle airflow. The element was positioned (initial test) directly above the leak opening (0.25-in.-diameter hole) and 1.5 inches above the top surface of the bleed duct. Upon completion of the initial test, the one-foot section of the element was offset 0.5-inch and 1.0-inch from the duct centerline, as shown in Figure 16. The installation of the element, with the exception of the offset, remained the same as employed in the initial tests.

Simulated bleed leak tests were conducted with the Systron-Donner element at the M=1.2 (sea level) flight condition utilizing the test procedure identified in Section 5.2.1. Tests were conducted with the element located directly above the leak for leakage flow rates of 4.8 and 11.8 lb/min. Additional tests at a leakage flowrate of 11.8 lb/min were also performed with the element offset 0.5 and 1.0-inches from the leak. The results of all tests are presented in Section 5.3.3.
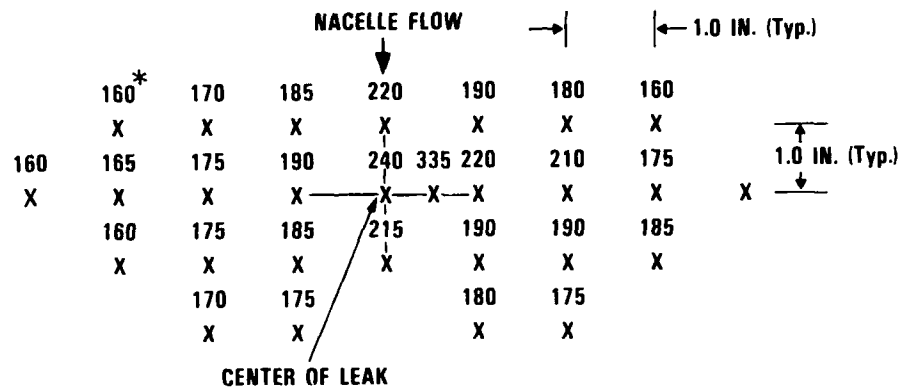
5.3 Test Results

The test results from both the IR detection tests and Systron-Donner cable element tests are presented in the following paragraphs. In addition, test results for the thermal response of the stainless steel surface exposed to the leakage flow are also discussed.

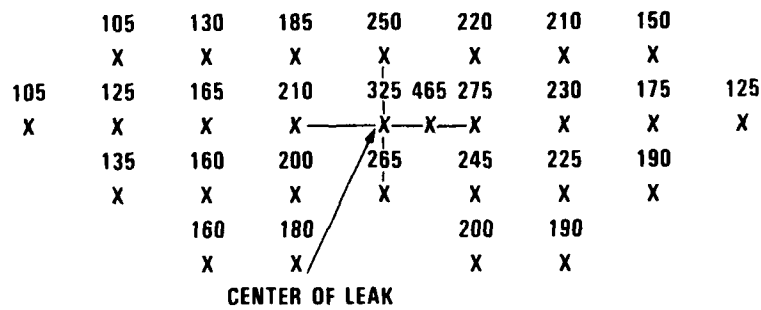### 5.3.1 Thermal Response of Stainless Steel Plate

The thermal response of the stainless steel plate (simulated fuel tank surface) located directly above the simulated leak (0.25-inch-diameter hole) is presented for the M=0.0 (idle power), M=0.75 (40.0K ft), and M=1.2 (sea level) conditions in Figure 17.

The data is presented in terms of equilibrium temperatures achieved after exposure to the leak at 28 locations on the plate, as determined from thermocouples on the plate.
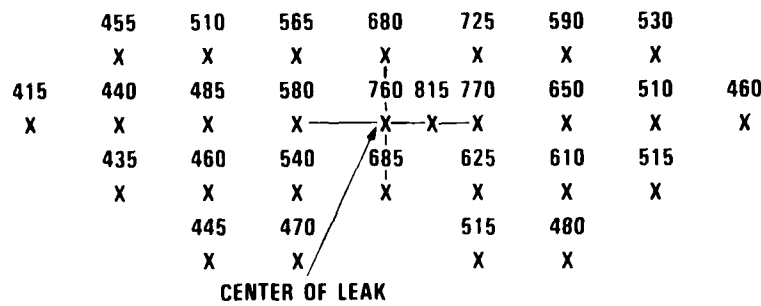
The results for the M=0.0 (idle power) condition are based on results from Run 3 which incorporated a leakage flowrate of 2.4 lb/min at a temperature of 435 F. The plate is observed (Figure 17) to reach a maximum temperature of 335 F at 0.5-inch from the leak centerline which indicates that the leak was inclined slightly with respect to the plate. The average temperature of a 2.0-inch by 2.0-inch area centered above the leak is 204 F and represents, based on an initial temperature of 90 F (nacelle airflow temperature at this condition), a change in temperature of 114 F. The results for the M=0.75 (4.0K ft) are based on the results from Run 2 which incorporated a leakage flow of 1.90 lb/min at a temperature of 595 F. The plate is observed to reach a maximum temperature of 465 F in the same location as noted previously for the M=0.0 (idle power) condition. The average temperature of a 2.0-inch by 2.0-inch area centered directly above the leak is 242 F and represents, based on an initial temperature of 75 F, a change in temperature of 167 F for this area. The

72

NACELLE FLOW   →| |←— 1.0 IN. (Typ.)

```
       160*  170   185   220   190   180   160
        X     X     X     X     X     X     X                    ↑
 160   165   175   190  240 335 220   210   175          1.0 IN. (Typ.)
  X     X     X     X————X—X—X   X     X      X ——        ↓
       160   175   185  /215   190   190   185
        X     X     X   X     X     X     X
             170   175           180   175
              X     X /           X     X
```

CENTER OF LEAK

RUN 3 (M = 0.0, S.L.)

```
       105   130   185   250   220   210   150
        X     X     X     X     X     X     X
 105   125   165   210  325 465 275   230   175   125
  X     X     X     X————X—X—X   X     X     X
       135   160   200  /265   245   225   190
        X     X     X   X     X     X     X
             160   180           200   190
              X     X /           X     X
```

CENTER OF LEAK

RUN 2 (M = 0.75, 40 KFT)

```
       455   510   565   680   725   590   530
        X     X     X     X     X     X     X
 415   440   485   580  760 815 770   650   510   460
  X     X     X     X————X—X—X   X     X     X
       435   460   540  /685   625   610   515
        X     X     X   X     X     X     X
             445   470           515   480
              X     X /           X     X
```

CENTER OF LEAK

RUN I-D (M = 1.2, S.L.)

*— All Temperatures in °F

RI 19

Figure 17. Temperature distributions resulting from leak.

73

results for the M=1.2 (sea level) condition are based on the results from Run 1-D which incorporated a leakage flow of 11.7 lb/min at a temperature of 825 F. The average temperature of a 2.0-inch by 2.0-inch area in this case is 660 F and represents, based on an initial temperature of 267 F, a temperature change of 392 F for this area.

5.3.2 Optical Measurements of the Bleed Duct Leak

5.3.2.1 Radiometric Analysis Packages' (RAPs') Results

The records for the RAP detector outputs are attached in Appendix C. Some output channels are not presented, as will be discussed later.

One term which needs to be defined again is "hot spot". The "hot spot" temperature refers to average temperature (based on nine thermocouple measurements) of a standard (2.0-inch by 2.0-inch) area which was located directly above the leak orifice (when the leak orifice was oriented normal to the impingement surface). The FOV of the RAPs and the ESP was centered about this area.

Tests 1, 1A, and 1B were conducted to determine the RAP detectors' offset voltages resulting from exposure to the test environments (i.e., the three simulated flight conditions). Test 1 investigated the offset associated with the detector electronics operating at room temperature (with water flowing through each RAP). The offset voltage(s) measured during this test defined the zero line(s) which the detector outputs from the ground idle and M=0.75 tests were referenced against. We felt that this was a reasonable approach since the ambient temperature (hence, the thermopile cold junction temperature) during the ground idle and M=0.75 tests remained very near room temperature (70±5 F). Also, during Test 1, several simulated bleed duct leaks were created (with the nacelle test fixture at room temperature and with the

nacelle test fixture at high temperature, simulating a M=1.2 sea level dash). We found during this testing that the time for a measurable "hot spot" to establish itself from impinging hot air took several minutes. Therefore, the channels which used the AC coupled amplifiers (thermopile channels 2, 4, 6, 8, 10, and 12 and the PbSe and pyroelectric channels) were of little use since their associated time constants were much less than several minutes. Therefore, these channels were not used in subsequent tests.

Test 1A was intended to determine the electrical offset associated with the high-temperature environment, the M=1.2 condition. Test 1B was performed since the RACAL recording system's sensitivity for Test 1A was not on an appropriate range. During this test series, protective blanking covers were placed over the detectors so that they could not receive radiation from the background; however, the blanks were free to re-emit radiation since the temperature fluctuates with the test environments' temperature (just as the FOV limiter's temperature fluctuates). The blanking covers reached 151 F during the M=1.2 simulation. The voltages which were measured during this test sequence defined the offset for each RAP detector which the subsequent M=1.2 tests were referenced against. Note, the actual offsets which should be used are actually lower since the FOV limiter only affects a fraction of what a detector sees, whereas the blanking covers completely obscure the detector's field-of-view. Therefore, the re-emission of radiation from the blanking covers (hence, the offset voltage) is more significant than the re-emission of radiation from only the FOV limiters. For this reason the irradiance levels must be considered approximate. The difference between the irradiance before and during the introduction of a leak, however, should be fairly accurate since the temperature of the FOV limiters and the RAP package (with the thermopile cold junctions) remained constant at 151 F before and during a bleed duct leak.

To "calculate" an irradiance value, the offset voltage was

75

first subtracted from the measured detector output. Using the voltage result, an irradiance value was determined from the calibration curves of Appendix A. (The thermopile calibration curve had to be extrapolated to accommodate the higher output voltages.) This irradiance value was then divided by the appropriate filter bandwith transmission factor (identified in Appendix B for each filter which was used). This compensated for the transmission losses associated with the IR bandpass filters (note, detector calibration was not performed with filters in place). The result is the irradiance value reported.

Test 1C was intended to measure the spectral radiation levels associated with the simulated M=1.2 flight condition, but after the introduction of the bleed duct leak, it was noticed that the bleed duct temeprature dropped from 575 F to approximately 500 F. Since the bleed duct contributes such a large percentage of the back-ground irradiance, the RAP detectors initially saw less radiation instead of more after the introduction of the leak. To minimize this anomaly, a restricting orifice was installed in the dump valve line upstream of the two inch bleed duct and the one half inch leak line as previously discussed in Section 5.2.1.

After performing these tests, it was observed that the channels which monitored the 2.348+0.293 microns and 4.402+0.081 microns were not operating properly. It is not known at present what the malfunctions were. It is also not known when these malfunctions occurred. The outputs from these two channels are, therefore, not presented in Appendix C.

A typical output of RAP channel 1 (Ge, 2-14 microns), in terms of output voltage versus time, for the M=1.2 (sea level) condition is presented in graphical form for Test 1D and part of Test 1E in Figure 18. Irradiance calculations were performed at discrete times, based on the procedure discussed previously, as indicated in Figure 18. The results are summarized in Table 5 of this test. In addition, all other pertinent test variables are

76
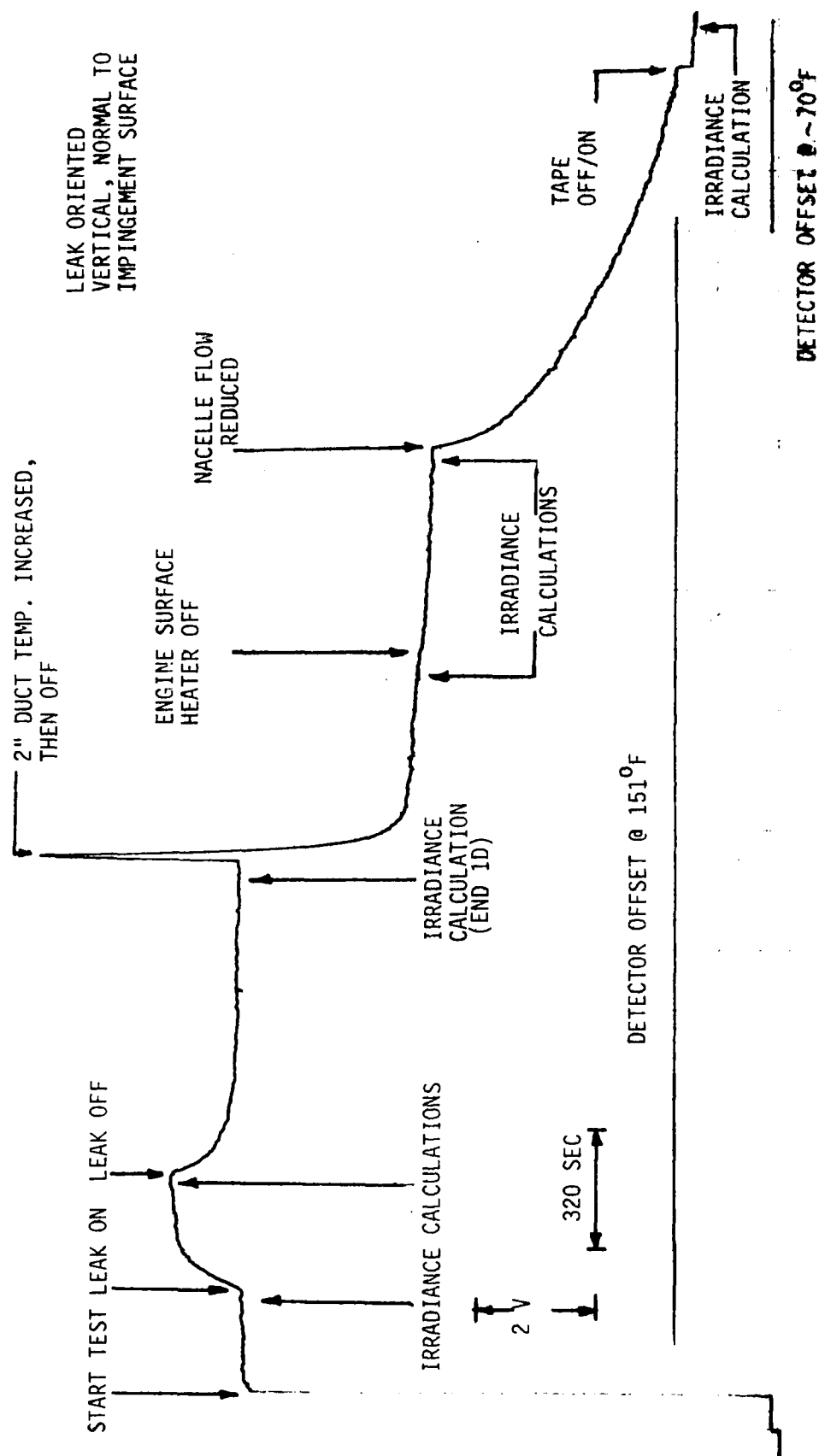
Figure 18. Output of Channel 1 (Ge, 2-14 μm) for Test 1D and 1E (M=1.2).

TABLE 5. M=1.2, SEA LEVEL DASH WITH VERTICAL LEAK.

TEST #	AVG. ENGINE CASE TEMP. (°F)	NACELLE AIR TEMP (°F)	NACELLE AIR FLOW (#/MIN)	BLEED DUCT TEMP (°F)	BLEED DUCT FLOW	BLEED LEAK AIR TEMP (°F)	BLEED LEAK AIR FLOW (#/MIN)	AVG. HOT SPOT TEMP. (°F)	APPROX. IRRADIANCE (mW/cm²) PER WAVEBAND COATED Ge 2-14µm	3.690 ±.317µm	4.745 ±.244µm	9.597 ±2.113µm	COMMENTS
1D	339	263	266	470	ON	-	0	280	16.13	2.25	0.90	6.82	M=1.2 OPERATING CONDITION
1E	339	263	266	465*	ON	825	11.7	612	18.28	2.94	1.15	7.84	BLEED LEAK PRESENT
	339	263	266	470	ON	-	0	280	16.13	2.25	0.90	6.82	BLEED LEAK OFF
	339	263	266	285	OFF	-	0	275	11.02	1.56	0.77	5.00	BLEED DUCT OFF
	339	263	266	285	OFF	-	0	270	10.22	1.56	0.77	4.71	ENGINE CASE HEATER OFF
	339	90	40-60	110	OFF	-	0	110	3.65	2.25	3.02	1.42	NACELLE AIR FLOW LOWERED
	339	90	40-60	335	OFF	820	11.7	~600	13.01	4.88	4.99	5.80	BLEED LEAK WITH COOLER NACELLE
	290	90	40-60	105	OFF	-	0	150	3.65	1.59	2.21	1.37	BLEED LEAK OFF
	230	90	40-60	830	ON	-	0	185	SAT.	--	--	--	BLEED DUCT ON, TOO HOT
	190	90	40-60	480	ON	-	0	135	11.18	2.63	3.19	4.21	BLEED DUCT TEMP. LOWERED
	165	90	40-60	100	OFF	-	0	100	--	--	--	--	BLEED DUCT OFF; EQUIL. NOT MET
	170	90	40-60	100	OFF	-	0	90	--	--	--	--	ENGINE CASE HEATER ON
	260	90	40-60	110	OFF	-	0	80	--	--	--	--	NACELLE AIR OFF; EQUIL. NOT MET
	340	90	0	130	OFF	-	0	115	≥5.21	≥1.19	≥1.87	≥2.39	ENGINE CASE HOTTER
1F	358	267	263	495	ON	-	0	290	16.59	3.94	2.16	7.35	M=1.2 OPERATING CONDITION
	358	267	263	480*	ON	840	11.3	602	18.28	4.44	2.32	8.07	BLEED LEAK PRESENT
	358	267	263	505	ON	-	0	320	17.16	3.94	2.32	7.62	BLEED LEAK OFF
	358	267	263	290	OFF	-	0	280	10.75	2.94	1.57	5.40	BLEED DUCT OFF
1G	346	265	134	290	OFF	-	0	280	10.00	0.94	0.77	5.00	NACELLE AIR FLOW LOWERED
	346	265	134	615	ON	-	0	300	20.00	2.13	1.15	8.52	BLEED DUCT ON
	346	265	134	535	ON	880	10.4	586	20.97	2.44	1.45	9.38	BLEED LEAK PRESENT
	346	265	134	620	ON	-	0	330	20.29	2.13	1.15	8.81	BLEED LEAK OFF
	346	265	134	285	OFF	-	0	280	10.11	0.34	0.25	5.51	BLEED DUCT OFF

* Bleed duct temperature initially dropped ~25°F, then went to reported temperature.

78

summarized in Table 5 for the remaining M=1.2 (vertical leak) tests.

The results in Table 5 for Run 1D indicate, based on the 2 to 14 micron waveband (coated Ge) and ignoring reemitted radiation contributions from the FOV limiters, the irradiance of the environment with all heated sources present was 16.13 mW/cm^2. When the leak was introduced, the irradiance increased to 18.28 mW/cm^2; thus, the leak contributed approximately 2 mW/cm^2 of incident radiant energy at the detector. The irradiance data for the other three channels also indicate an increase in irradiance as the leak is introduced. The change in irradiance produced by the leak is therefore definitely detectable at this condition. The analytical model developed in Section 2.3 was utilized to predict the change in irradiance for the test conditions of Run 1D. The predictions were based on the actual temperature distributions resulting from the leak (Figure 17) and assumed radiation properties for the participating surfaces. The model predicted 15.4 mW/cm^2 before the leak was introduced for the 2 to 15 micron waveband; the measured value was 16.13. After the leak was introduced, the model predicted 16.0 mW/cm^2 of radiant energy, a net percent increase of almost 4.0%. The measured radiant percent increase was approximately 13% after the leak was introduced. The agreement between the measured and calculated results was deemed satisfactory and provided additional confidence in the experimental observations.

During Test 1E, an attempt was made to quantify each source of radiation (i.e. the heated surface simulating the engine case, the bleed duct, the "hot spot" created by the leak, and the surfaces heated by the nacelle air) when the RAPs were at high-temperature (simulating the M=1.2 condition) and at room temperature (roughly simulating the M=0.75 and M=0.0 condition). Part of Test 1E is presented on the Test 1D chart; the conclusion of 1E is presented on a second chart.

79

When only the simulated engine case heater and the heated air flow were present, the irradiance was 11.02 mW/cm^2, indicating that the bleed duct steady-state irradiance contributed about 5 mW/cm^2 (16.13-11.02). When the engine case heater was shut off, the 263 F air measured 10.22 mW/cm^2 (note, the 263 F air heated all structures to approximately 263 F). Therefore, the engine case heater only contributed 0.8 mW/cm^2 (11.02-10.22) of radiant energy at the RAP detectors; however, the detectors were focused near the fuel tank structure, away from the engine case. Based on these values, it becomes clear how dominant the background is that an optical detector must discriminate against.

After the radiation sources were measured at high-temperature and airflow, the flowrate and temperature of the nacelle air was reduced, and these same isolated radiation sources were measured again. A low air flow was utilized (40 to 60 pounds per minute) to minimize convective heat transfer from the leak to the detectors. The steady-state temperature of the nacelle components was approximately 110 F when an 820 F leak was introduced. The resulting irradiance was 9.36 mW/cm^2 (13.01-3.65). Similary, when the other components were introduced their irradiances under similar conditions as the M=1.2 test above were 11.18 mW/cm^2 for the bleed duct at 480 F and at least 5.21 mW/cm^2 for the engine case (the engine heated surface may not have reached equilibrium). Unfortunately, the 263 F air was not measured with the detector at 110 F primarily due to the logistics involved and the extremely small signal expected. Since the cold junction temperature of the RAPs was much lower (151 versus approximately 75 F), the increase in measured output voltage (irradiance) was expected. The reason the "hot spot" and engine case irradiance increased so drastically (2 versus 9 mW/cm^2 and 0.8 versus approximately 5 mW/cm^2, respectively) was most likely due to the increased RAP detector's sensitivities and to some convective and conductive heat transfer to the RAPs.

It was noted during Test 1D/E that the bleed duct temperature

80

still dropped about 25 F immediately after the introduction of the bleed leak. However, after about two to three minutes, the bleed duct returned to near its pre-leak temperature.

Under similar conditions to Test 1D, Test 1F was performed to check the repeatability of the measurements. As can be seen in Table 5, the results were similar. The slightly high temperature(s) of the nacelle background in Test 1F (primarily, the bleed duct) seemed to have greater effect on the narrowband channels than on the broadband measurements. For this reason and the fact that the broadband channel generated the most measurable signals, the 2 to 14 micron waveband's results are emphasized and discussed in greater detail throughout this report. This channel indicated that the incident background radiation before the bleed leak was present was 16.13 mW/cm^2 for Test 1D and 16.59 mW/cm^2 for 1F. After the leak was introduced, the irradiance increased to 18.28 mW/cm^2 for both tests. After the leak was removed, the coated Ge channel returned to 16.13 mW/cm^2 for Test 1D; however, Test 1F did not return to its pre-leak irradiance. Instead, it decreased to 17.16 mW/cm^2. The reason was that the background environment did not return to its pre-leak temperature(s) as it did for Test 1D. The bleed duct and the area where the "hot spot" resides were at higher temperatures for the post-leak irradiance calculation than they were for the pre-leak calculation for Test 1F. Nevertheless, the repeatability of the test was deemed acceptable.

During Test 1G, the nacelle air flow was again reduced, but for a different reason than in Test 1E. It was hoped that the air flow rate would permit the bleed duct temperature to increase (more representative of the actual F-111 M=1.2 condition). As can be seen from Table 5, the temperature did indeed increase, as did the resultant irradiance (from approximately 16 to 20 mW/cm^2). However, the drop in temperature after the introduction of the bleed leak was also more dramatic. Even so, the coated Ge channel still measured an appreciable increase (almost 1.0 mW/cm^2) in incident radiant energy from the introduction of the bleed leak.

81

Tables 6 and 7 illustrate the M=1.2 (sea level) results from Tests 4, 4A, and 7 for the leak oriented ±45 degrees from a vertical plane (i.e., toward and away from the ESP, respectively). There does not appear to be a significant difference for these tests' pre-or post-leak irradiance values over the respective values observed during Test 1D and 1F. However, Tests 4, 4A, and 7's measured irradiances during their bleed leak were slightly lower than in earlier tests. As indicated by their lower "hot spot" temperature, the radiation emitted by this standardized area (which was the RAPs' approximate centerline field-of-view) was less. The "hot spot's" location had shifted. The change in irradiance from the introduction of the leak was still appreciable though, as in the Test 1 series. This observed result verifies that optical detection of bleed duct leaks can offer large area coverage benefits (90 degrees of the 360 F bleed duct circumference, for this particular case).

It is worth noting that the bleed duct temperature drop earlier observed during the introduction of the bleed leak was not experienced for Test 4 and 4A (based on the thermocouple measurement data taken at one minute intervals). Instead, the duct appeared to increase in temperature. The reason for this is unclear. Since only the thermocouple which was located downstream of the bleed leak was used, it was thought that the hot air from a leak was convectively reheating the duct; however, no rational scenario to support this could be established.

The results from the M=0.75 flight condition with a leak oriented vertically (Test 2) are illustrated in graphical form in Figure 19 and summarized in tabular form for all the wavebands in Table 8. As expected, the observed broadband irradiance values were less than the M=1.2 tests. As not expected though, the incident radiant energy at the detectors decreased after the introduction of the leak. We first thought that the bleed duct dropped in temperature after the leak was present, as observed

TABLE 6. M=1.2, SEA LEVEL DASH WITH LEAK -45° (I.E. TOWARD THE ESP)

TEST #	AVG. ENGINE CASE TEMP. (°F)	NACELLE AIR TEMP (°F)	NACELLE AIR FLOW (#/MIN)	BLEED DUCT TEMP (°F)	BLEED DUCT FLOW	BLEED LEAK AIR TEMP (°F)	BLEED LEAK AIR FLOW (#/MIN)	AVG. HOT SPOT TEMP. (°F)	APPROX. IRRADIANCE (mW/cm² per waveband) COATED Ge, 2-14µm	3.690 ±.317µm	4.745 ±.244µm	9.597 ±2.113µm	COMMENTS
4	348	265	264	485	ON	--	0	285	16.29	3.25	1.15	6.99	M=1.2 OPERATING CONDITION
	348	265	264	530	ON	800	11.5	390	17.63	3.94	1.51	7.72	BLEED LEAK PRESENT
	348	265	264	560	ON	--	0	320	17.90	3.63	1.32	7.72	BLEED LEAK OFF
4A	345	263	266	480	ON	--	0	285	16.88	3.44	0.16	8.37	M=1.2 OPERATING CONDITION
	345	263	266	510	ON	785	11.4	363	17.63	3.94	0.32	9.09	BLEED LEAK PRESENT
	345	263	266	480	ON	--	0	~280	17.00	3.44	0.16	8.57	BLEED LEAK OFF

TABLE 7. M=1.2, SEA LEVEL DASH WITH LEAK +45° (I.E. AWAY FROM ESP)

TEST #	AVG. ENGINE CASE TEMP. (°F)	NACELLE AIR TEMP (°F)	NACELLE AIR FLOW (#/MIN)	BLEED DUCT TEMP (°F)	BLEED DUCT FLOW	BLEED LEAK AIR TEMP (°F)	BLEED LEAK AIR FLOW (#/MIN)	AVG. HOT SPOT TEMP. (°F)	APPROX. IRRADIANCE (mW/cm² per waveband) COATED Ge, 2-14µm	3.690 ±.317µm	4.745 ±.244µm	9.597 ±2.113µm	COMMENTS
7	355	267	263	490	ON	--	0	285	16.13	3.44	0.90	7.84	M=1.2 OPERATING CONDITION
	355	267	263	485*	ON	810	11.5	473	17.42	3.94	1.03	8.19	BLEED LEAK PRESENT
	355	267	263	495	ON	--	0	~300	16.59	3.94	1.03	7.84	BLEED LEAK OFF

*Bleed duct temperature initially dropped ~20°F, then went to reported temperature.
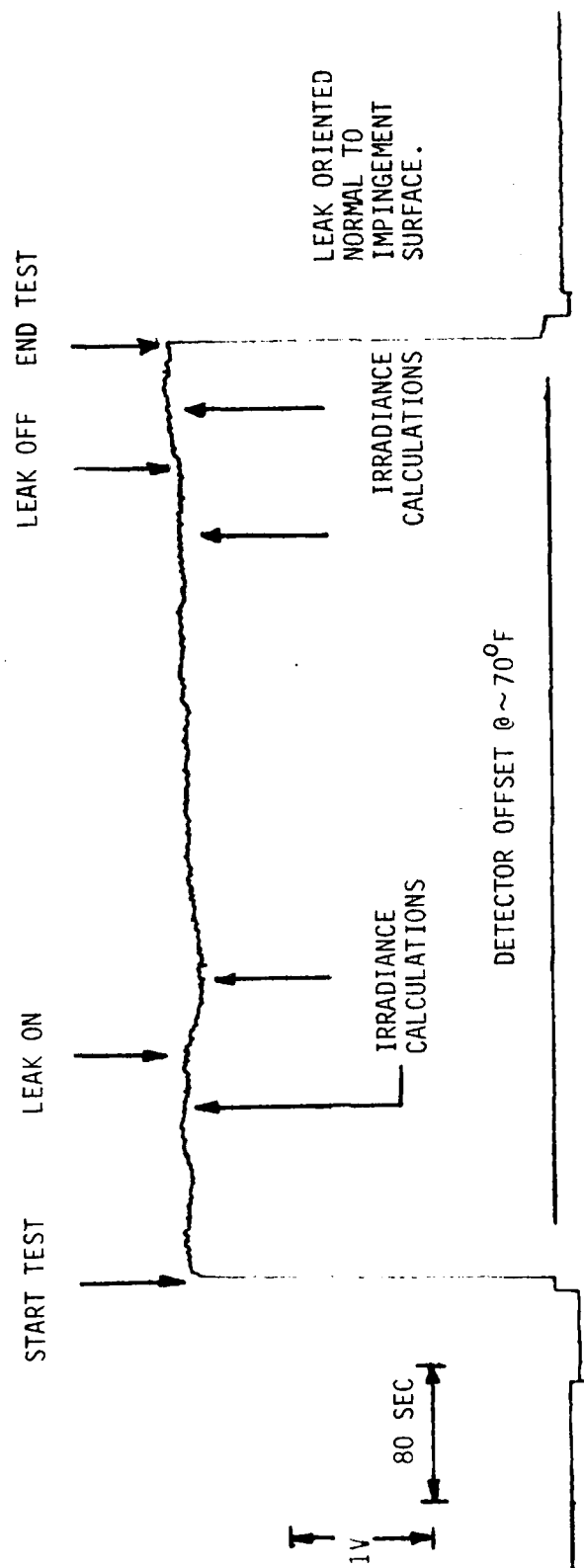
Figure 19. Output of Channel 1 (Ge, 2-14 μm) for Test 2 (M=0.75).
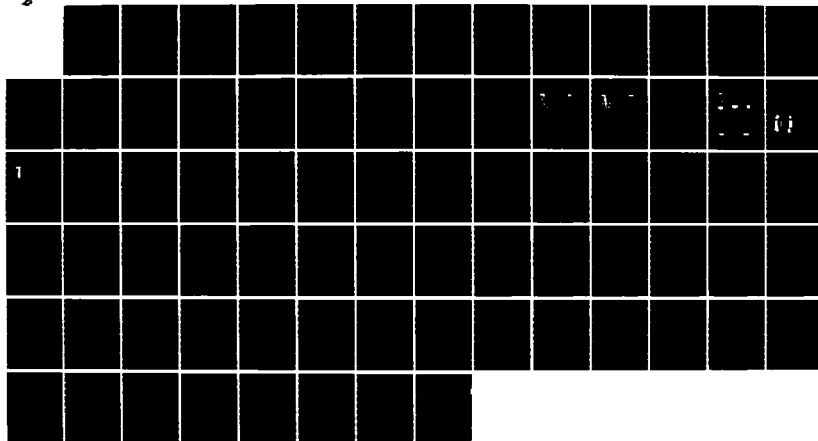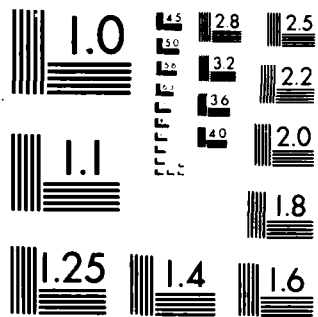
MICROCOPY RESOLUTION TEST CHART

NATIONAL BUREAU OF STANDARDS 1963 A

TABLE 8. M=0.75, 40,000 FEET ALTITUDE WITH VERTICAL LEAK

TEST #	AVG.ENGINE CASE TEMP. (°F)	NACELLE AIR		BLEED DUCT		BLEED LEAK AIR		AVG. HOT SPOT TEMP. (°F)	APPROX. IRRADIANCE (mW/cm² per waveband)				COMMENTS
		TEMP (°F)	FLOW (#/MIN)	TEMP (°F)	FLOW	TEMP (°F)	FLOW (#/MIN)		COATED Ge, 2-14μm	3.690 ±.317μm	4.745 ±.244μm	9.597 ±2.113μm	
2	167	75	248	310	ON	--	0	90	7.04	2.75	1.68	2.67	M=0.75 OPERATING CONDITION
	167 167	75 75	248 248	300 310	ON ON	580 595	1.9 1.9	~190 248	6.72 7.04	2.75 2.75	1.68 1.74	2.56 2.72	LEAK INTRODUCED LEAK CONDITION @ EQUIL.
	167	75	248	310	ON	--	0	95	7.20	2.75	1.74	2.72	BLEED LEAK OFF

TABLE 9. M=0.0, GROUND IDLE CONDITION WITH VERTICAL LEAK

TEST #	AVG.ENGINE CASE TEMP. (°F)	NACELLE AIR		BLEED DUCT		BLEED LEAK AIR		AVG. HOT SPOT TEMP. (°F)	APPROX. IRRADIANCE (mW/cm² per waveband)				COMMENTS
		TEMP (°F)	FLOW (#/MIN)	TEMP (°F)	FLOW	TEMP (°F)	FLOW (#/MIN)		COATED Ge, 2-14μm	3.690 ±.317μm	4.745 ±.244μm	9.597 ±2.113μm	
3	218	90	34	400	ON	--	0	130	8.22	2.44	2.89	3.01	M=0.0 OPERATING CONDITION
	218 218	90 90	34 34	315 315	ON ON	435 435	2.4 2.4	184 212	7.53 7.63	2.38 2.38	2.83 2.77	2.72 2.79	LEAK INTRODUCED LEAK CONDITION @ EQUIL.
	218	90	34	400	ON	--	0	165	8.12	2.38	2.77	3.01	BLEED LEAK OFF
3A	192	120	58	350	ON	--	0	140	8.76	4.56	5.72	3.58	M=0.0 OPERATING CONDITION
	192 192	120 120	58 58	320 350	ON ON	405 --	2.4 0	233 ~150	8.71 8.76	4.56 4.56	5.72 5.72	3.58 3.58	LEAK PRESENT BLEED LEAK OFF

earlier. The bleed duct thermocouple, however, indicated that the bleed duct temperature remained fairly constant. Due to this unexplained anomaly, the radiant energy incident upon the RAP detectors cannot be determined. It is masked by whatever caused the decrease in the nacelle background radiation emission. Nevertheless, it certainly appears that the signal from the leak was small.

The results from Test Series 3, the ground idle condition (M=0.0), are summarized in Table 9. Figure 20 illustrates the results in graphical form from a typical test. The irradiance levels were lower in magnitude than those experienced during the M=1.2 tests, as was the case during Test 2. Again, this is attributed to the cooler temperatures of the bleed duct and other surrounding nacelle structures. Also, as in Test 2, the irradiance levels dropped after the introduction of the duct leak. However, unlike Test 2, the bleed duct's temperature dropped after the introduction of the leak. Furthermore, it remained at this lower temperature until the leak was removed (unlike the Test Series 1). Because of this, the irradiance effects of the bleed leak are again lost. Again, the effects of the leak are felt to be small. It is worth noting, though, that the irradiance did slightly increase in Test 3 for the broadband channels after two to three minutes of leakage when all the temperatures were constant except the increasing "hot spot" temperature.

5.3.2.2 Environmentally Suitable Package's (ESP) Results

The records for the ECP's measurements can be found in Appendix D. The ESP detector was not calibrated since its sole function was intended to demonstrate that a solid-state optical device could operate in a high-temperature environment while still outputting discernable voltages for different engine compartment events, such as bleed duct leaks. Therefore, only output voltages are reported.
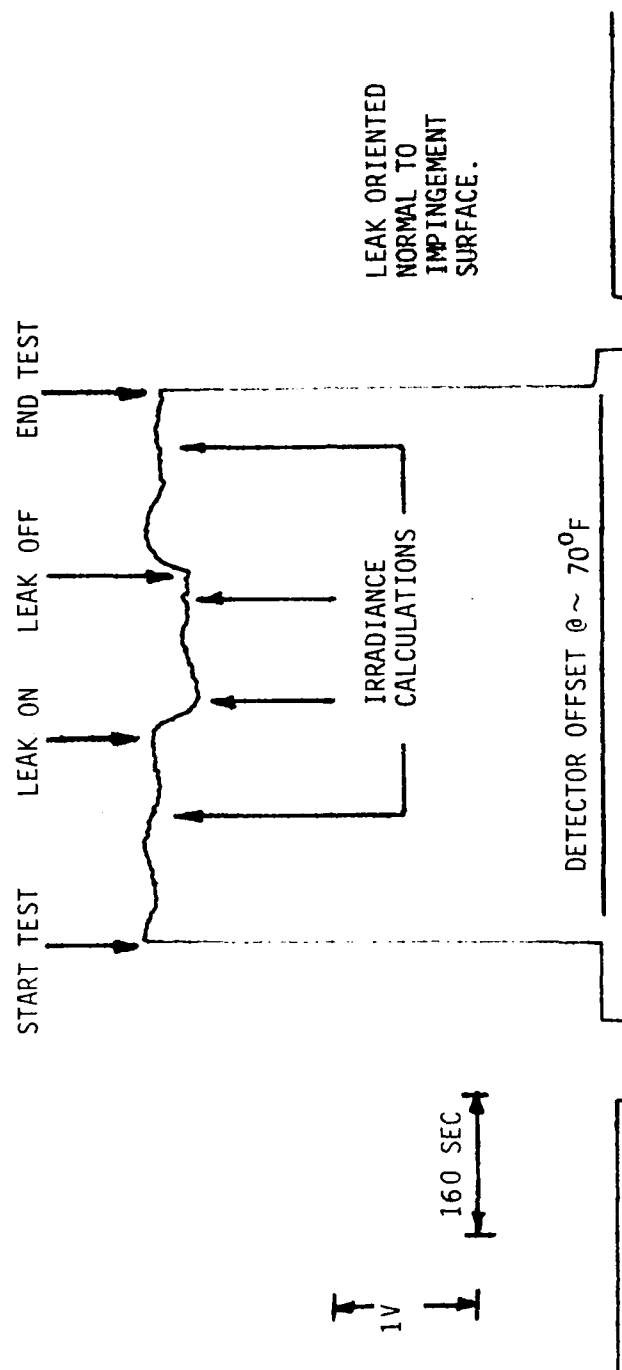
Figure 20. Output of Channel 1 (Ge, 2-14 μm) for Test 3 (M=0.0).

As Figure 21 illustrates, the ESP was as capable of operating and detecting bleed leaks as the water-cooled RAP detectors. For Test 1D the RAP's coated Ge channel changed 1.1 volts when the bleed leak was introduced. The ESP detector's output voltage changed 1.8 volts. The ESP detector ever recognized events that none of the RAP detectors recognized, as indicated in Figure 22. It is acknowledged that the output voltage was small (0.13 volts) and the ESP was closer to the leak event than the RAP, but it should also be noted that the ESP with its 95 degrees FOV had approximately the same amount of the bleed duct in its field-of-view as the RAPs. The ESP also had a smaller amplification gain.

Since irradiance values cannot be determined from the ESP data, only the output voltages are presented. Table 10 shows the output voltages for the RAP's coated Ge channel and the ESP. A quantitative comparison should not be made between these two detectors' outputs due to their different orientation (with respect to the leak source and background radiators), distance, FOV, sensitivity, and monitored wavebands. As can be seen, though, the ESP did give a discernable output signal for every bleed leak event except for Test 2's. Of course great care would have to be taken if an optical system were designed to trigger on such small signals as these (to negate a high false alarm rate).

Upon examining the ESP output data of Appendix D, it is apparent that the output voltage varied in a peculiar manner after the introduction of any test condition (e.g. airflow through the bleed duct, airflow through the nacelle, bleed leak, etc.). While the RAP detectors indicated a changing test condition by an exponential change in output voltage (reaching a steady-state voltage level), the ESP began responding exponentially but then changed. Apparently, the hot junction of the ESP's thermopile detector recognized the event in the same fashion as a RAP detector's hot junction. However, unlike the RAP detectors, the ESP's case temperature (hence, cold junction temperature) also changed due to the event. Thus, the cold junction temperature

88
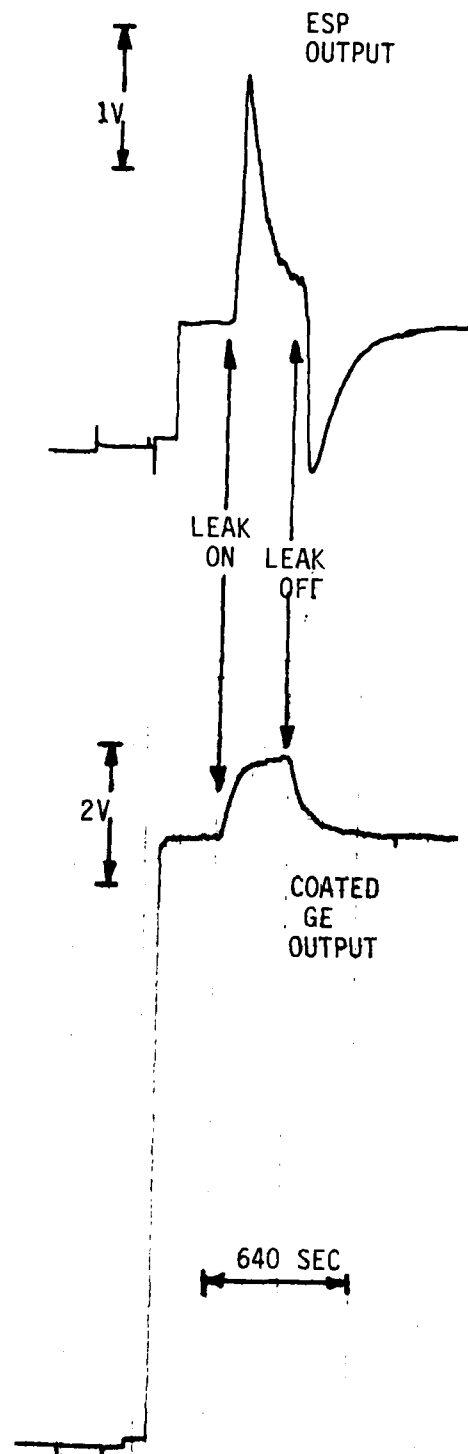
Figure 21. ESP and coated Ge channel output for Test 1D.
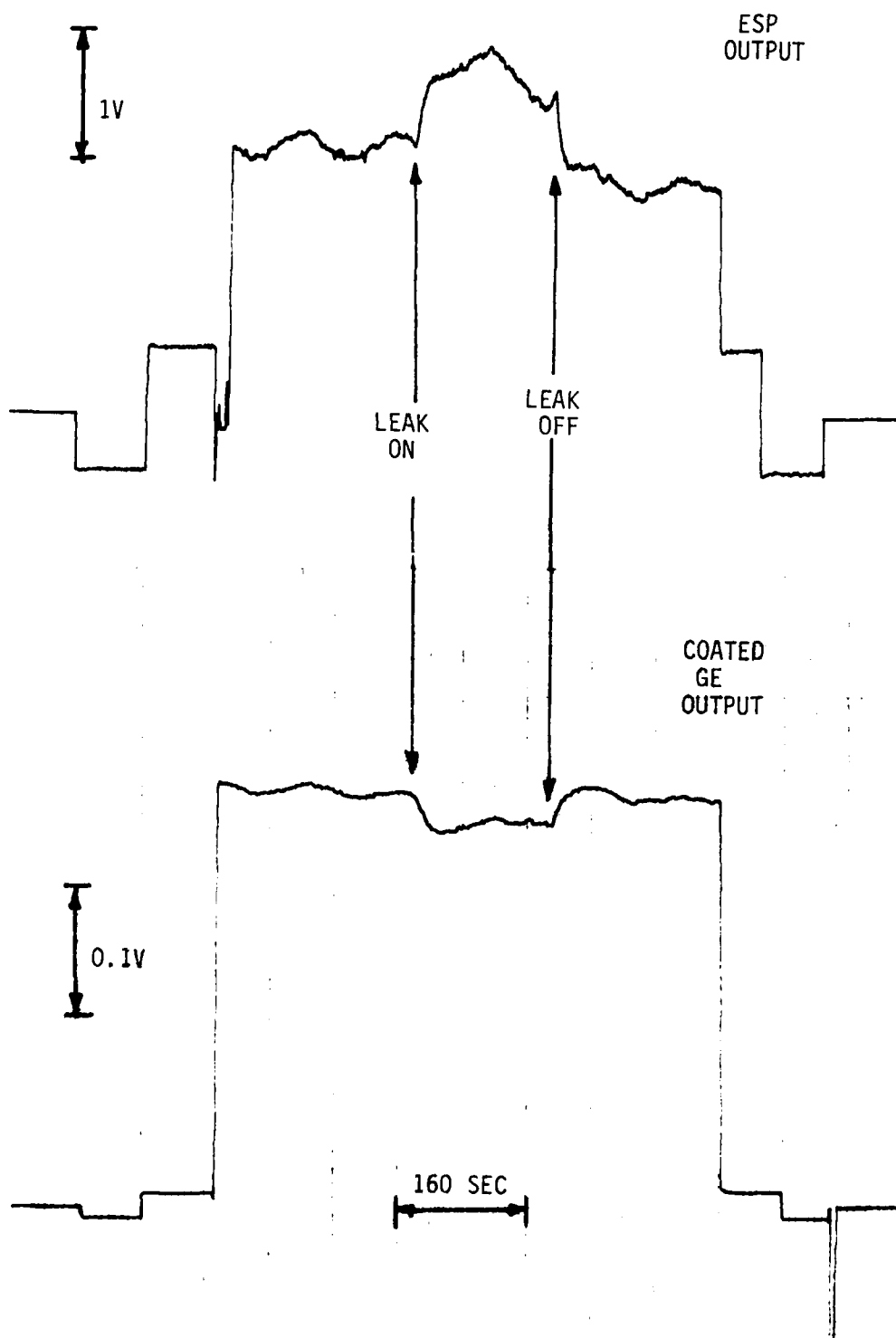
Figure 22. ESP and coated Ge channel output for Test 3.

90

Table 10. OUTPUT VOLTAGES FOR THE ESP AND RAP'S GE CHANNEL.

TEST #	TEST CONDITION	OUTPUT VOLTAGE CHANGE DUE TO IMPOSING CONDITION (VOLTS)	
		RAP's COATED Ge, 2-14 μm	ESP, 0.2-6 μm
1D	As specified in Table 5,		
	● Leak present	+1.1	+1.80
	● Leak off	-1.1	-1.35
1E	As specified in Table 5,		
	● Leak present (cooler nacelle)	+4.0	+4.75
	● Leak off	-3.9	-1.95
1F	As specified in Table 5,		
	● Leak present	+0.90	+1.25
	● Leak off	-0.60	-0.975
1G	As specified in Table 5, ● Leak present (hotter duct)	+0.60	+2.45
	● Leak off	-0.40	-1.175
2	As specified in Table 8,		
	● Leak present	-0.15	-0.075
	● Leak off	+0.05	+0.025
3	As specified in Table 9,		
	● Leak present	-0.30	+0.13
	● Leak off	+0.20	-0.15
3A	As specified in Table 9		
	● Leak present	-0.05	+0.04
	● Leak off	+0.05	-0.08
4	As specified in Table 6,		
	● Leak present	+0.7	+2.90
	● Leak off	+0.1	-1.05
4A	As specified in Table 6,		
	● Leak present	+0.45	+2.65
	● Leak off	-0.40	-0.575
7	As specified in Table 7,		
	● Leak present	+0.70	+0.275
	● Leak off	-0.50	-0.325

varied similarly to the hot junction but at a slower rate due to its higher thermal mass. This dictates that the ESP can only respond to engine events through transient (nonsteady-state) output signals. The source(s) of the ESP case's temperature increasing must have consisted at least partially of radiative and conductive heat transfer mechanisms (since the introduction of a bleed leak in a high airflow nacelle could not affect the convective heat transfer rate when this phenomena was observed). The removal/elimination of an event permitted the ESP hot junction to drop in temperature at a quicker rate than the cold junction. This explains the negative output voltage measurements. Eventually, however, both junctions were at or near the same temperature, and a null output was observed. The output voltages shown in Table 10 are the transient voltage changes observed soon after the introduction/removal of the bleed leak.

The results from the ESP indicate that an aircraft-suitable optical overheat detection system for engine compartment protection is realizable. Based on these results, a system of this type could provide at least ±45 degrees coverage around the bleed duct and be capable of responding to a small bleed duct leak within two minutes. A system of this type, as with most systems, might have difficulty detecting the leak at the M=0.75 and M=0.0 (ground idle) condition assuming the test conditions were representative simulations of the actual environment. However, it is felt that it could be done with proper safeguards.

5.3.3 Systron-Donner Test Results

Four separate tests were conducted with the Systron-Donner element installed in the bleed duct/nacelle simulator per the test procedure discussed in Section 5.2.2 for the M=1.2 (sea level) flight condition and the results are summarized in Table 11.

Runs 1-H and 1-I were conducted with the element located directly above the leak for flowrates of 4.8 and 11.8 lbs/min, respectively. The element did not detect the leak at a flowrate of 4.8 lb/min as evidenced by the fact that the resistance of the element remained unchanged at a value of 98 KOHMS during and after exposure to the leak. This indicates that there was not sufficient heating of the element to increase the helium gas pressure in the element to the required level to activate the pressure switch in the responder assembly. It may be recalled, based on the calibration procedure for the element discussed in Section 5.2.2, that the resistance of the element changes from 98 KOHMS to zero OHMS upon activation of the pressure switch. The leak was detected by the element for Run 1-I when the leakage flowrate was controlled to 11.8 lb/min. (Nominal flowrate utilized in the IR detection tests for the M=1.2, sea level, flight condition.)

The detectability at this condition was evidenced by a change in resistance from 98 KOHMS (before leak was introduced) to zero OHMS a short time after the exposure of the element to the leak. The leak was not detected for Run 1-J in which the element was offset 1.0 inches from the leak or in Run 1-K in which the element was offset 0.5-inch from the leak. The detectability for these conditions was again based on the fact that the electrical resistance of the element remained unchanged at a value of 98 KOHMS before and after the leak was introduced.

The Systron-Donner element did effectively detect the simulated leak (M=1.2, sea level flight condition) when a leakage

93

TABLE 11. SYSTRON-DONNER TEST RESULTS.

| FLIGHT CONDITION | RUN NO. | BLEED TEMP, °F | LEAKAGE FLOW RATE LB/MIN | NACELLE | | HEATER SURFACE TEMP. °F | SYSTRON-DONNER ELEMENT LOCATION | LEAK DETECTED |
				FLOW RATE LB/MIN	T °F			
M = 1.2 (Sea Level)	I–H	825	4.8	263	265	356	DIRECTLY ABOVE LEAK	NO
	I–I	840	11.8	266	264	370		YES
	I–J	835	11.8	267	263	373	OFF-SET 1.0 IN. FROM LEAK	NO
	I–K	840	11.6	266	267	353	OFF-SET 0.5 IN. FROM LEAK	NO

RF 17

94

flowrate of 11.8 lb/min was allowed to directly impinge upon the element. The detectability of the element for direct leak impingement is a function of leakage flowrate as evidenced by the fact that the leak was not detected at a flowrate of 4.8 lb/min. The Systron-Donner element, as expected, is not effective in detecting leaks in situations where the leak does not impinge directly on the element as indicated by the data of Runs 1-J and 1-H.

The angular coverage of the Systron-Donner element is therefore (based on the 0.5-inch offset test results) less than ±18 degrees since the coverage angle is defined by arctan (0.5/1.5). The IR detection techniques were found to provide at least ±45 degree angular coverage based on the test results discussed in Section 5.3.2 and therefore provide at least 2.5 times (45/18) greater angular coverage than the cable element for the respective test configurations used during this effort. It should be pointed out that regardless of where one places the Systron-Donner element around the circumference of the duct, the angular coverage will not change (i.e., it will always have less than ±18 degrees coverage around the duct). However, if the location of the IR sensor is modified to optimize its field-of-view around the bleed duct, its superior angular coverage can be further improved (greater than ±45 degrees).

The data in Table 10 also suggests that the Systron-Donner element would not detect leaks at the M=0.0 (ground static) or M=0.75 (40 K ft) conditions. This conclusion is based on the fact that the leak conditions for Run 1H (825 F leak at 4.8 lb/min) are more severe than the corresponding values for the M=0.0 and M=0.75 conditions. Based on the fact that at least one IR detector detected the effects of the hot air leak for the M=0.0 condition (the most difficult detection condition tested), the IR technique appears to be more capable of detecting leaks over a wider range of flight conditions than the cable elements.

95

SECTION 6

CONCLUSIONS AND RECOMMENDATIONS

A partial spectral signature was developed during this effort for a simulated F-111 engine nacelle environment. As a result, it was demonstrated that optical detection of engine compartment overheat events (such as bleed duct leaks) is feasible. Although an uncooled solid-state optical detection device was demonstrated during this effort, the practicality to aircraft application has not been sufficiently established. The practicality can only be established by designing and constructing a prototype system (using the information generated under this effort as a guide) and by determining its perforamnce and its assocaited penalties in a more realistic environment.

Conclusions from this effort are summarized as follows:

o We demonstrated that a properly designed IR sensor can satisfactorily operate in a heated environment at least as high as 265 F.

o Based on the test results, optical overheat detection can offer much more than 2.5 times greater angular coverage around the bleed duct than the conventional overheat system.

o The pneumatic continuous-loop overheat detection system only responded to the bleed duct leak under the simulated M=1.2 condition, and only when the hot air from the leak was directly impinging upon the continuous-loop cable. It is postulated based on the test results that the element would not detect a leak at the M=0.0 (ground static) or M=0.75 (40K ft) conditions.

o It appeared that at least one infrared detector was capable of
   recognizing the effects of every leak for every test condition.
   Although the M=0.0 (ground idle) condition generated extremely
   small leak signals, it was nevertheless, still observed.

      Based on the above findings, we recommend that a prototype
optical overheat detection system be developed. Realistic, large-
scale (or full-scale) tests that investigate whether this system
could reliably detect overheat events during ground idle and
M=0.75 conditions as well as other flight conditions should be
conducted. Also, it should be determined whether an optical
system can be suitably packaged for aircraft use without imposing
additional maintenance or logistic penalties.

REFERENCES

1. Springer, R. J., et al, "Advanced Ultra-Violet (UV) Aircraft Fire Detection System. - Volume I," AFWAL-TR-82-2062, August 1982.

2. Kern, M. T., Cinzori, R. J., Fuller, W. D., "Infrared Sensor for Detecting Bleed Air Leaks in Aircraft - Feasibility Study No. 2," Santa Barbara Research Center Report No. 40062, January 1984.

3. Private Communication, B. Nichols, Sacramento Air Logistics Center, September 1986.

4. Engineering Specification, "F-111 Aircraft Fire and Duct Failure Pneumatic Warning System," Sacramento ALC MMSRB 77-1, Revision 1, 29 April 1977.

5. Ozisik, M. N., "Radiative Transfer and Interaction with Conduction and Convection," John Wiley & Sons, Inc., New York, 1973.

6. Seigel, R. and Howell, J. R., "Thermal Radiation Heat Transfer," McGraw-Hill Book Co., New York, 1981.

7. Hornbeck, R. W., "Numerical Methods," Quantum Publisher, Inc., New Jersey, 1975.

8. McClure, J. D., Springer, R. J., "Environmental and Operating Requirements for Fire Extinguishing Systems on Advanced Aircraft," AFAPL-TR-73-122, September 1974.

9. Harper, C. T., Knezek, R. A., "F-111D Environmental Control System Design Analysis and Description - Refrigeration and Control Set," General Dynamics Report No. FZA-12-8004, 8 April 1971.

APPENDIX A

Detector Calibration Curves
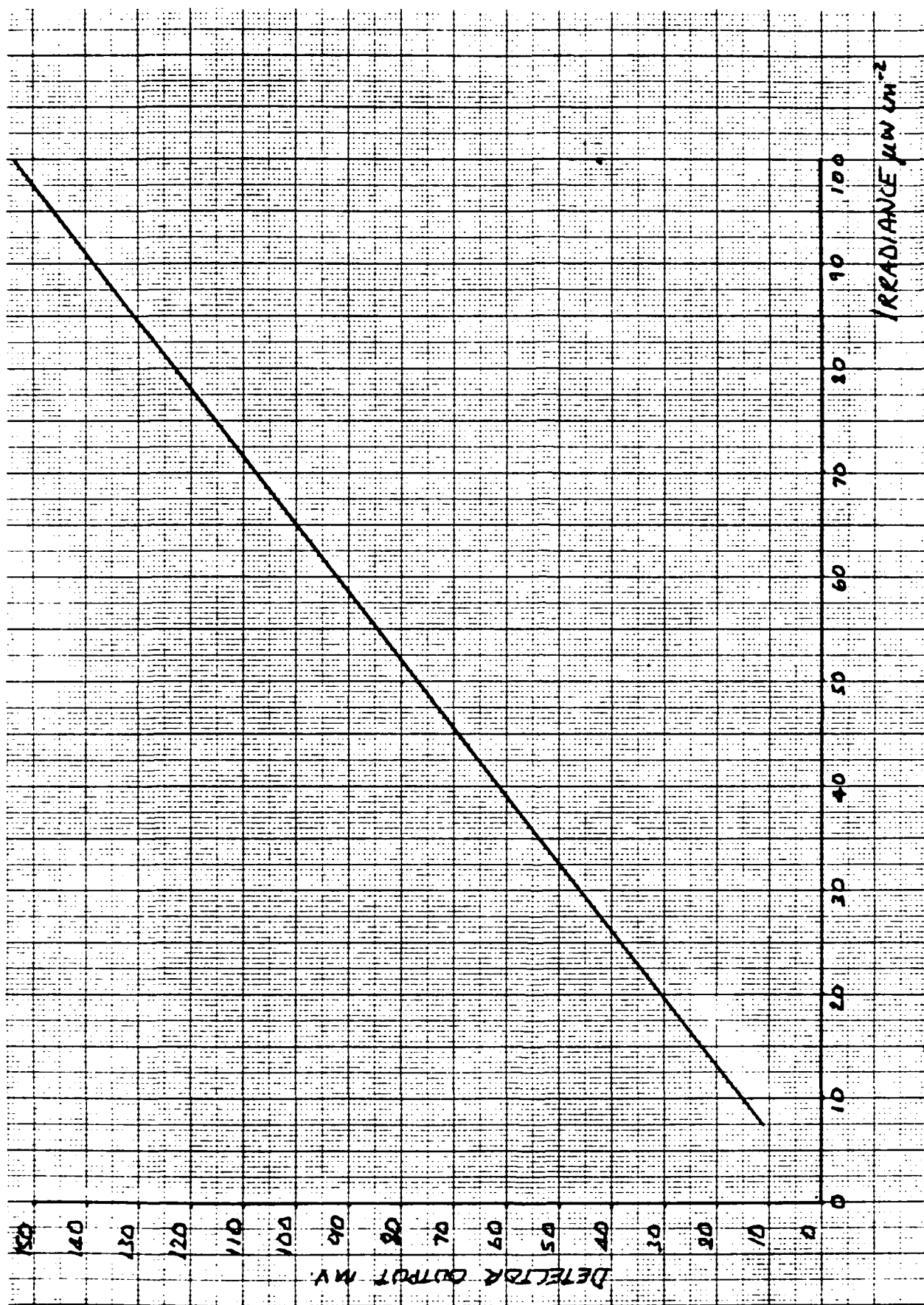
Figure A-1 RAP Lead Selenide Detector Calibration

Figure A . . RAP Thermopile Calibration
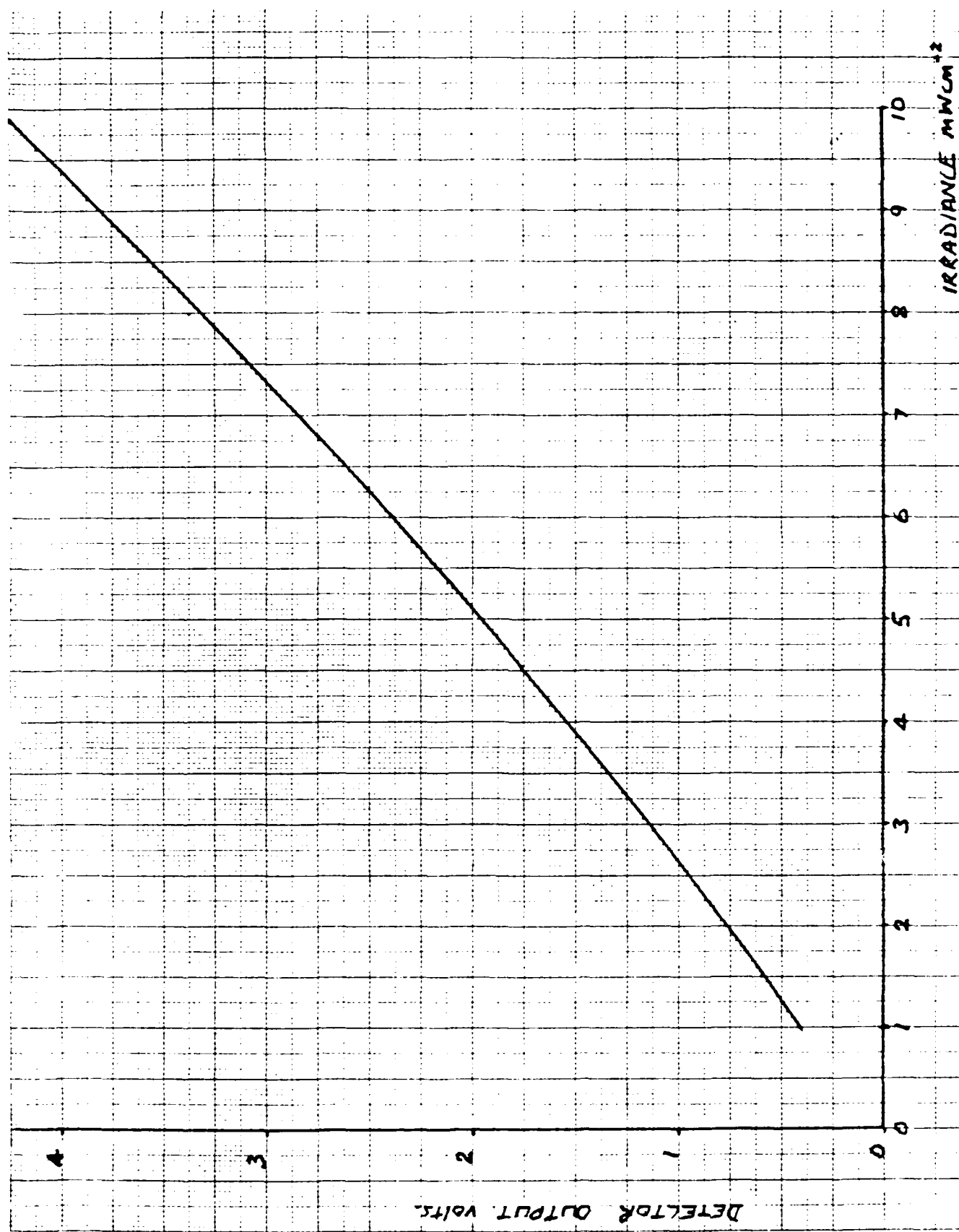
Figure A-3 RAP Thermopile Calibration

104
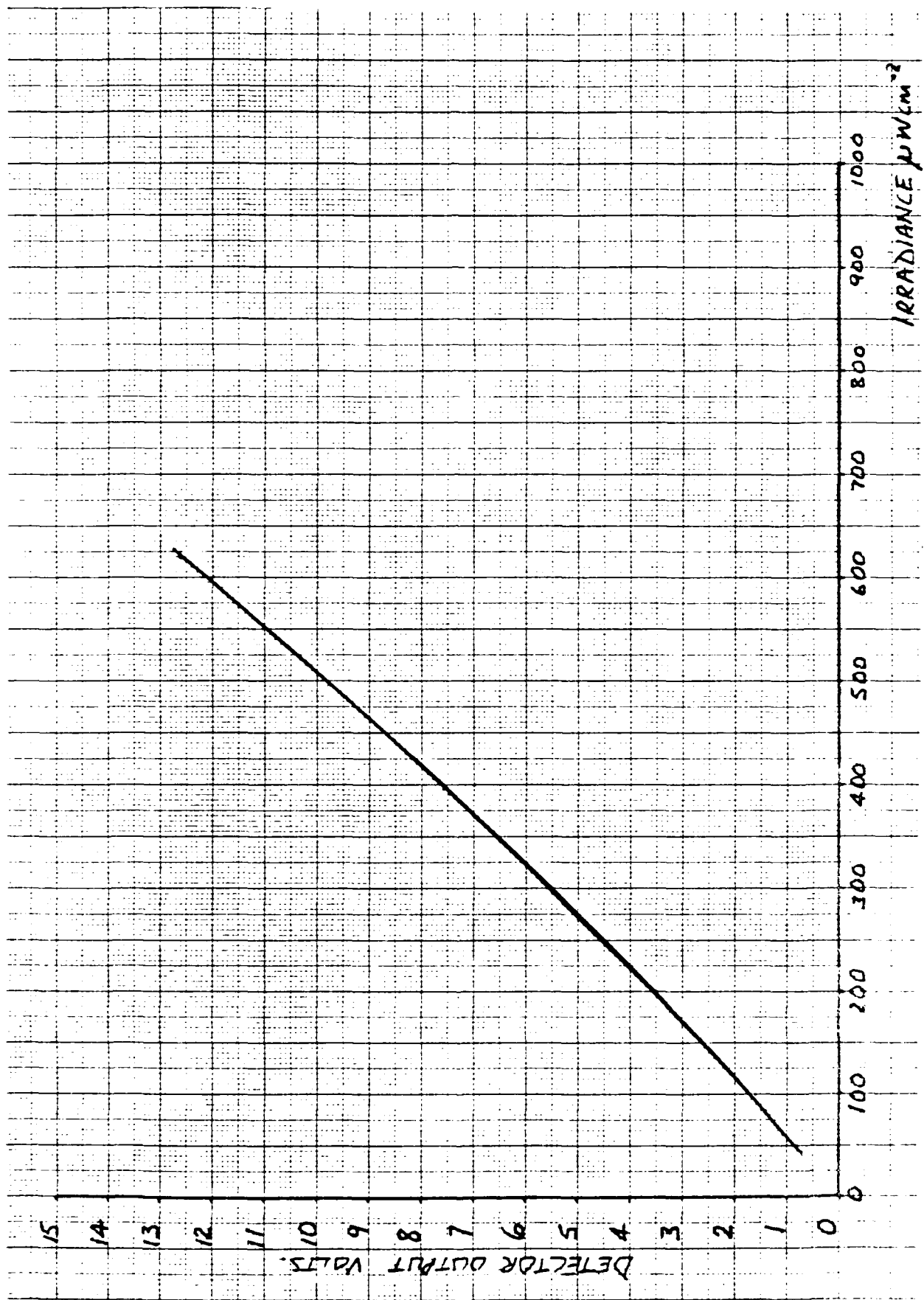
Figure A-4. RAP Pyroelectric Detector Calibration

105
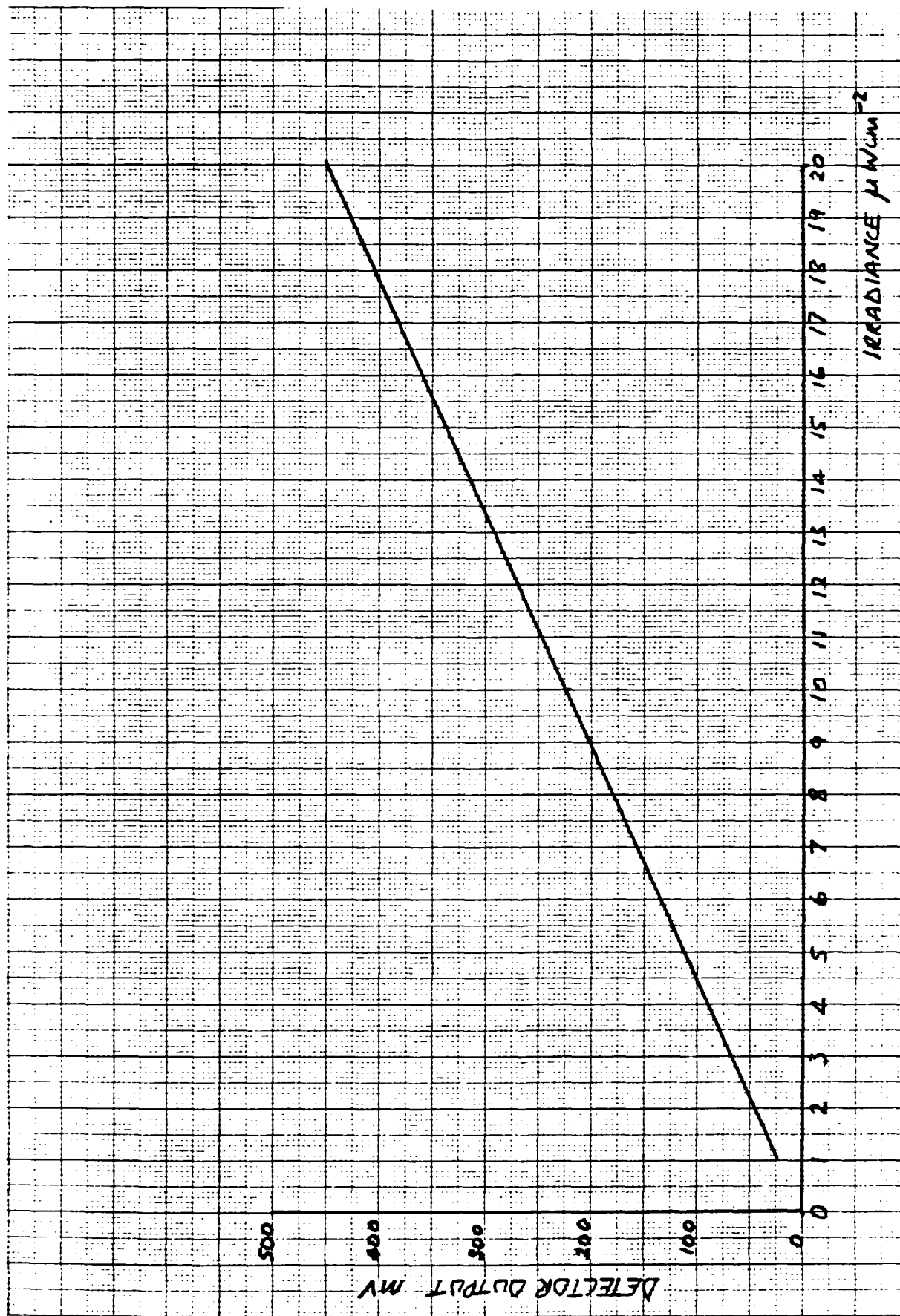
Figure A-5 RAP Pyroelectric Detector Calibration

106

APPENDIX B

Filter Transmission and Bandwidth Data
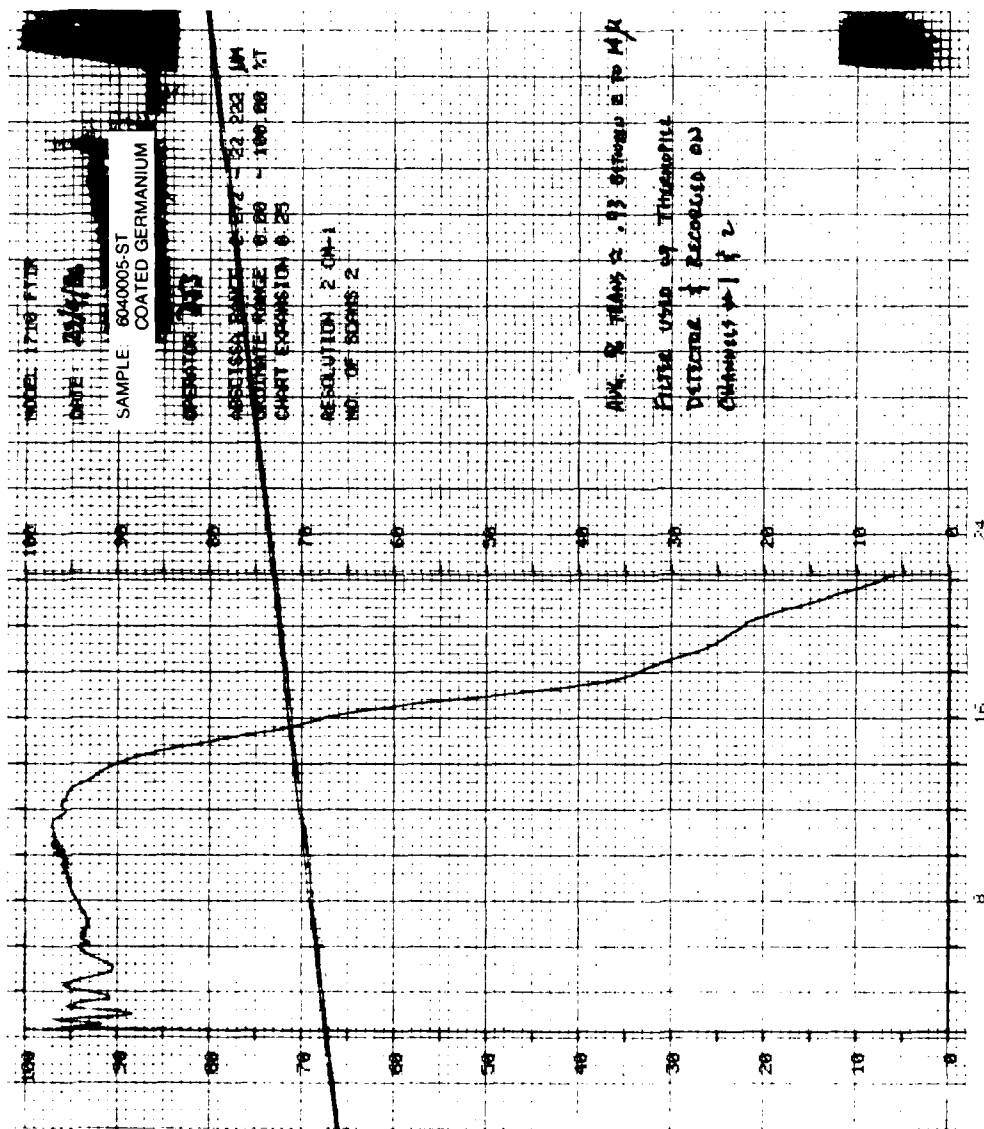
Figure B-1. Broad Band (Coated Ge) Filter Transmission

108
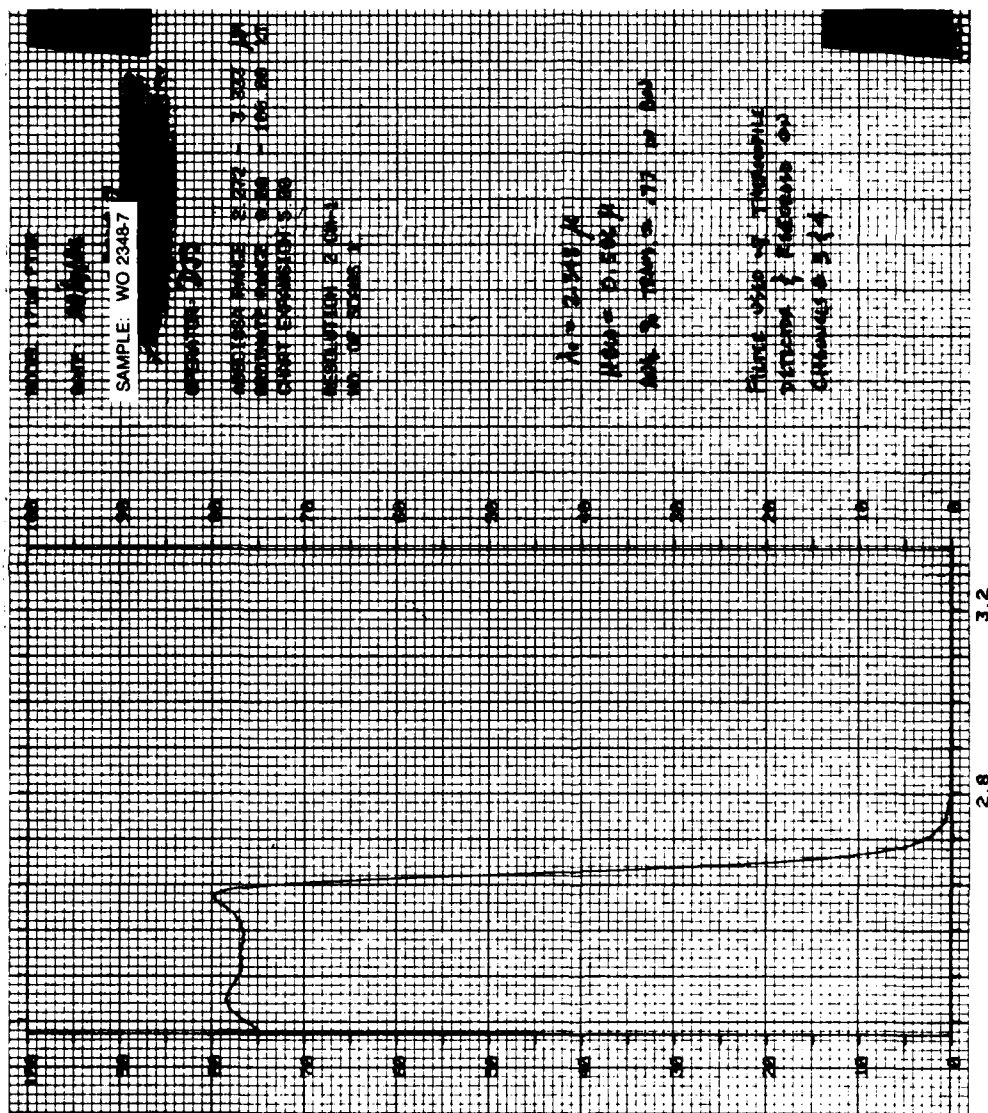
Figure B-2. Narrow Band Filter Transmission, Centered at 2.348 μm
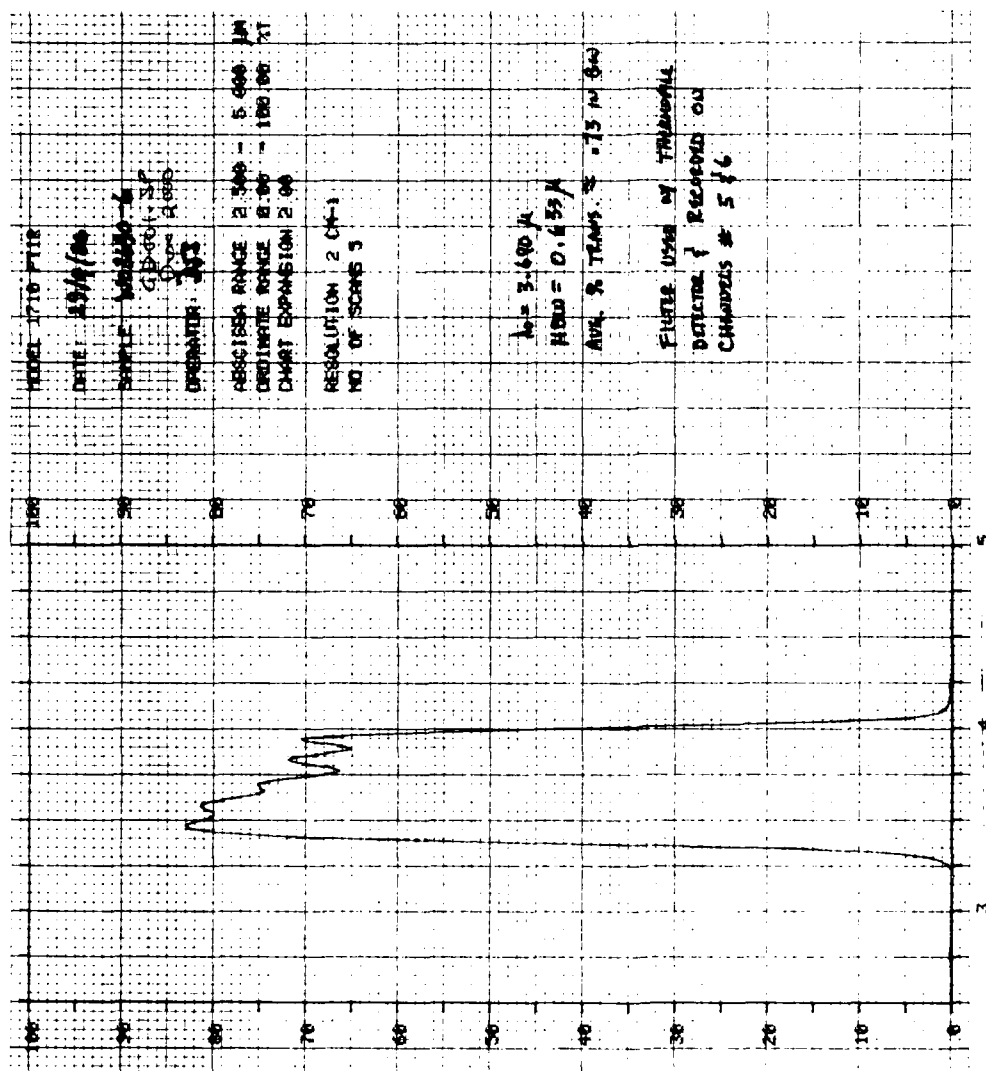
Figure B-3. Narrow Band Filter Transmission, Centered at 3.690 μm

Figure B-4. Broad Band Filter Transmission, Centered at 9.597 μm
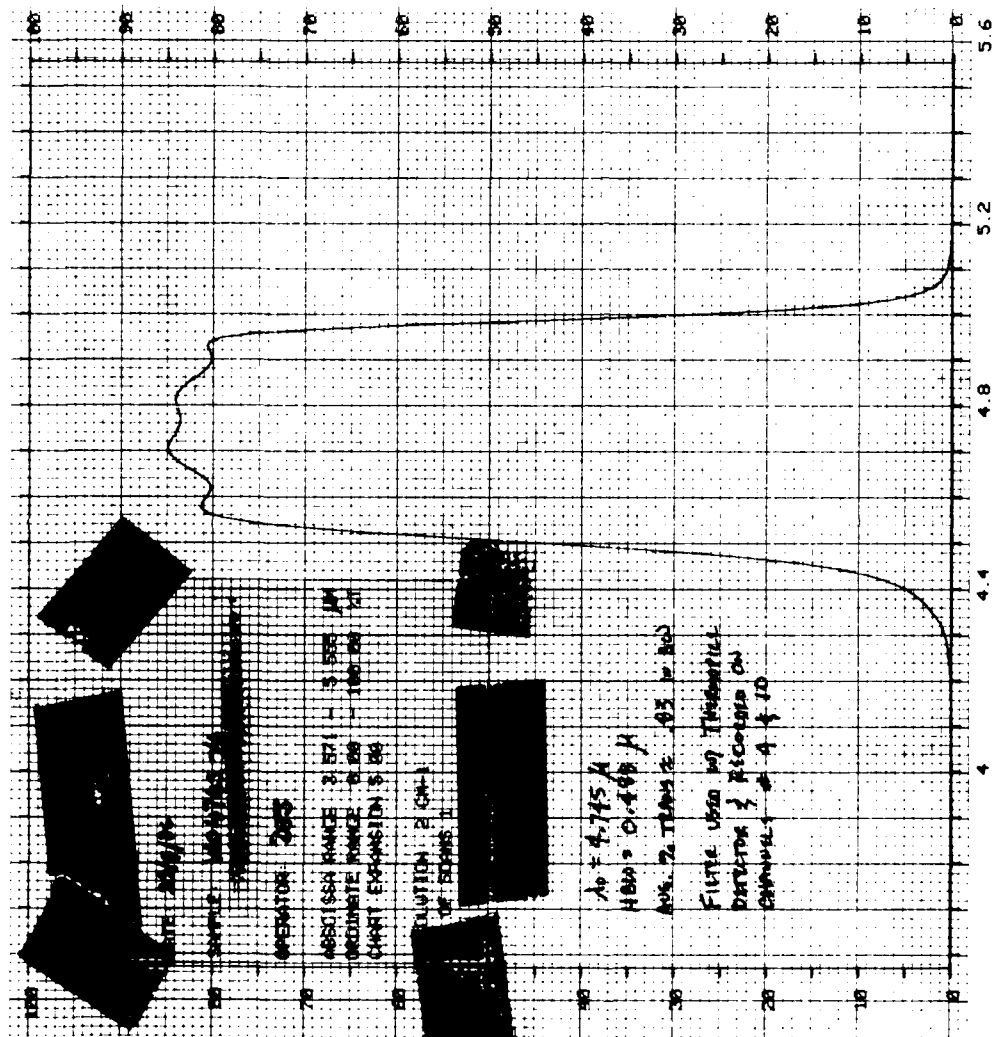
Figure B-5. Narrow Band Filter Transmission, Centered at 4.745 µm
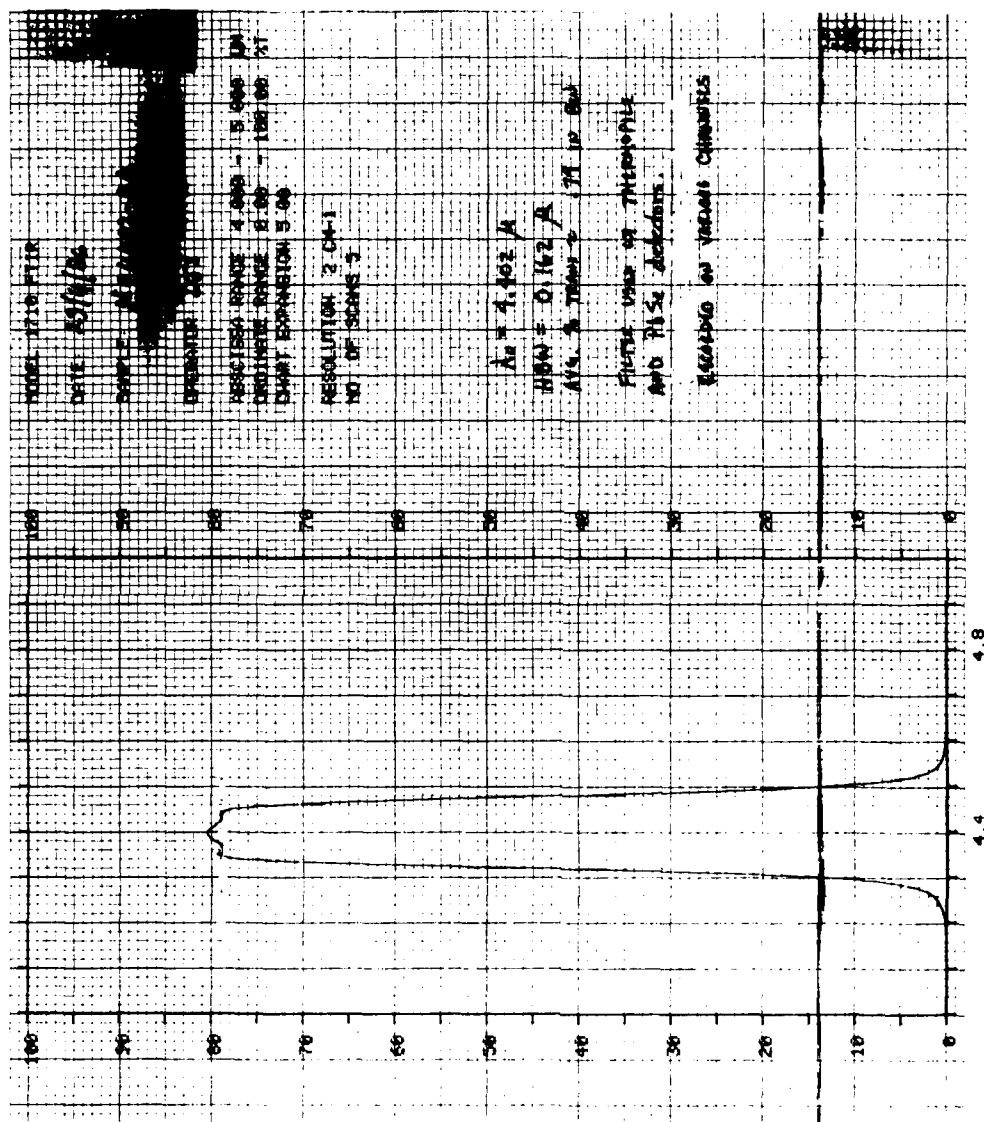
Figure B-6. Narrow Band Filter Transmission, Centered at 4.402 μm

113
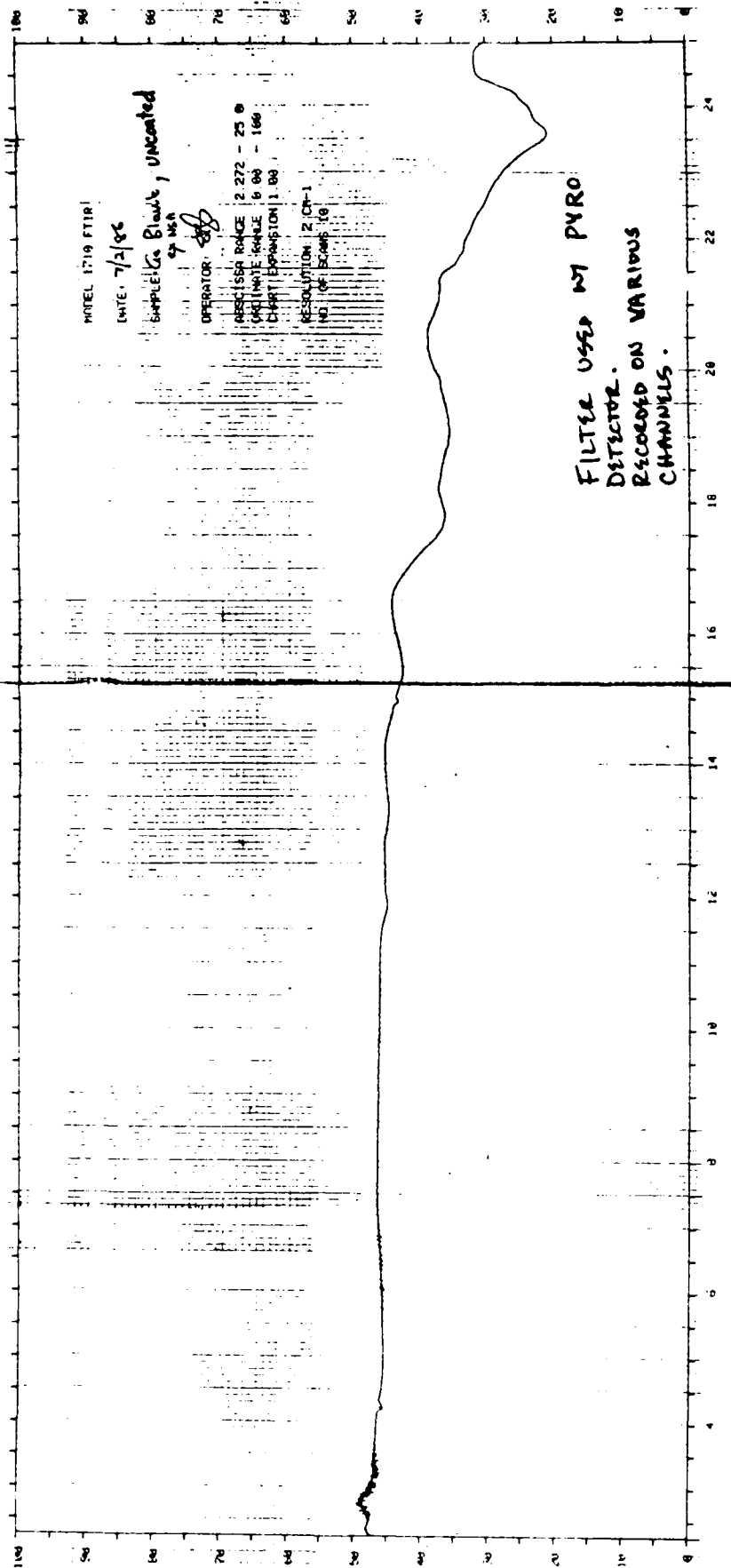
Figure B-7. Broad Band (Uncoated Ge) Filter Transmission

APPENDIX C

RAP Detector Output Voltage Records
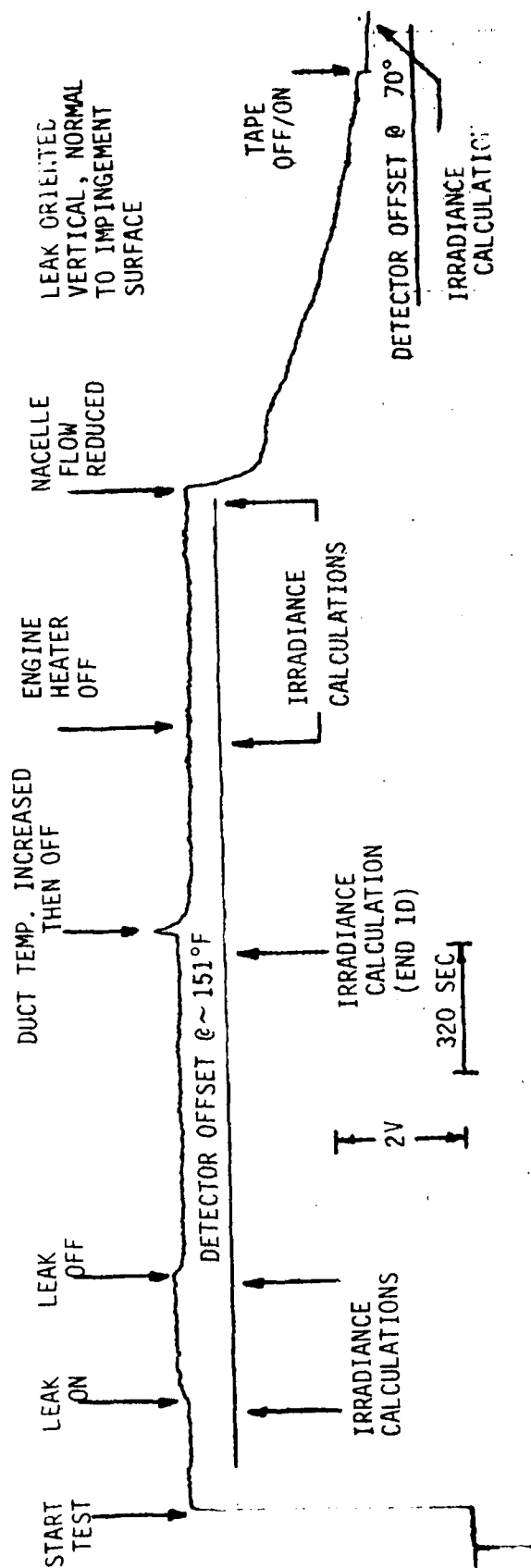
Figure C 1. Output of Channel 5 (3.690 ± .317 μm) for Tests 1D and 1E [start] (M=1.2)

116

LEAK ORIENTED VERTICAL,
NORMAL TO IMPINGEMENT SURFACE

TAPE OFF/ON

NACELLE
FLOW
REDUCED

ENGINE
HEATER
OFF

IRRADIANCE
CALCULATIONS

IRRADIANCE CALCULATION

DUCT TEMP. INCREASED,
THEN OFF

IRRADIANCE
CALCULATION (END 1D)

DETECTOR OFFSET @ 151°F

320 SEC

LEAK
OFF

LEAK
ON

IRRADIANCE
CALCULATIONS

2V
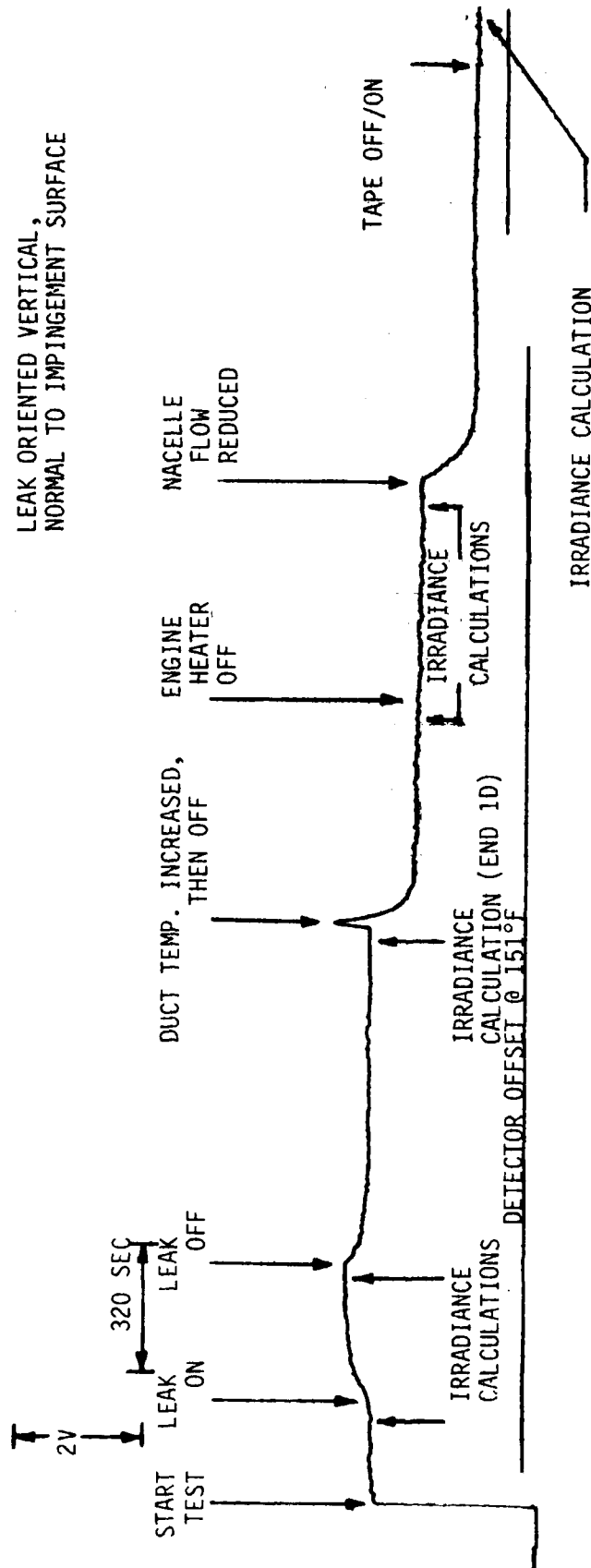
START
TEST

Figure C-2. Output of Channel 7 (9.597± 2.113 μm) for Tests 1D and 1E [start] (M=1.2)

117
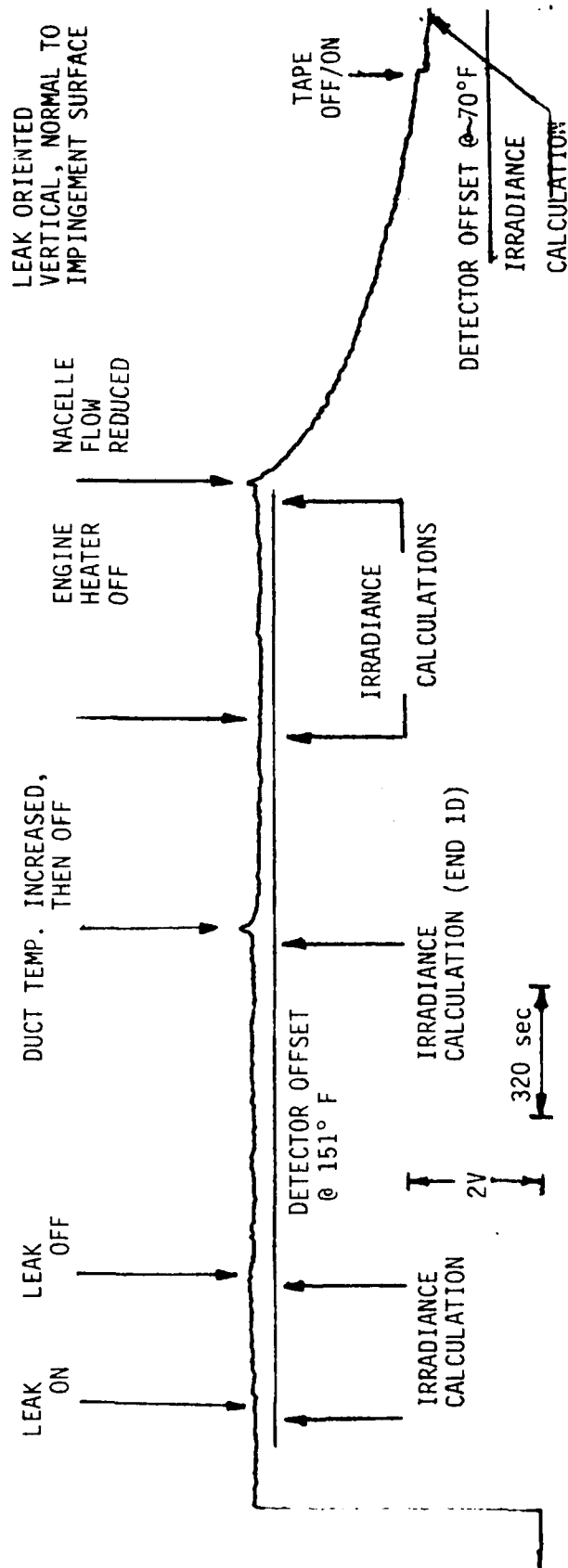
Figure C-3. Output of Channel 9 (4.745 ± .244 μm) for Tests 1D and 1E [start] (M=1.2)

118
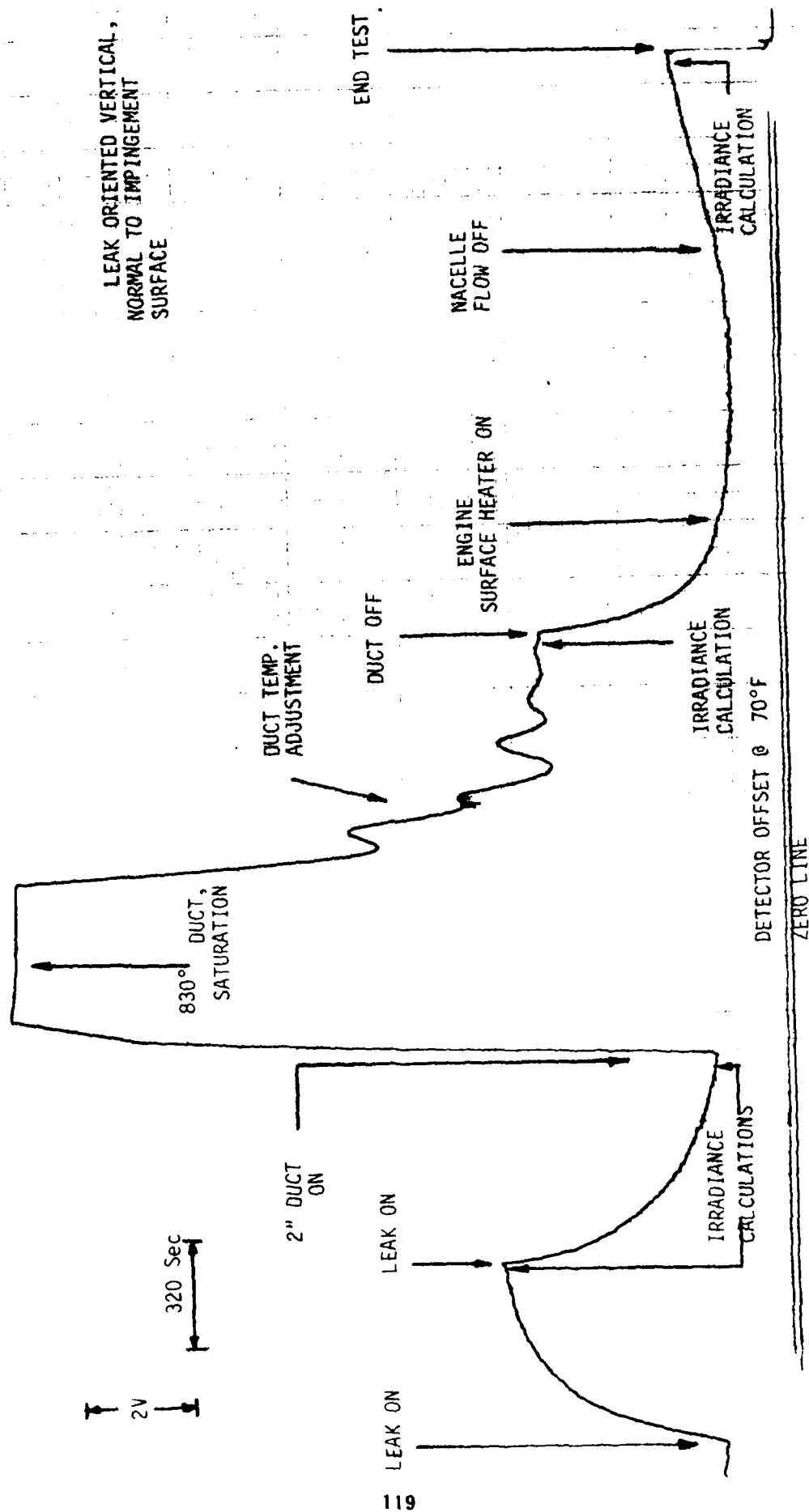
Figure C-4. Output of Channel 1 (Ge, 2-14μm) for Test 1E [cont] (M=1.2)

119
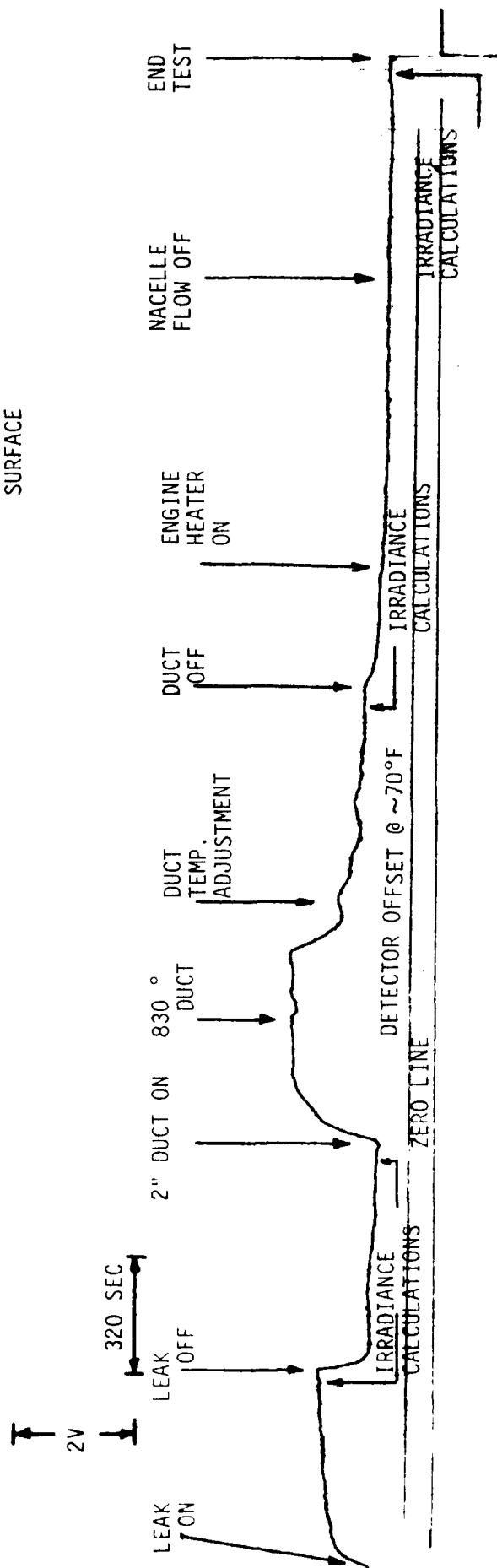
Figure C-5. Output of Channel 5 (3.690± .317 μm) for Test 1E[cont] (M=1.2)

120
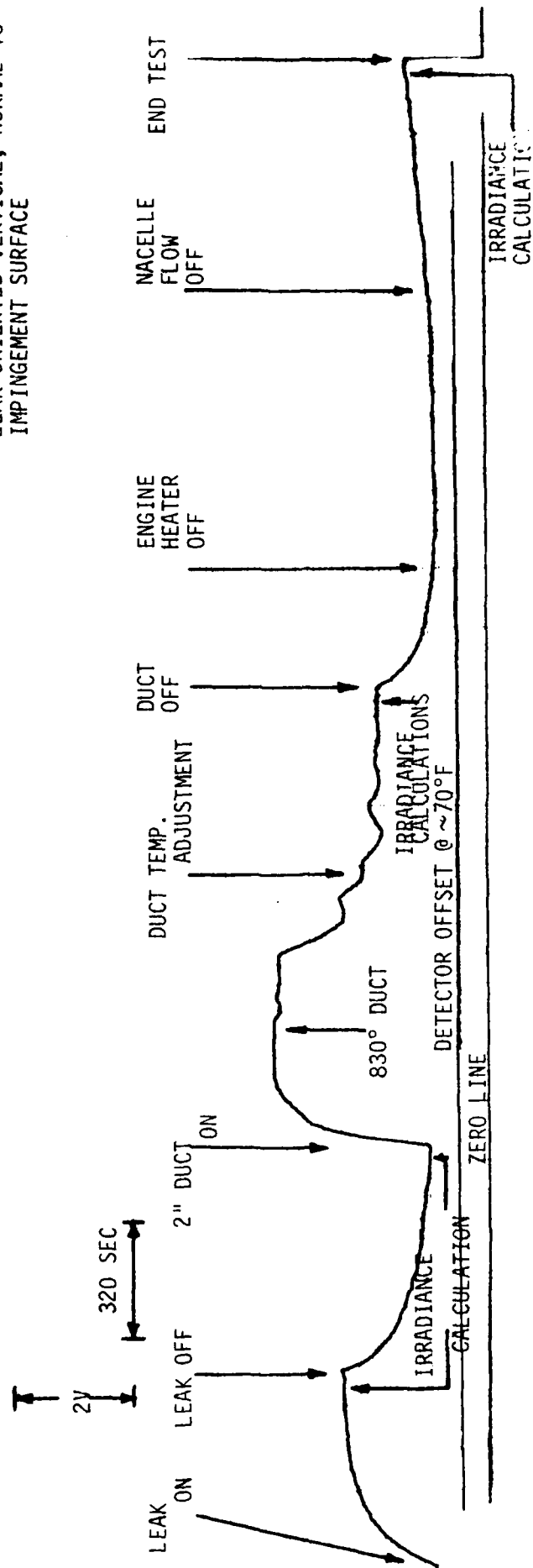
Figure C-6. Output of Channel 7 (9.597 ± 2.113 μm) for Test 1E [cont] (M=1.2)

121
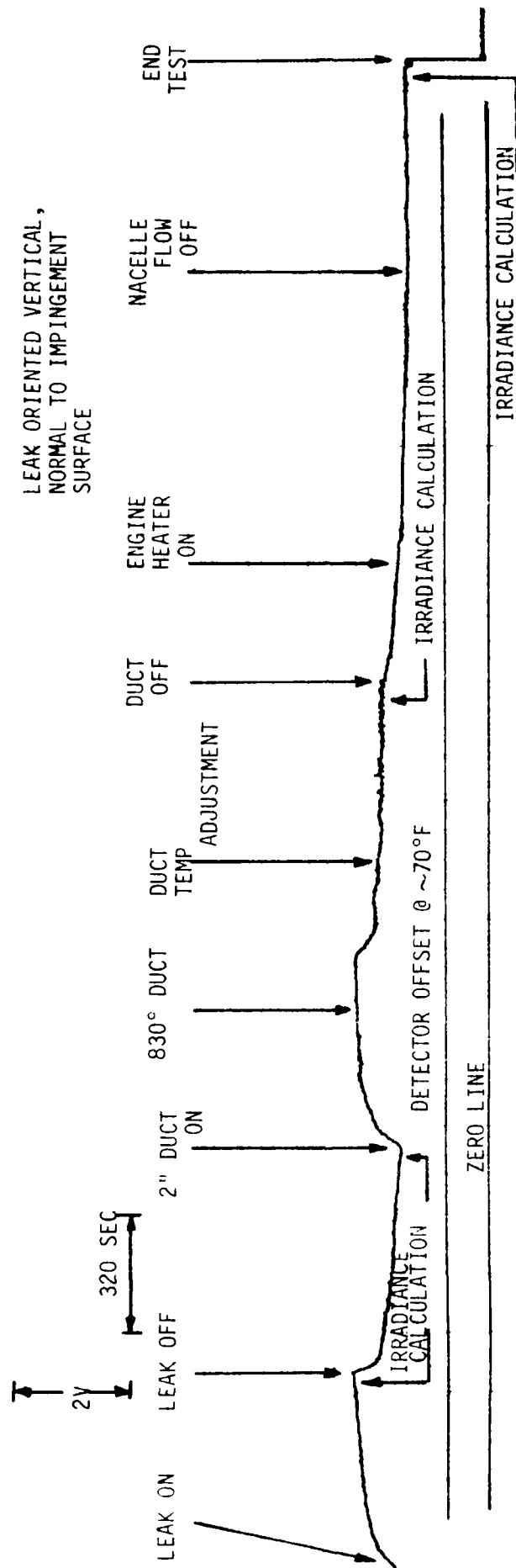
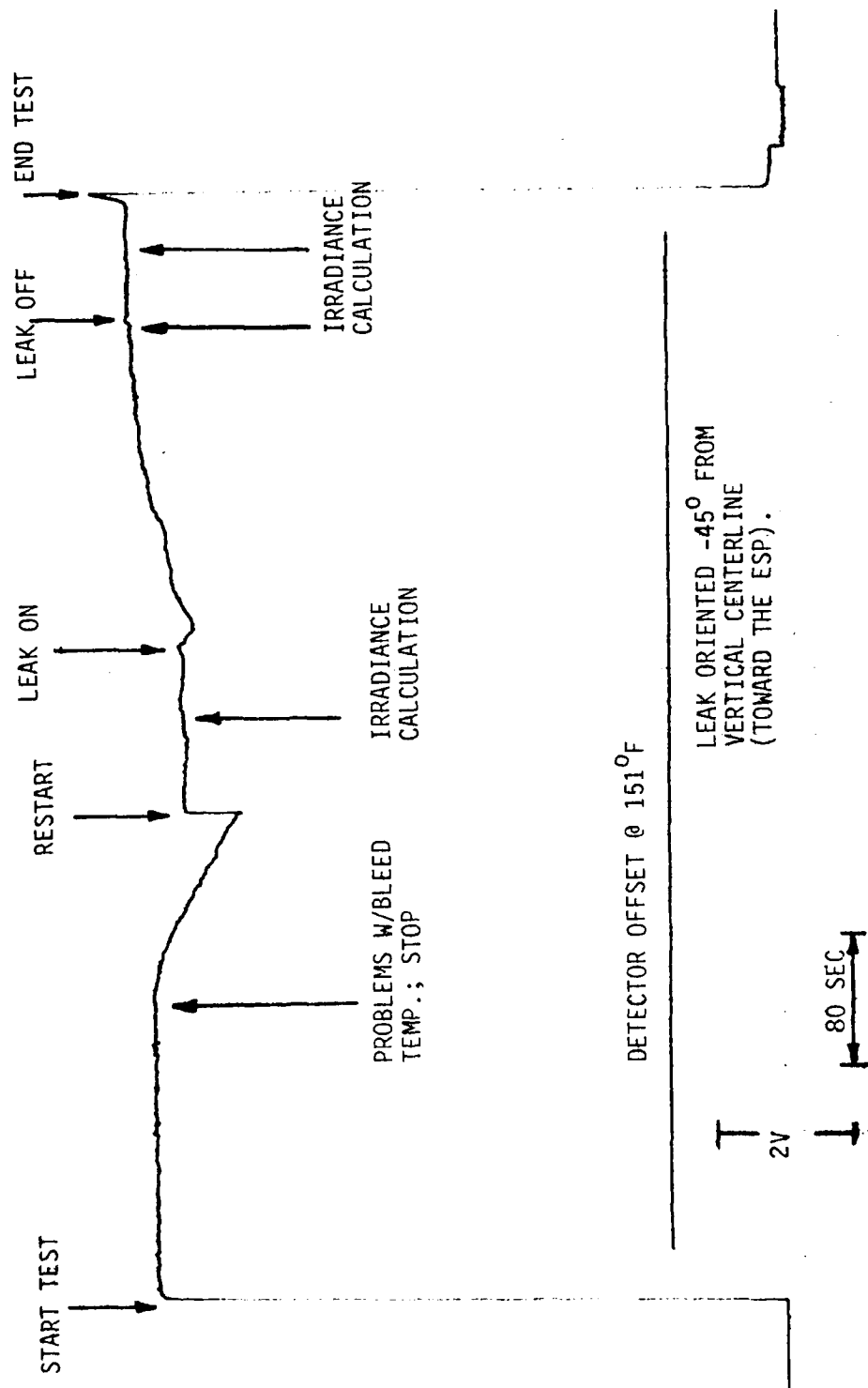Figure C-7. Output of Channel 9 (4.745 $\pm$ .244 μm) for Test 1E [cont] (M=1.2)

122
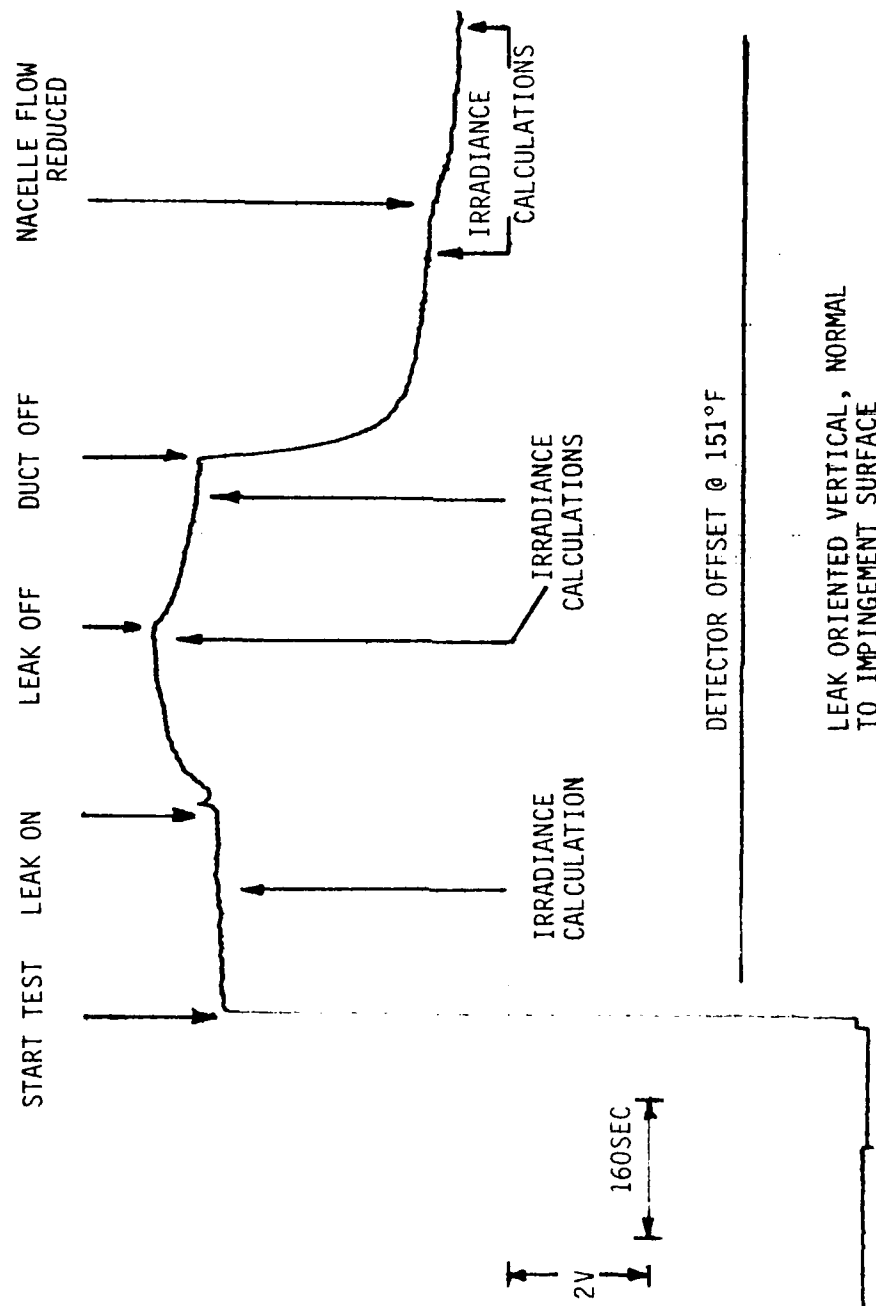
Figure C-8. Output of Channel 1 (Ge, 2-14 μm) for Test 1 F (M=1.2)

123
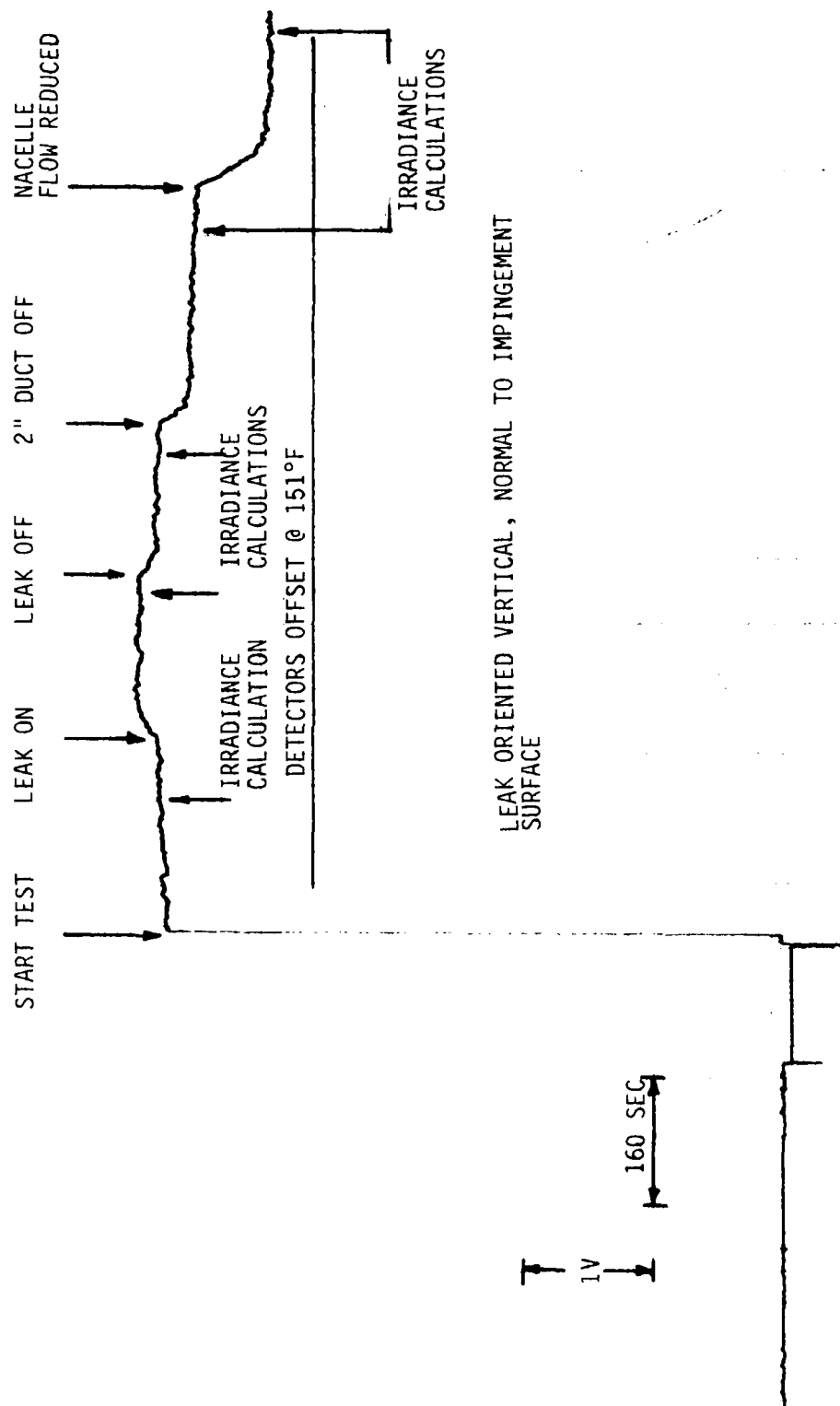
Figure C-9. Output of Channel 5 (3.690± .317 μm) for Test 1F (M=1.2)
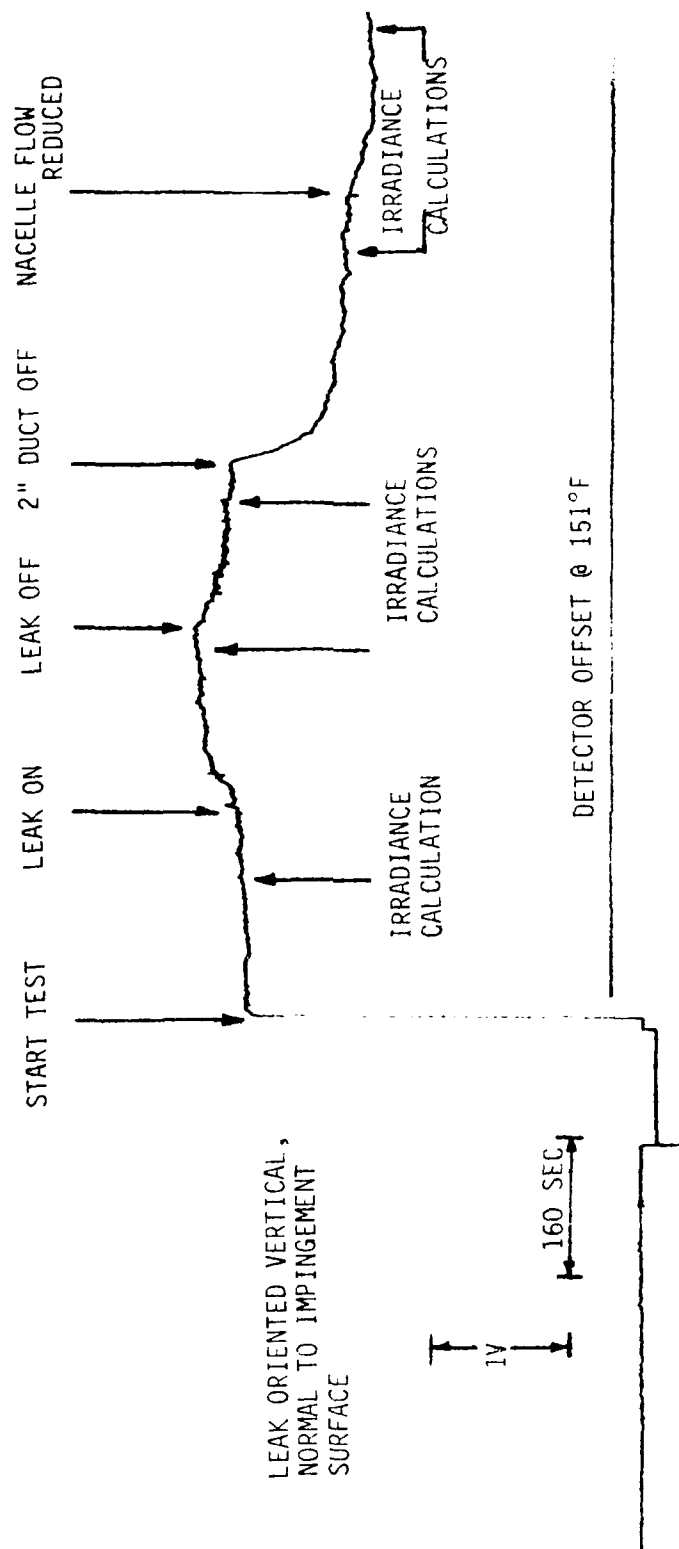
Figure C-10. Output of Channel 7 (9.597 ± 2.113 μm) for Test 1F (M=1.2)
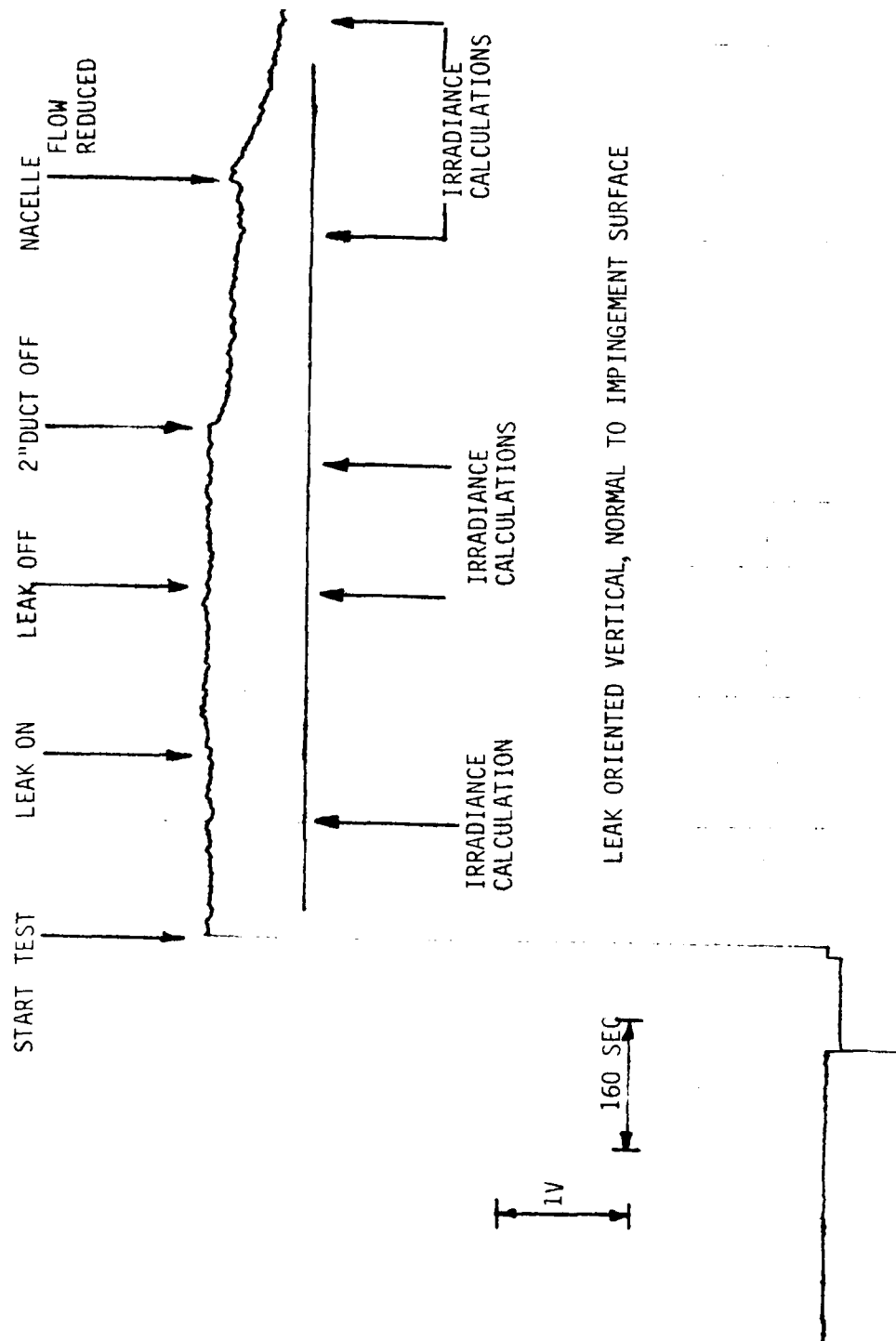
Figure C-11. Output of Channel 9 (4.745± .244 μm) for Test 1F (M=1.2)
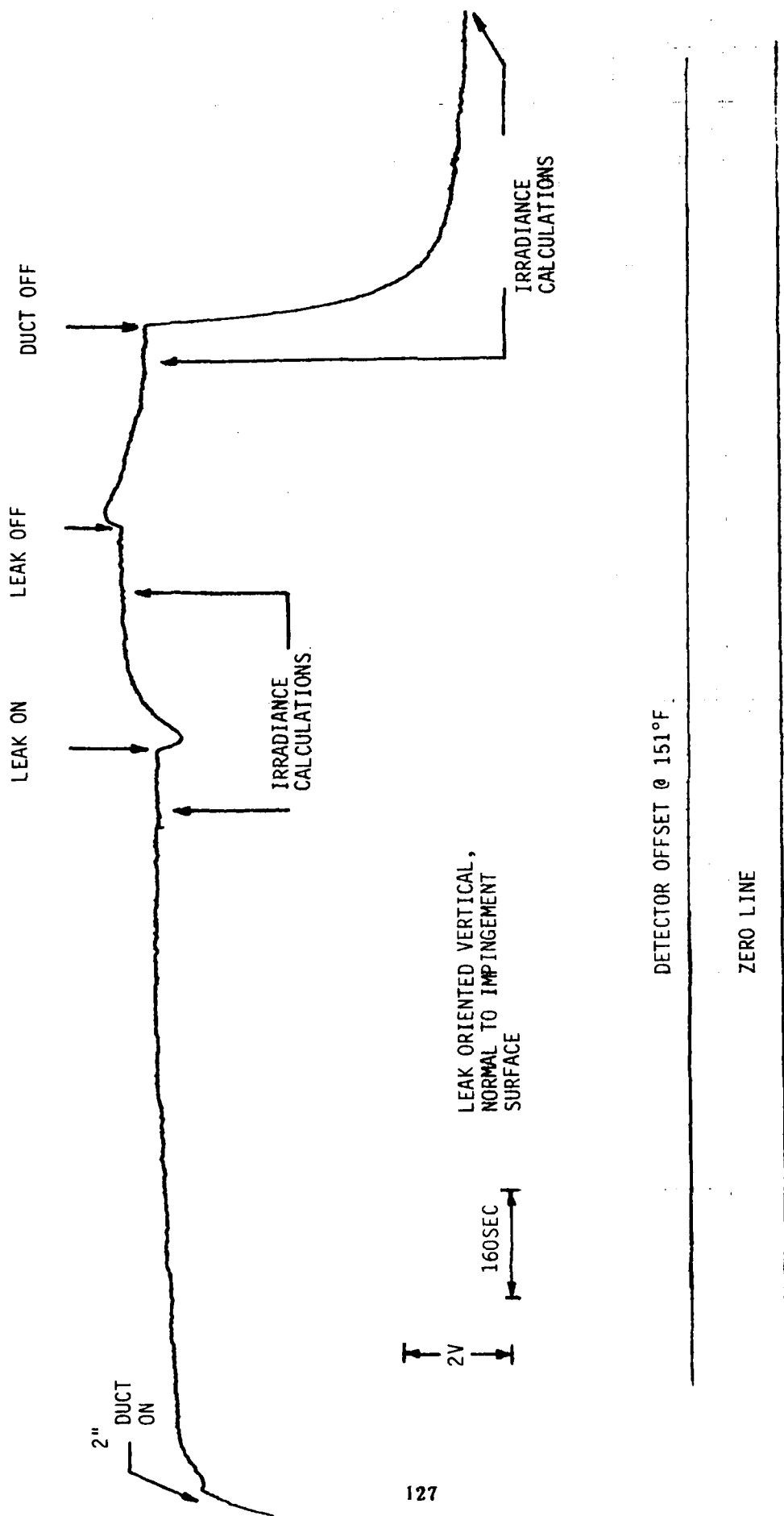
Figure C-12. Output of Channel 1 (Ge, 2-14 μm) for Test 1C (M=1.2)
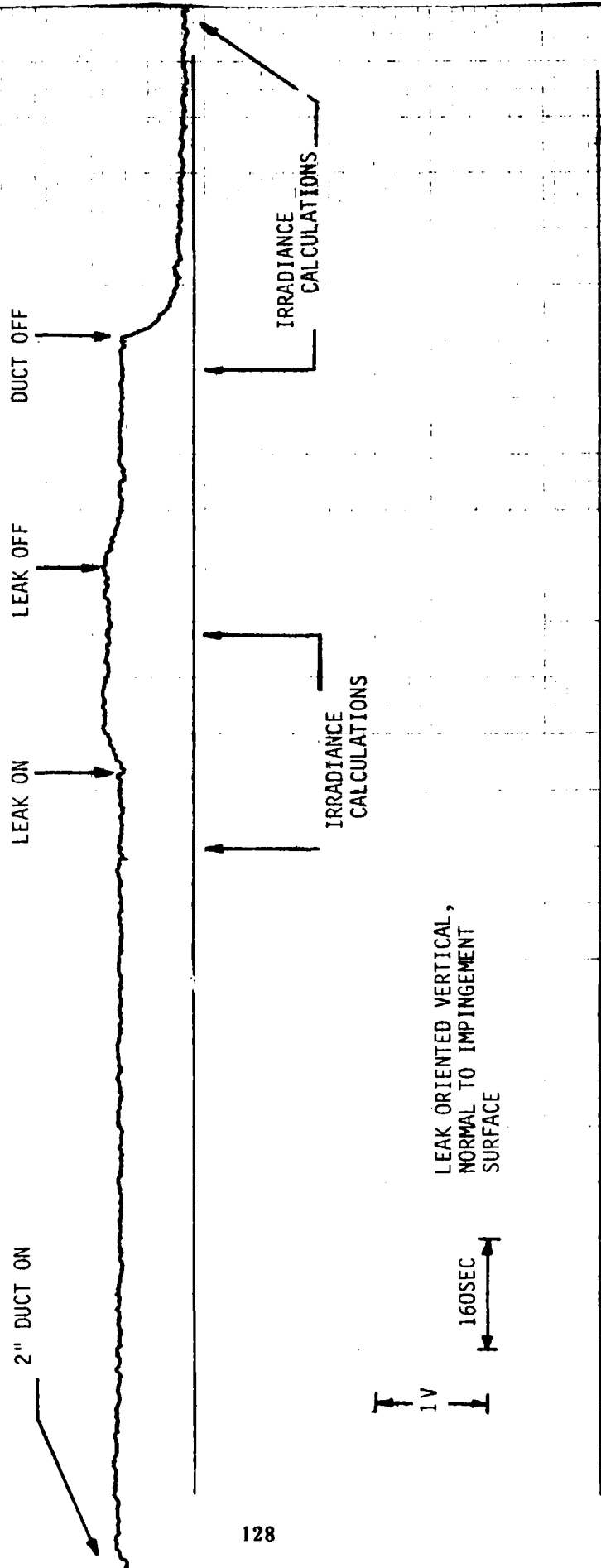
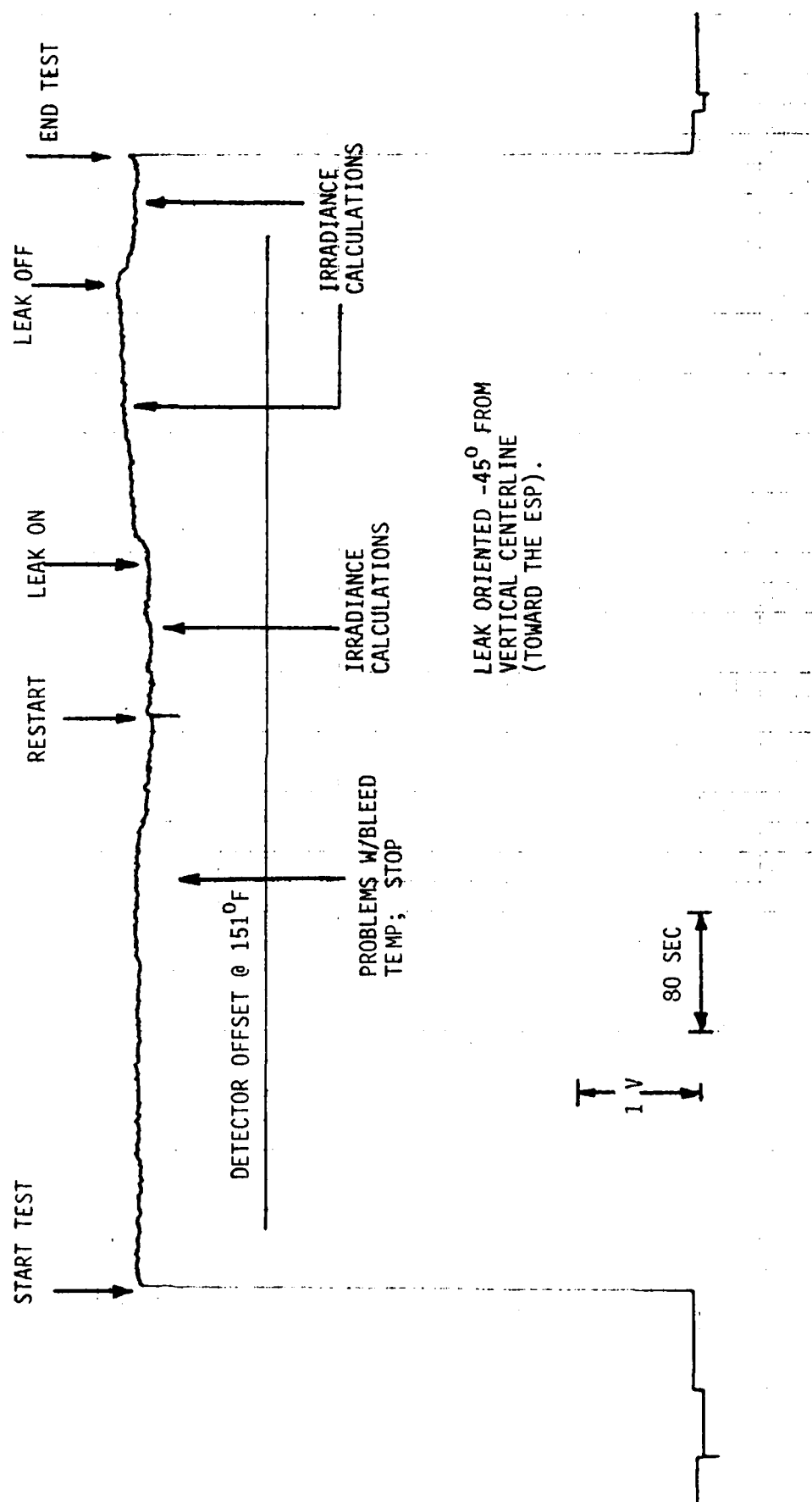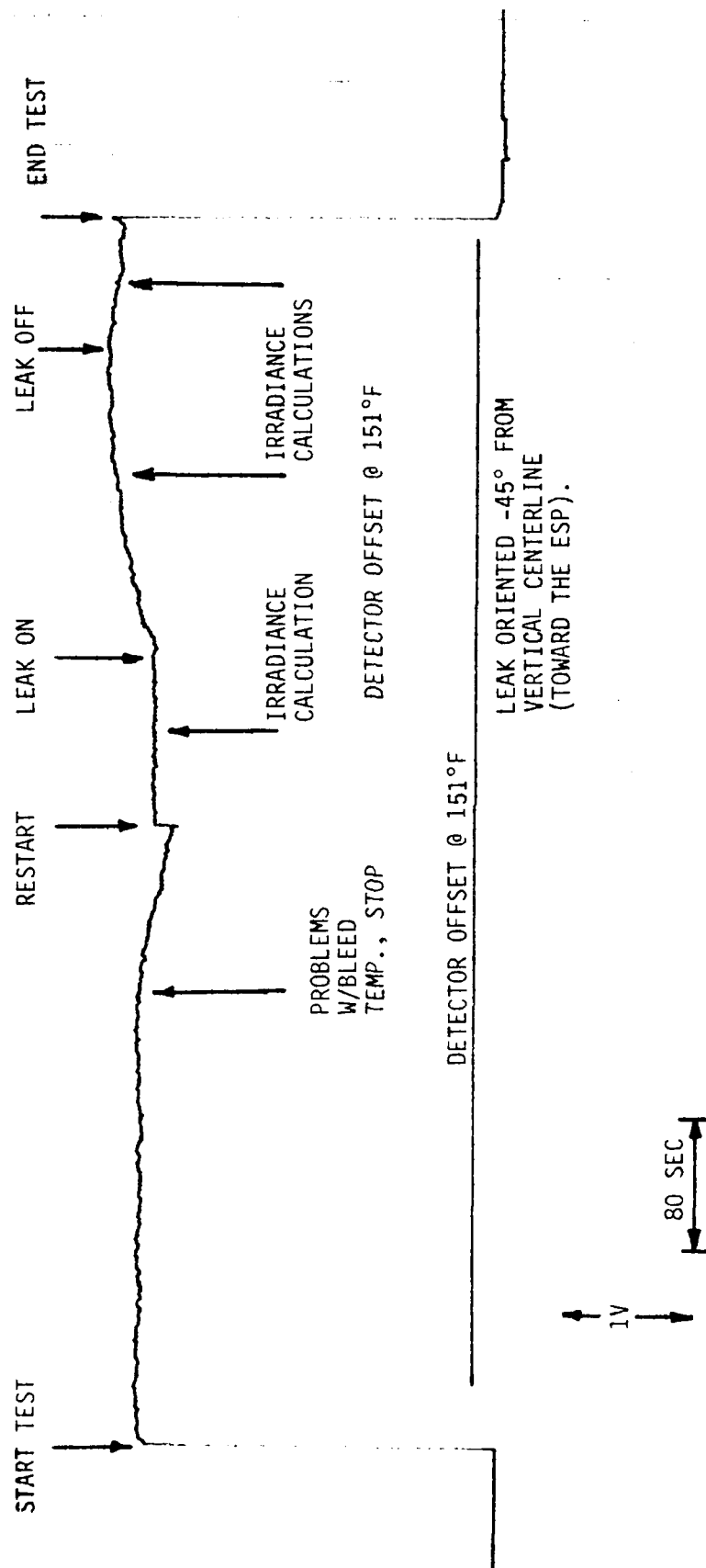Figure C-13. Output of Channel 5 (3.690± .317 μm) for Test 1G (M=1.2)

2" DUCT ON

LEAK ON

LEAK OFF

DUCT OFF

IRRADIANCE CALCULATIONS

IRRADIANCE CALCULATIONS

LEAK ORIENTED VERTICAL, NORMAL TO IMPINGEMENT SURFACE

DETECTOR OFFSET @ 151°F

160SEC

1V

ZERO LINE

129
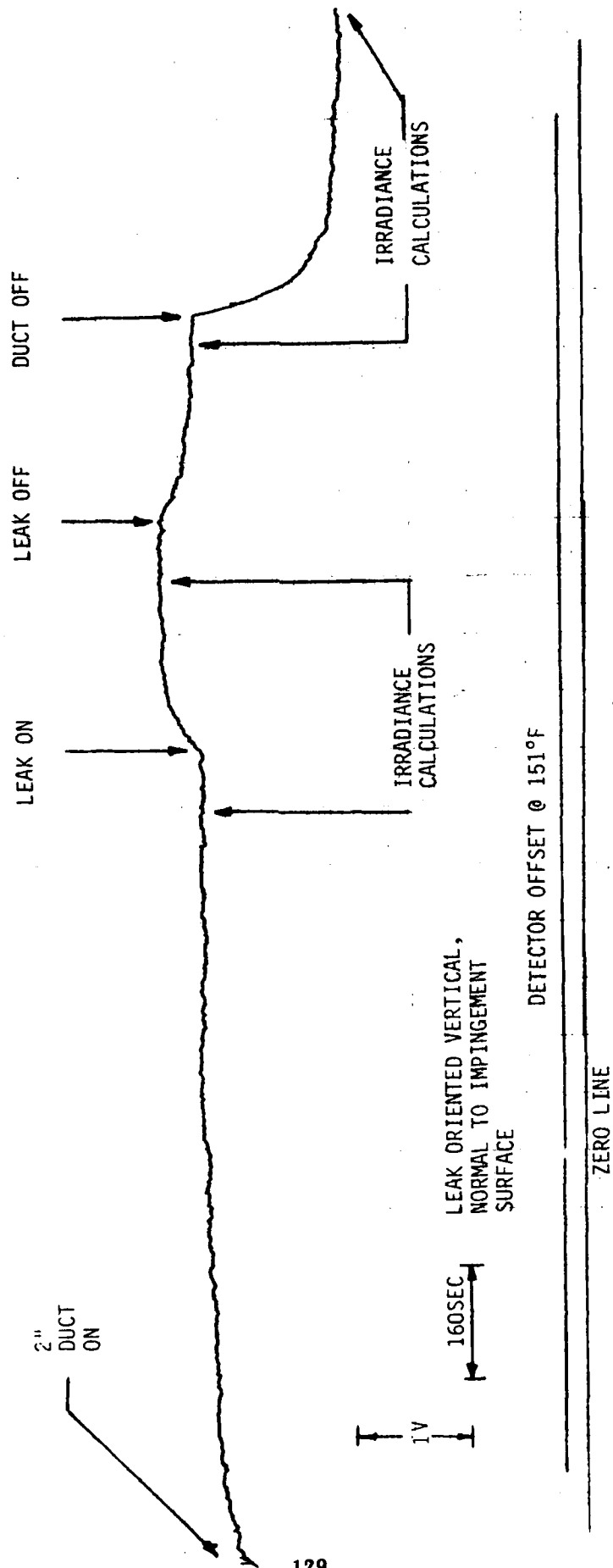
Figure C-14. Output of Channel 7 (9.597± 2.113 μm) for Test 1 G (M=1.2)
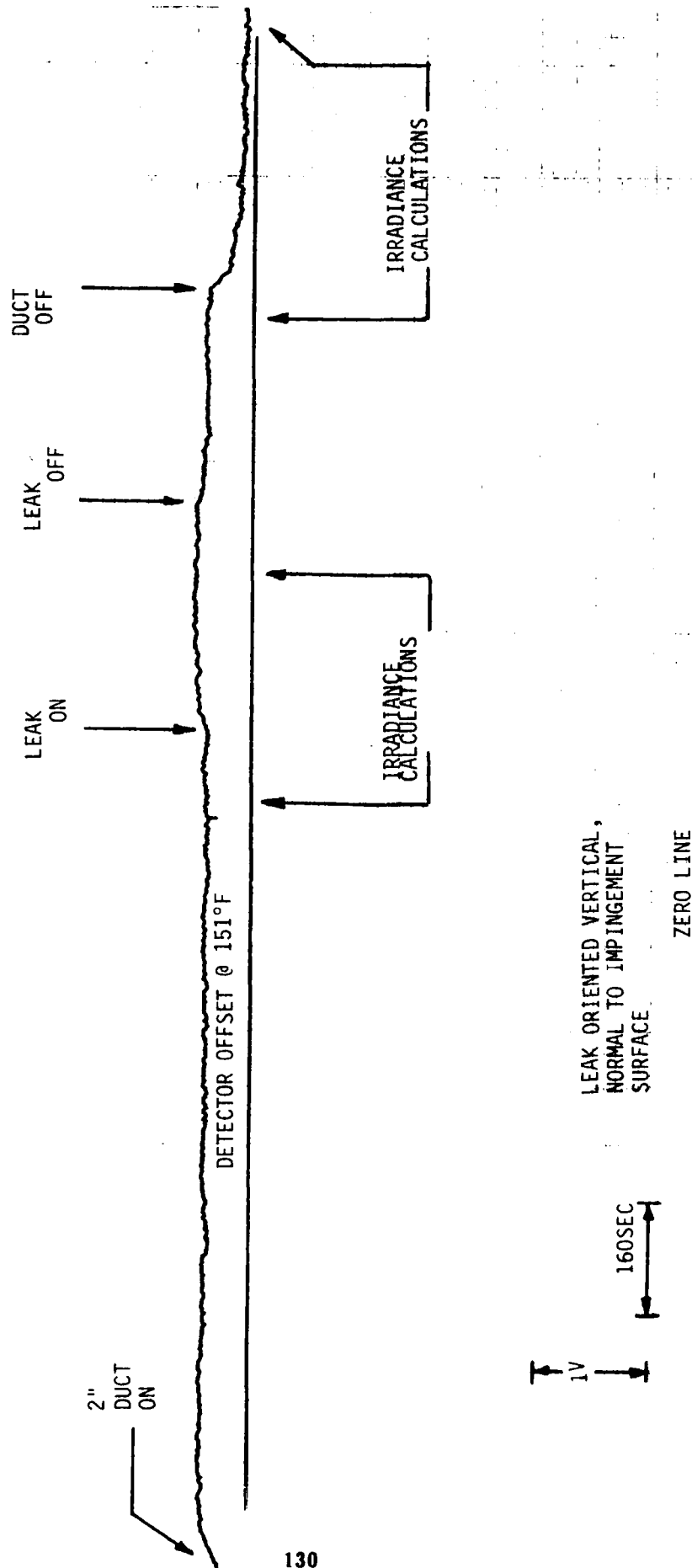
Figure C-15. Output of Channel 9 (4.745 ± .244 μm) for Test 1G (M=1.2)

130
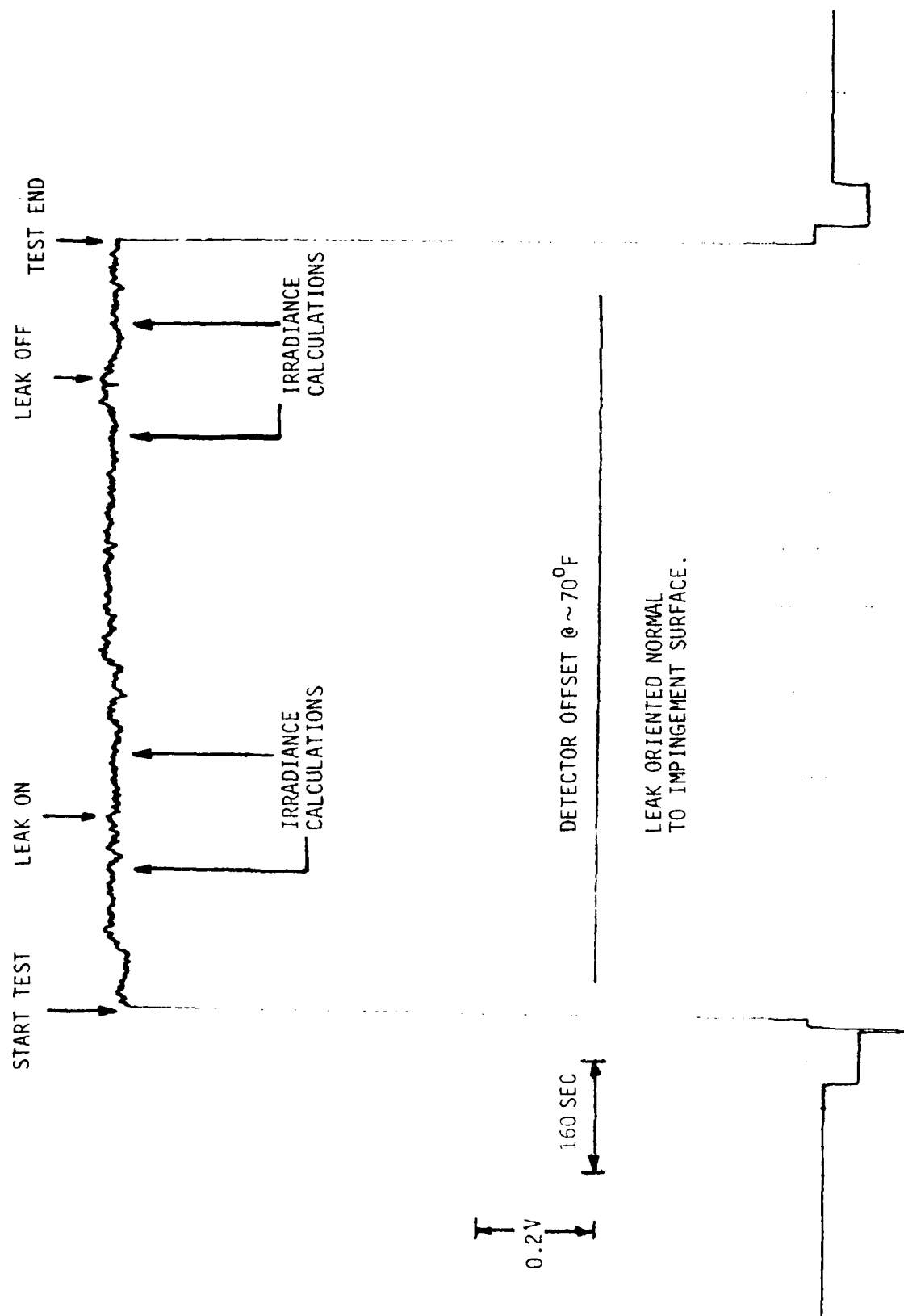
Figure C-16. Output of Channel 5 (3.690± .317 μm) for Test 2 (M=0.75)

131
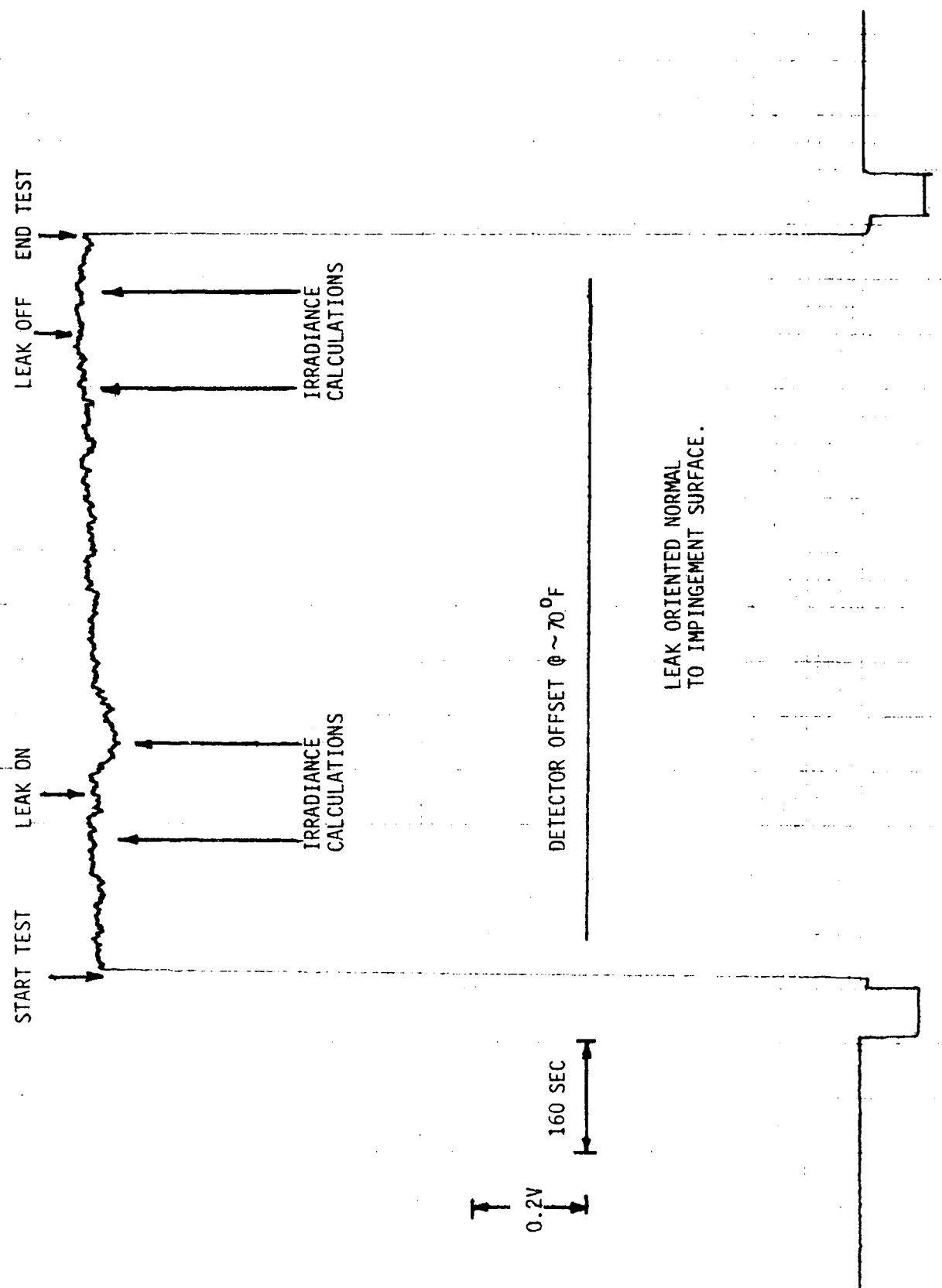
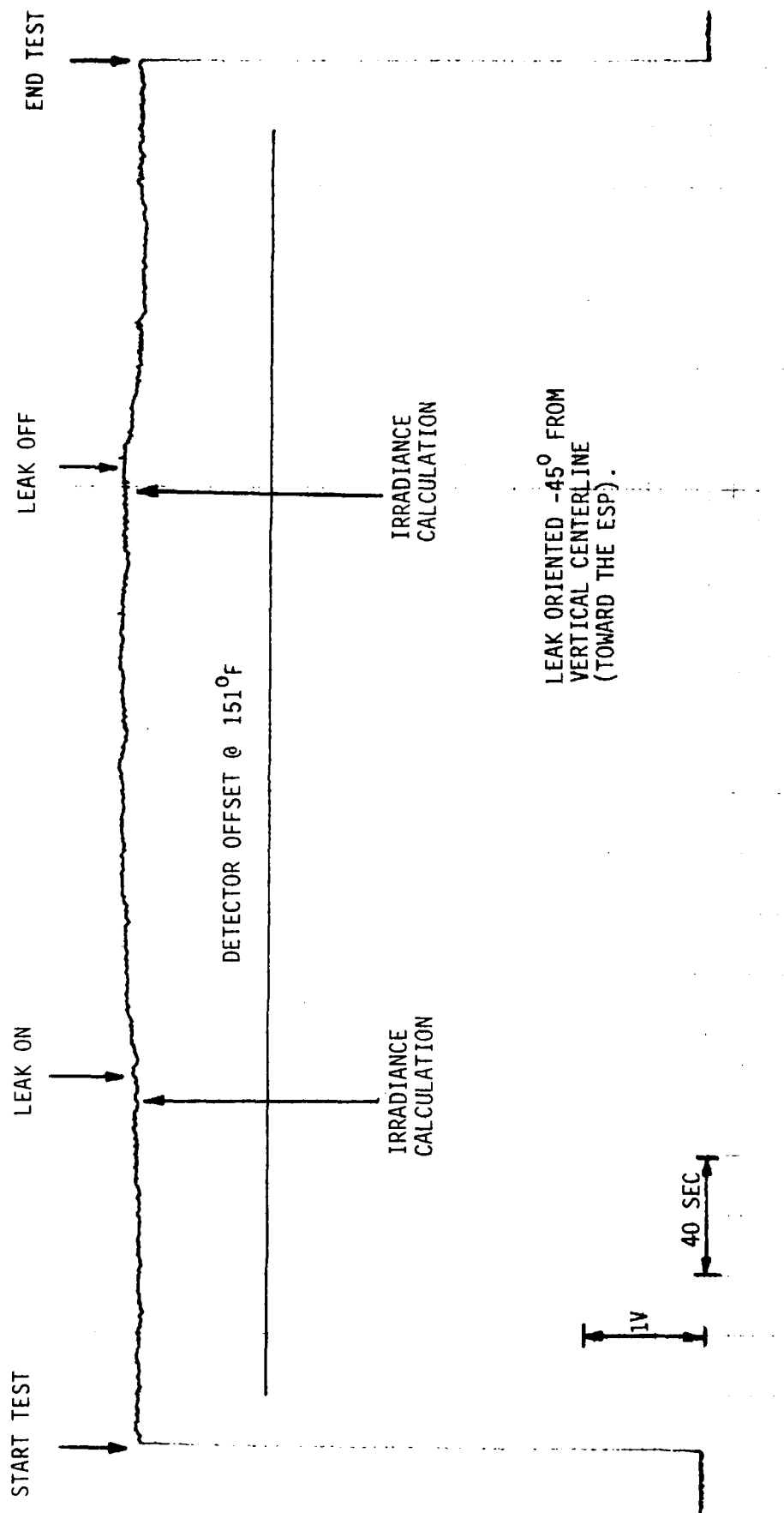Figure C-17. Output of Channel 7 (9.597± 2.113 μm) for Test 2 (M=0.75)
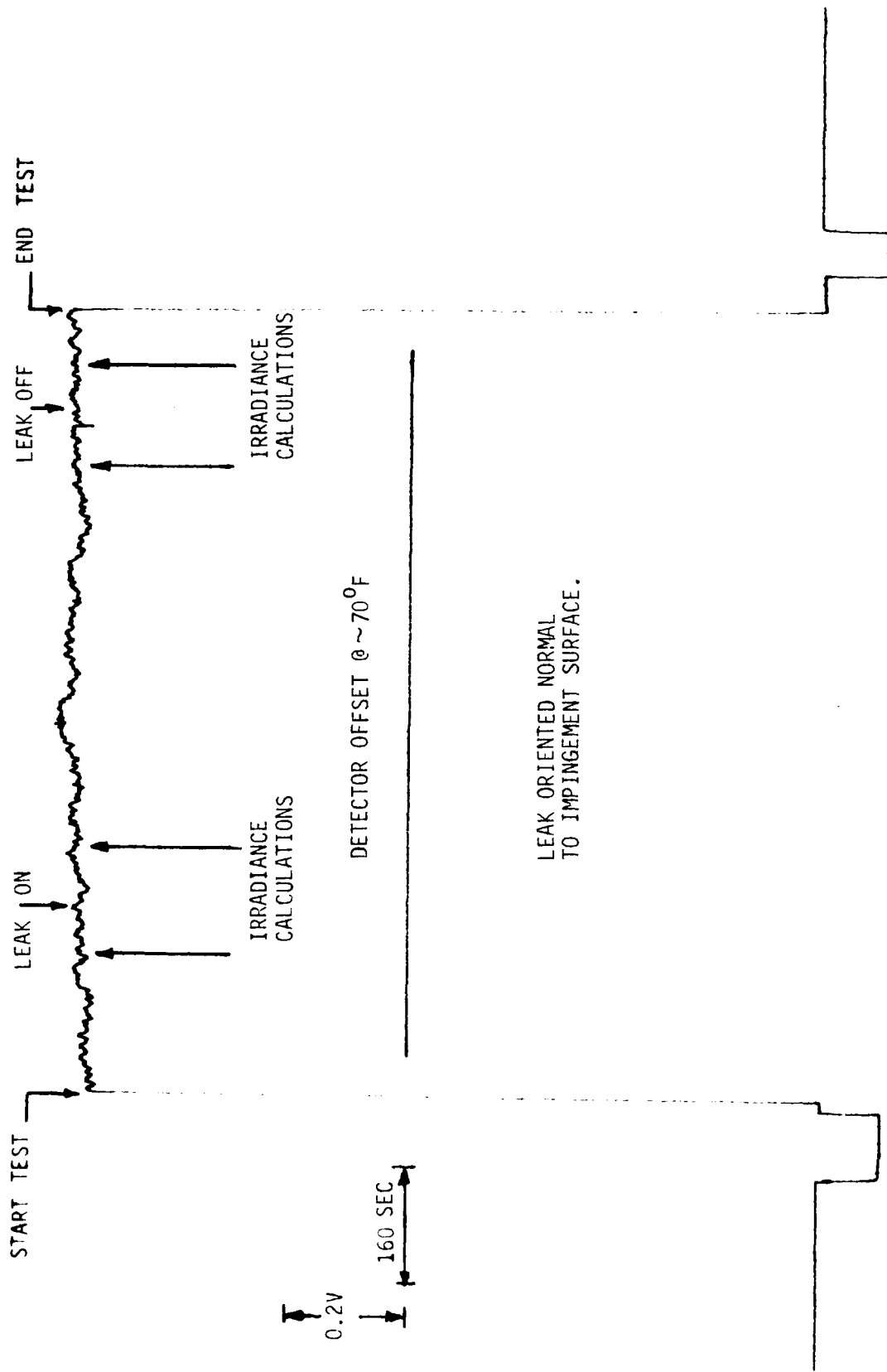
Figure C-18. Output of Channel 9 (4.745± .244 μm) for Test 2 (M=0.75)
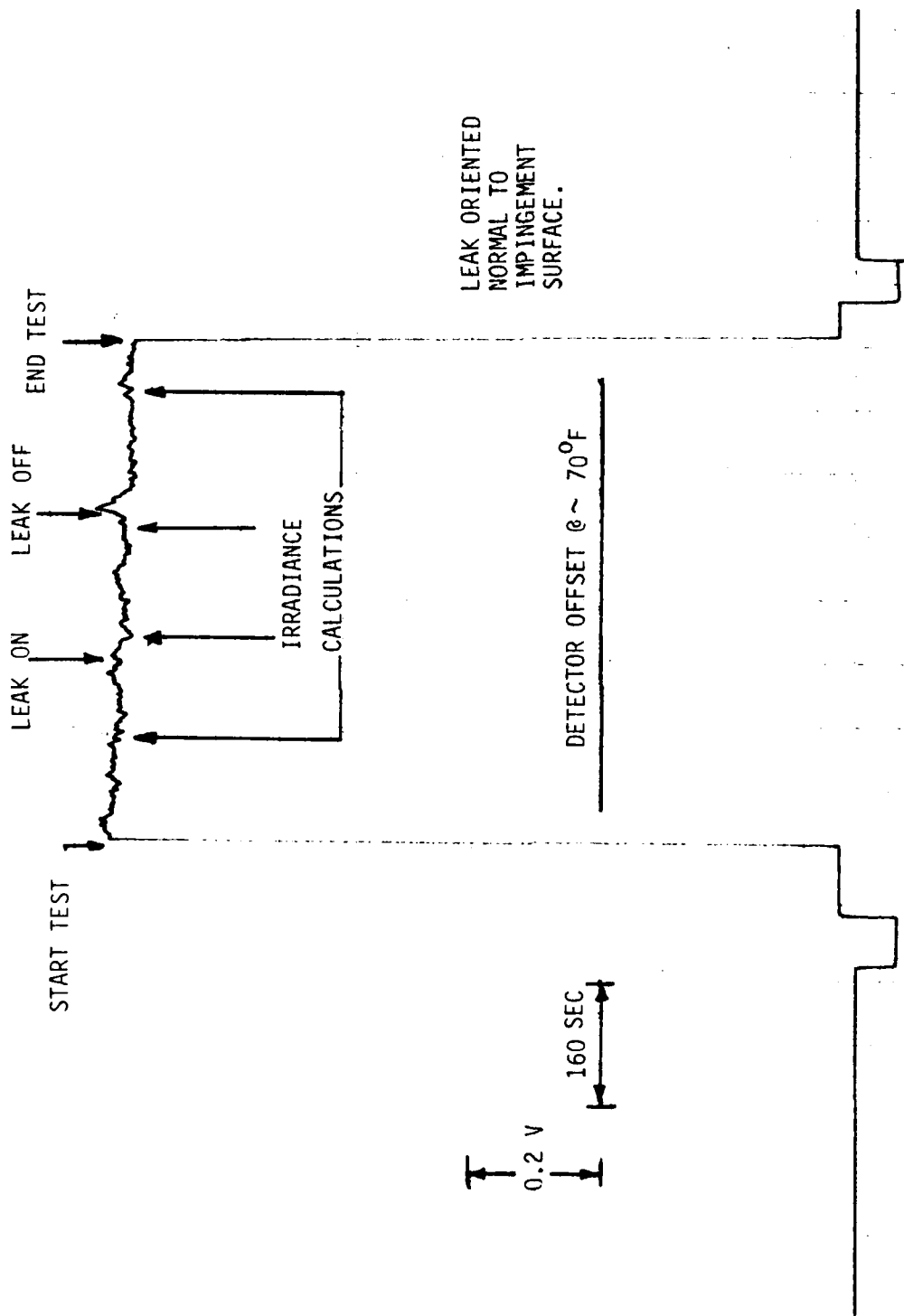
Figure C-19. Output of Channel 5 (3.690 ± .317 μm) for Test 3 (M=0.0)

START TEST

END TEST

LEAK
ON

LEAK
OFF

IRRADIANCE
CALCULATION

LEAK ORIENTED
NORMAL TO
IMPINGEMENT
SURFACE.

DETECTOR OFFSET @ ~ 70°F

0.2 V

160 SEC
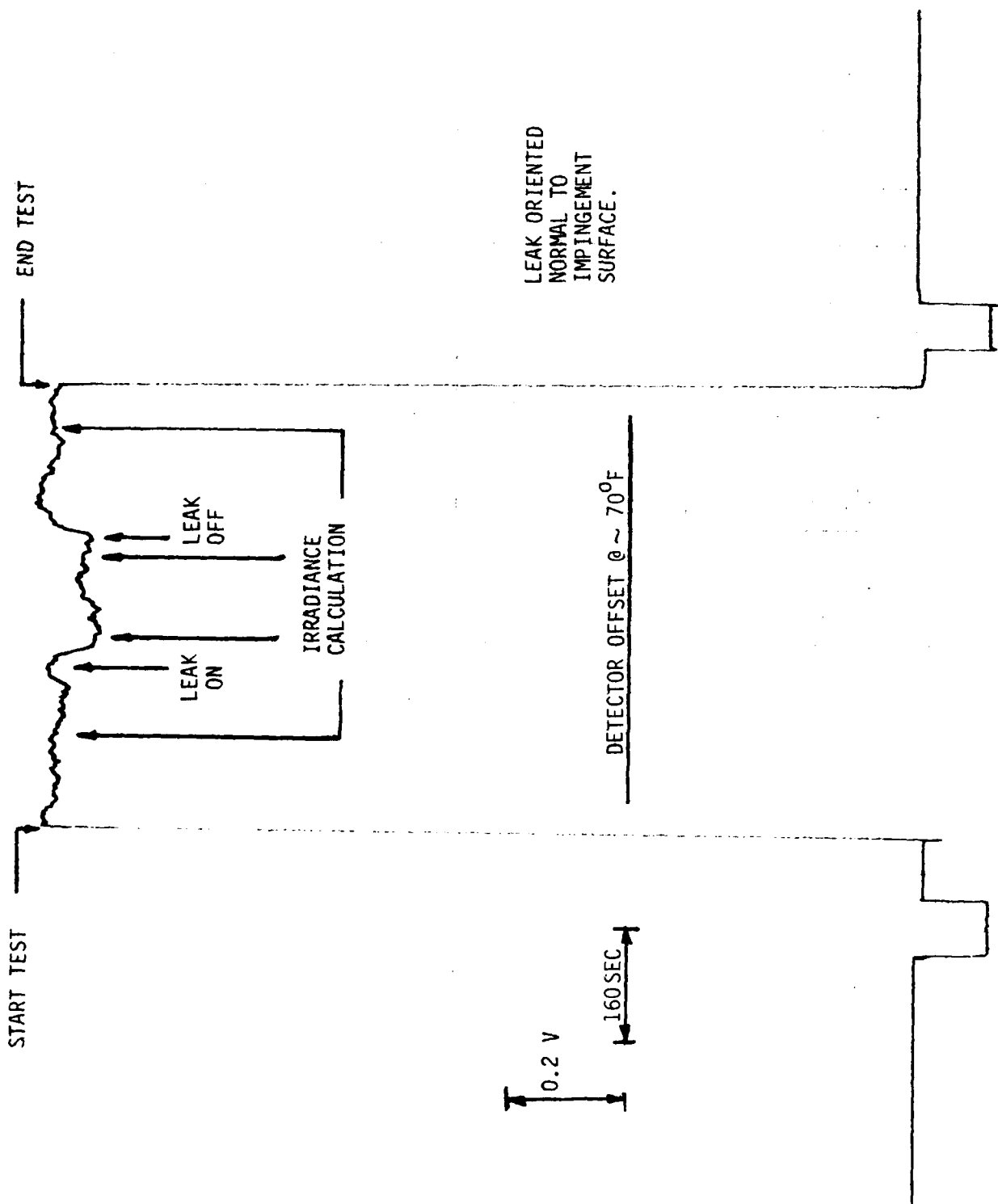
Figure C-20. Out of Channel 7 (9.597± 2.113 μm) for Test 3 (M=0.0)

135
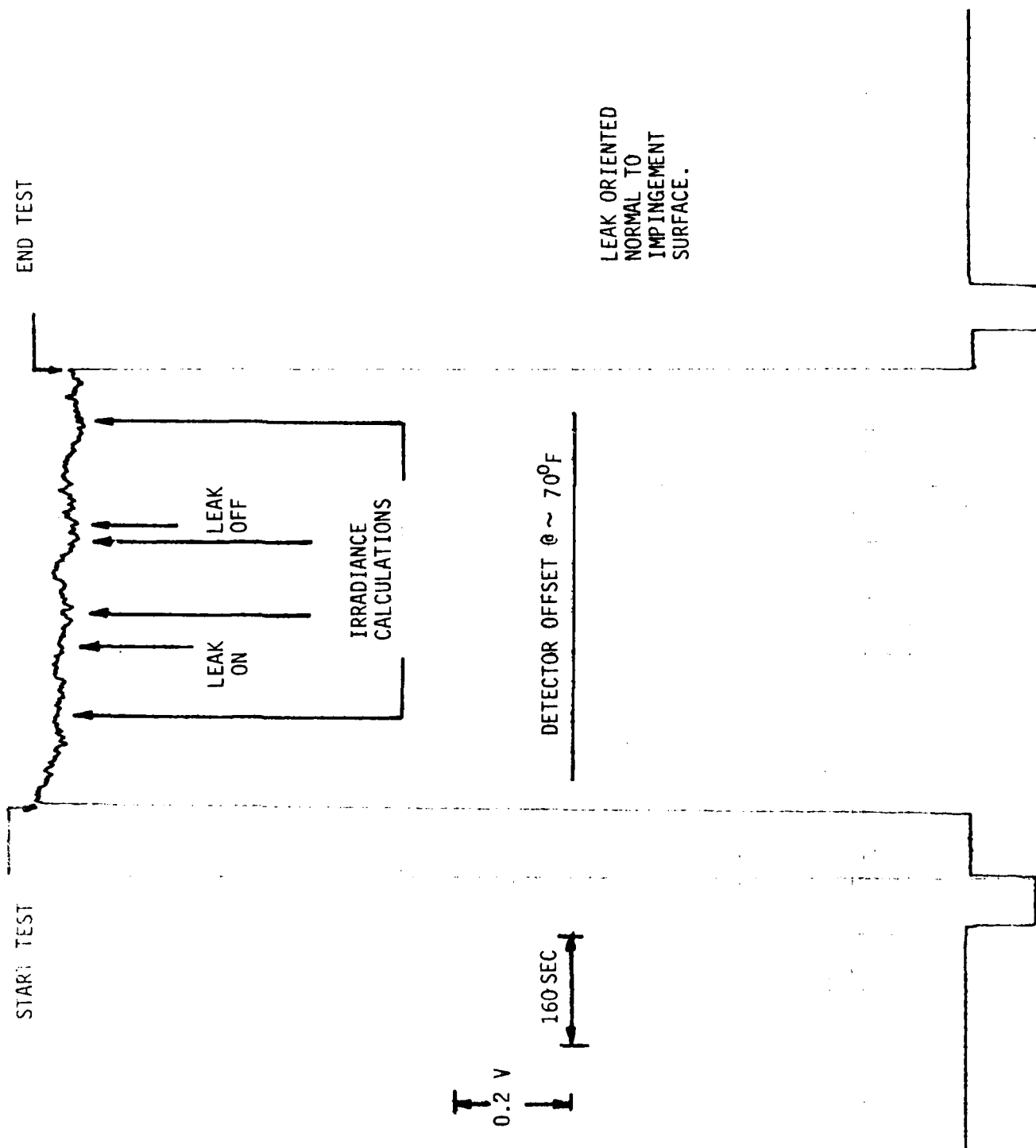
Figure C-21. Output of Channel 9 (4.745± .244 um) for Test 3 (M=0.0)

136
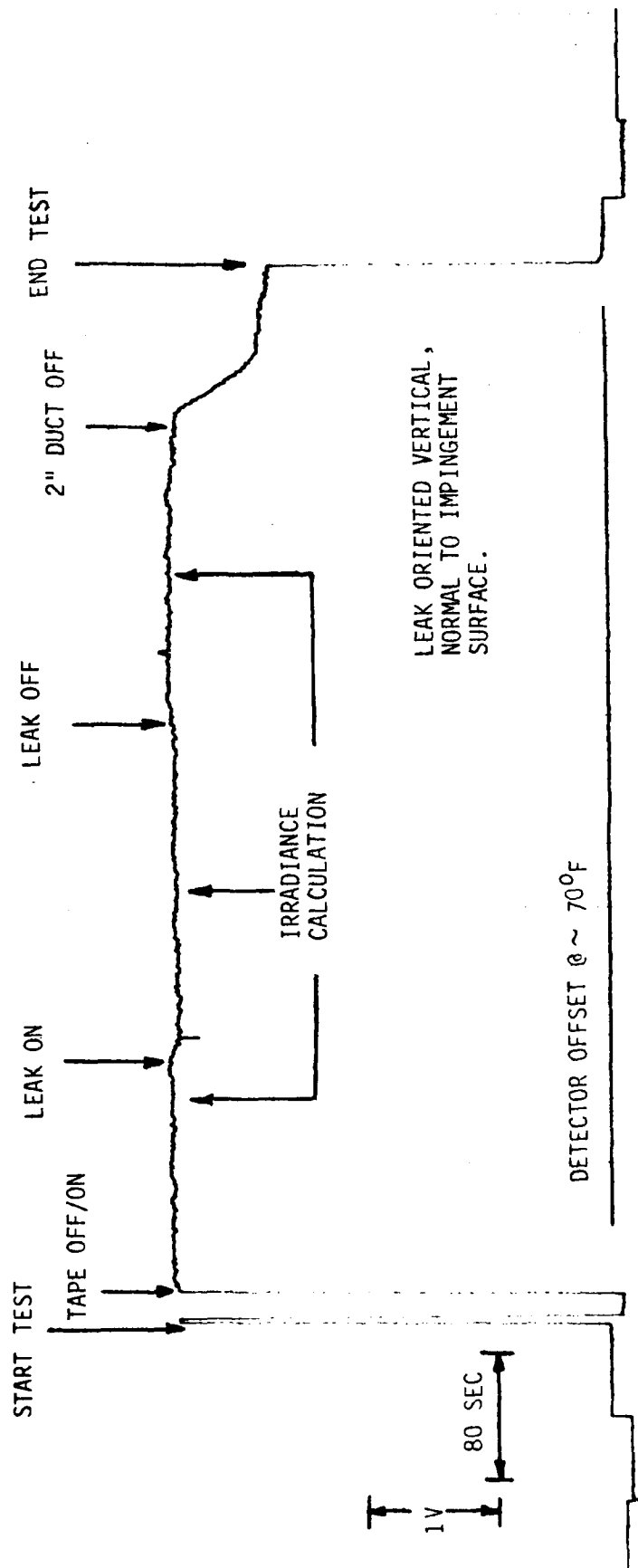
Figure C-22. Output of Channel 1 (Ge, 2-14 μm) for Test 3A (M=0.0)
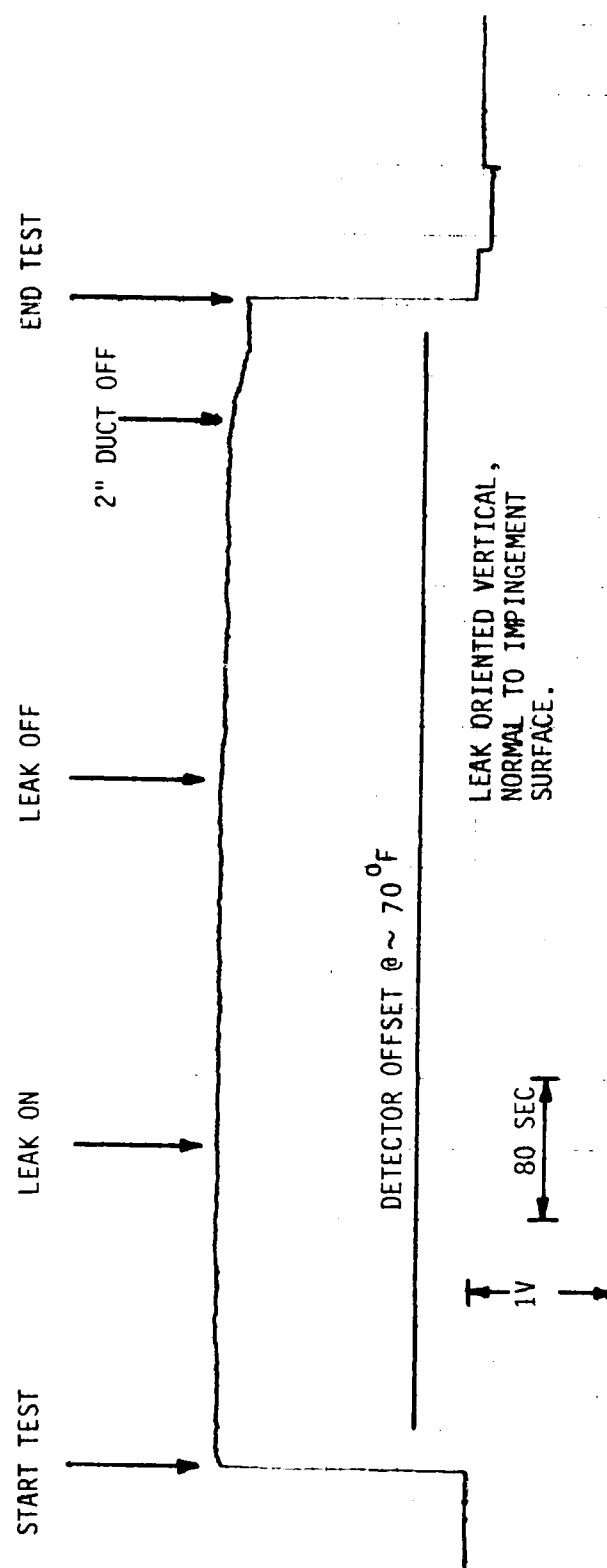
Figure C-23. Output of Channel 5 (3.690± .317 μm) for Test 3A (M=0.0)

START TEST
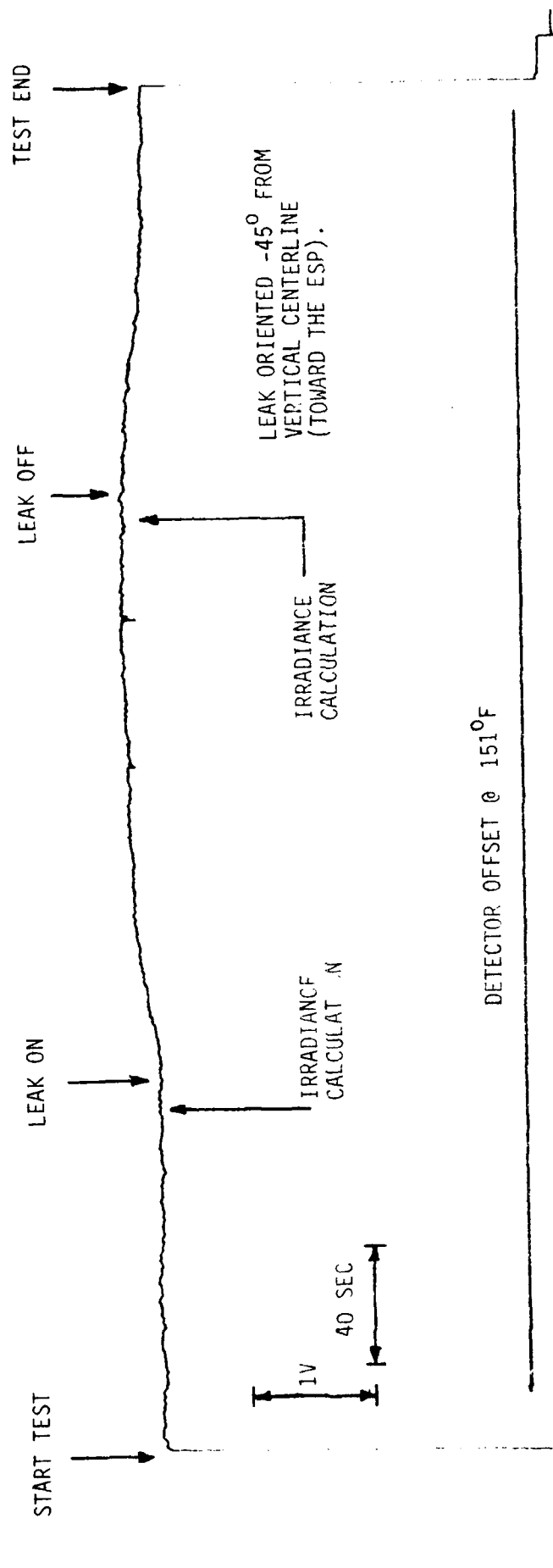
LEAK ON

LEAK OFF

2" DUCT OFF

END TEST

DETECTOR OFFSET @ ~ 70°F

LEAK ORIENTED VERTICAL, NORMAL TO IMPINGEMENT SURFACE.

80 SEC

1V
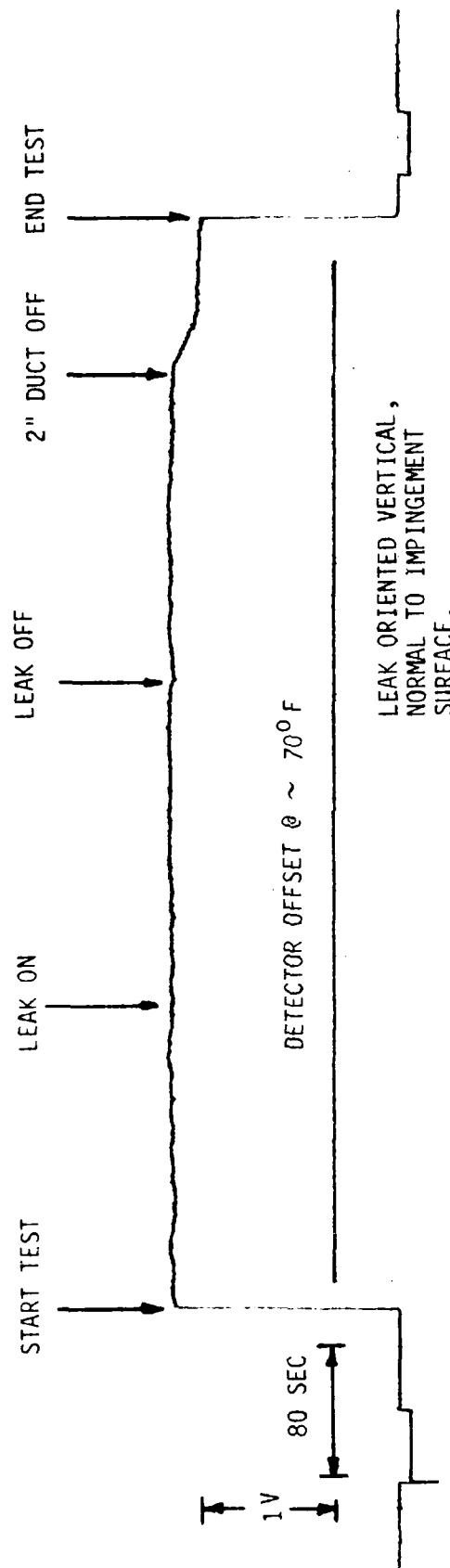
Figure C-24. Output of Channel 7 (9.597± 2.113 μm) for Test 3A (M=0.0)
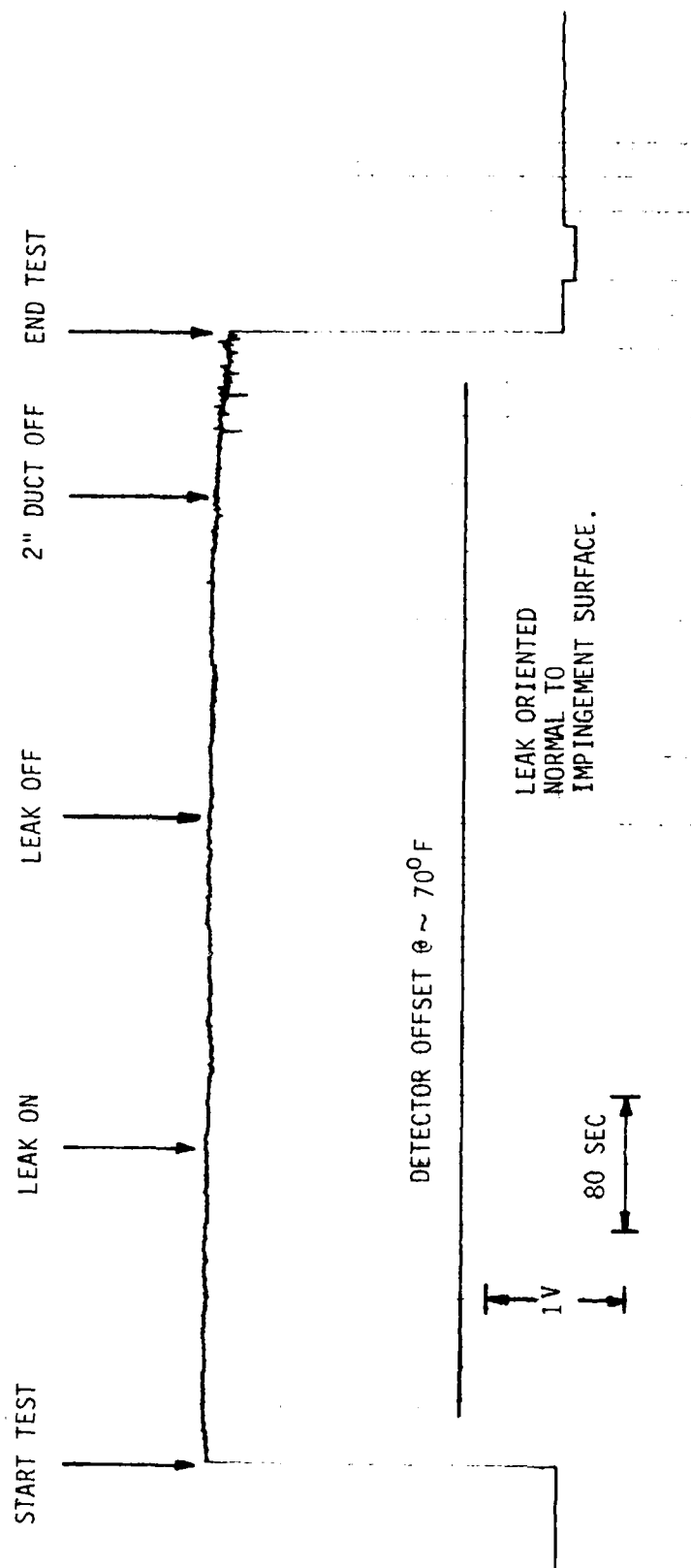
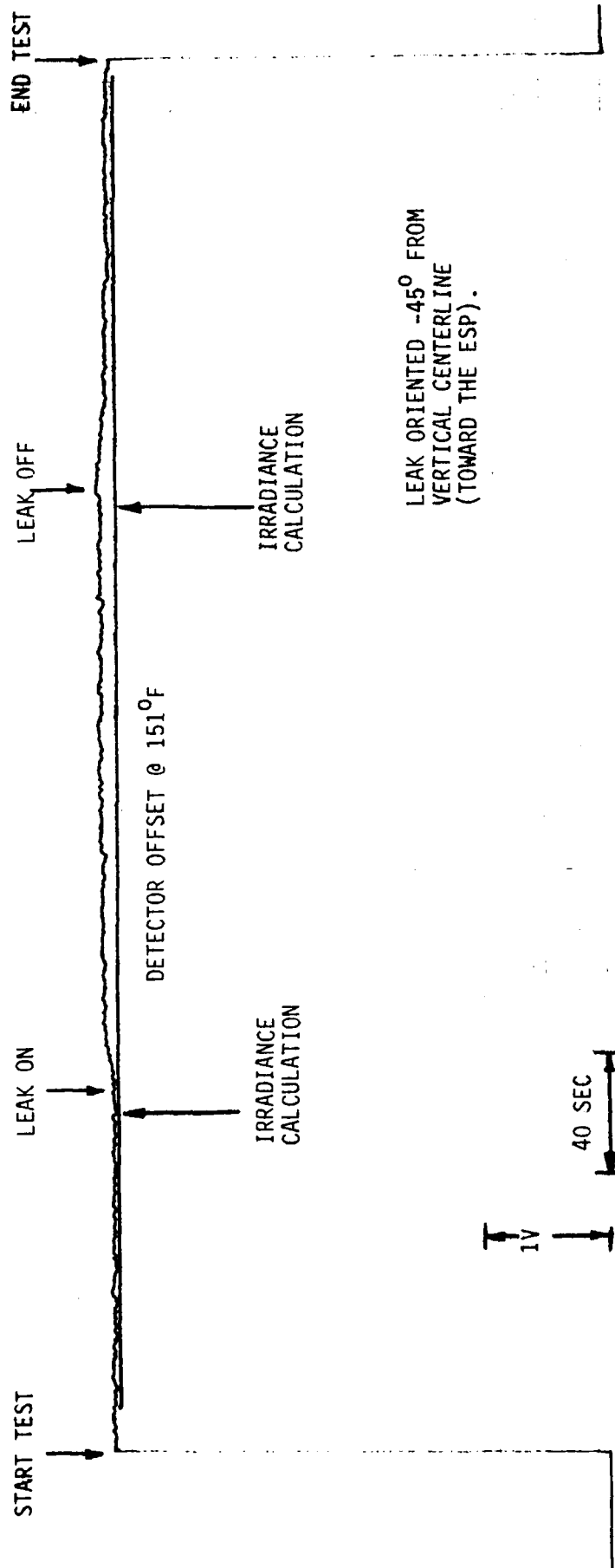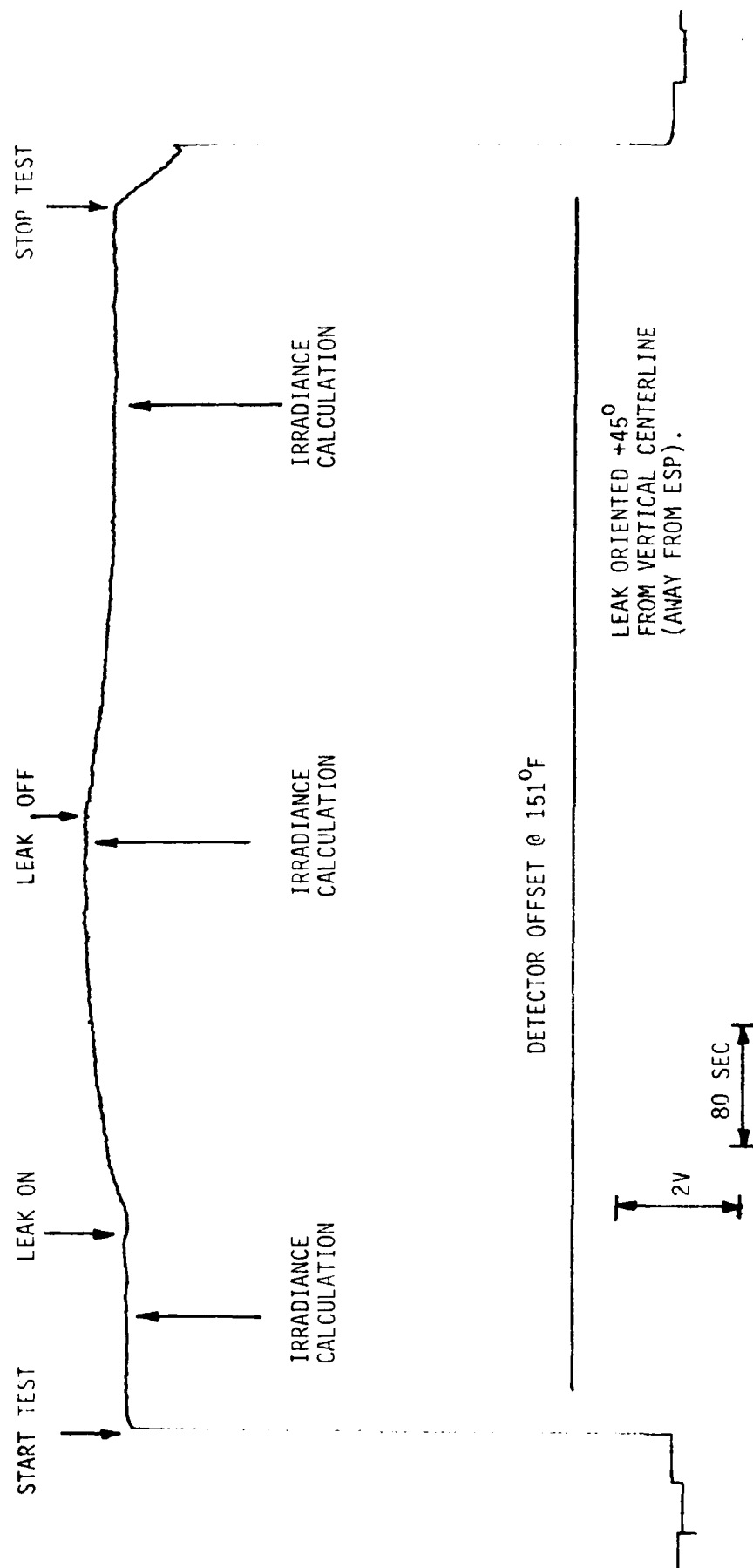Figure C-25. Output of Channel 9 (4.745± .244 μm) for Test 3A (M=0.0)

Figure C-26. Output of Channel 1 (Ge, 2-14 μm) for Test 4 (M=1.2)

START TEST

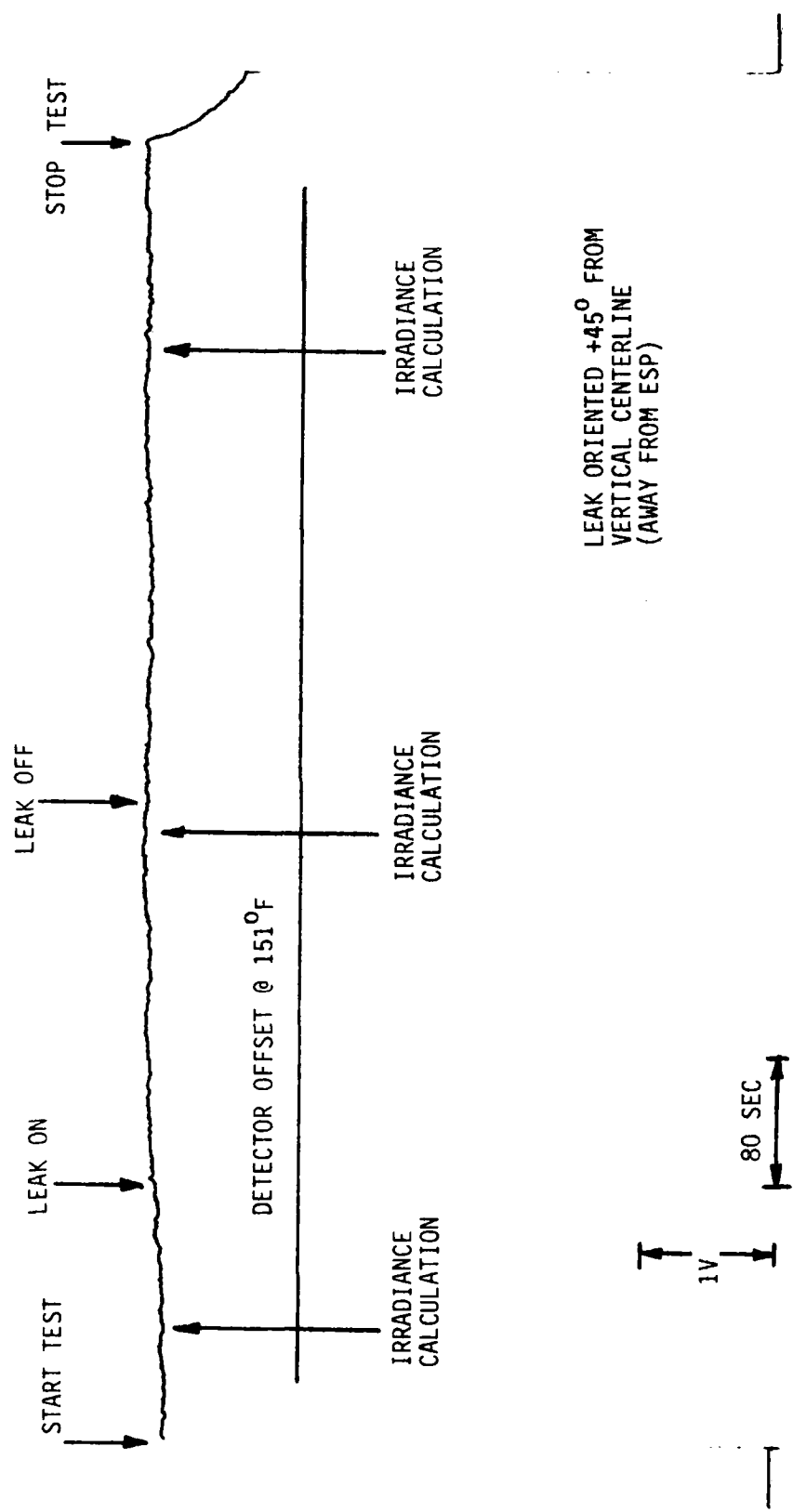PROBLEMS W/BLEED
TEMP.; STOP

RESTART

LEAK ON

IRRADIANCE
CALCULATION

LEAK OFF

IRRADIANCE
CALCULATION

END TEST

DETECTOR OFFSET @ 151°F

LEAK ORIENTED -45° FROM
VERTICAL CENTERLINE
(TOWARD THE ESP).

80 SEC

2V

Figure C-27. Output of Channel 5 (3.690+ .317 μm) for Test 4 (M=1.2)

142

Figure C-28. Output of Channel 7 (9.597±2.113μm) For Test 4

143
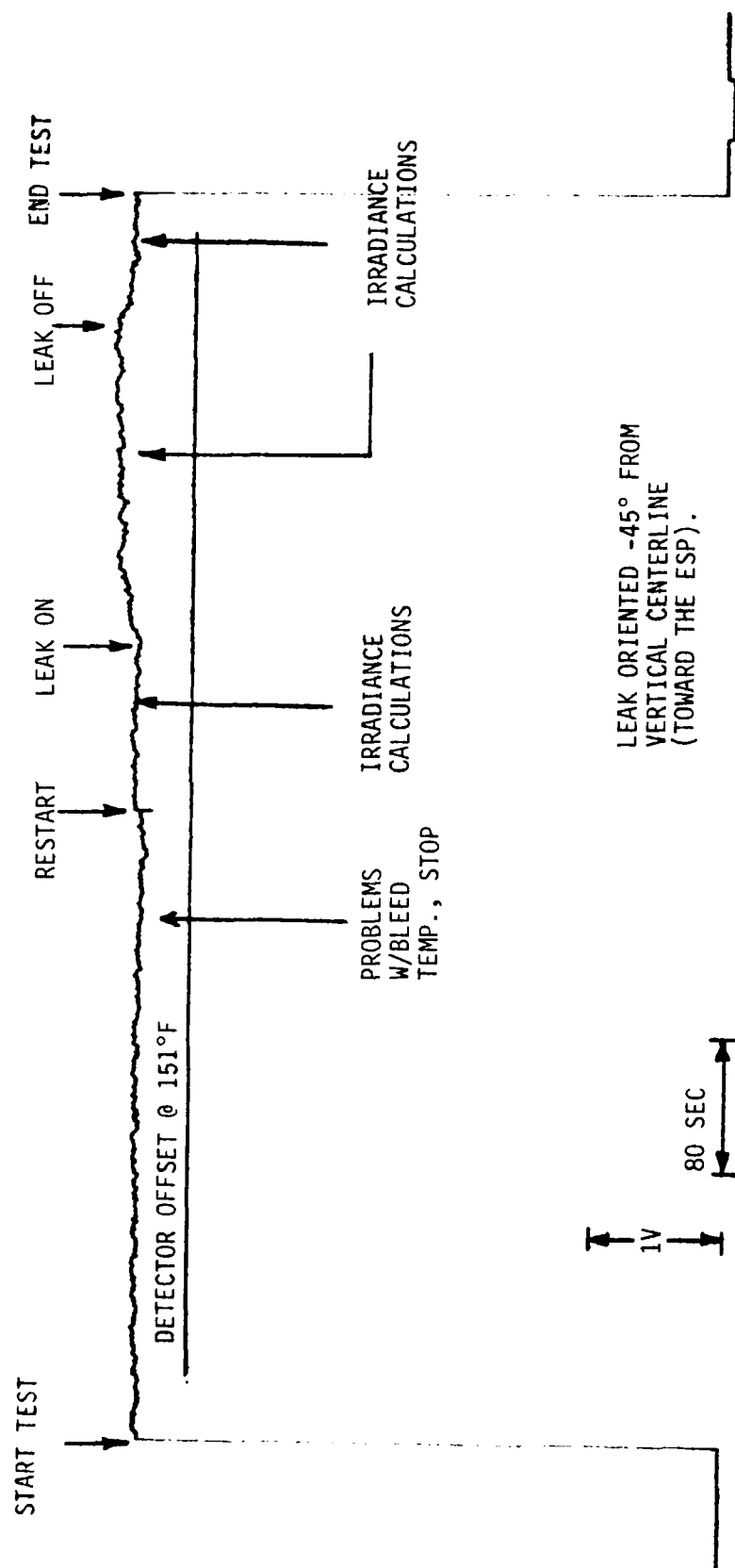
Figure C-29. Output of Channel 9 (4.745±.244 μm) for Test 4

START TEST

LEAK ON

IRRADIANCE
CALCULATION

LEAK OFF

END TEST

IRRADIANCE
CALCULATION

DETECTOR OFFSET VOLTAGE @ 151°F

LEAK ORIENTED -45° FROM
VERTICAL CENTERLINE
(TOWARD THE ESP).

2V

40 SEC
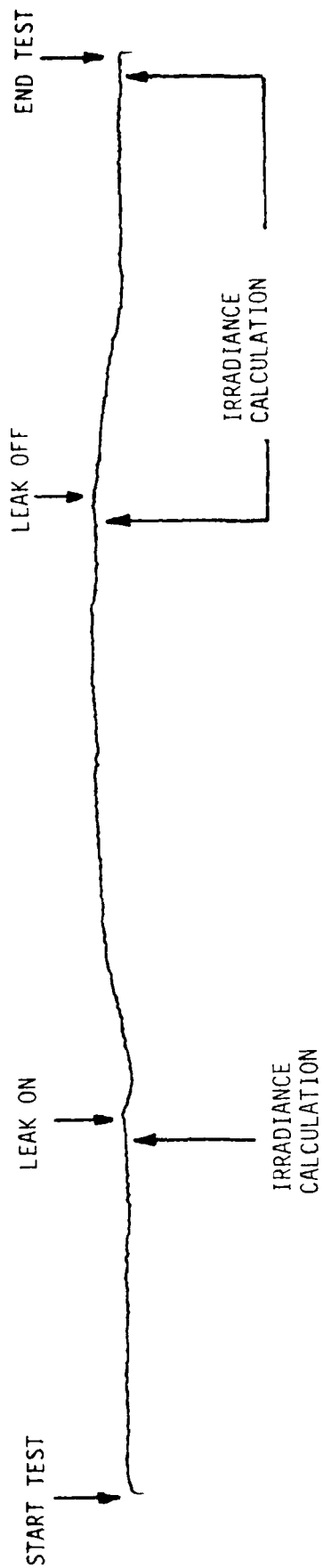
Figure C-30. Output of Channel 1 (Ge, 2-14 μm) for Test 4A (M=1.2)

145

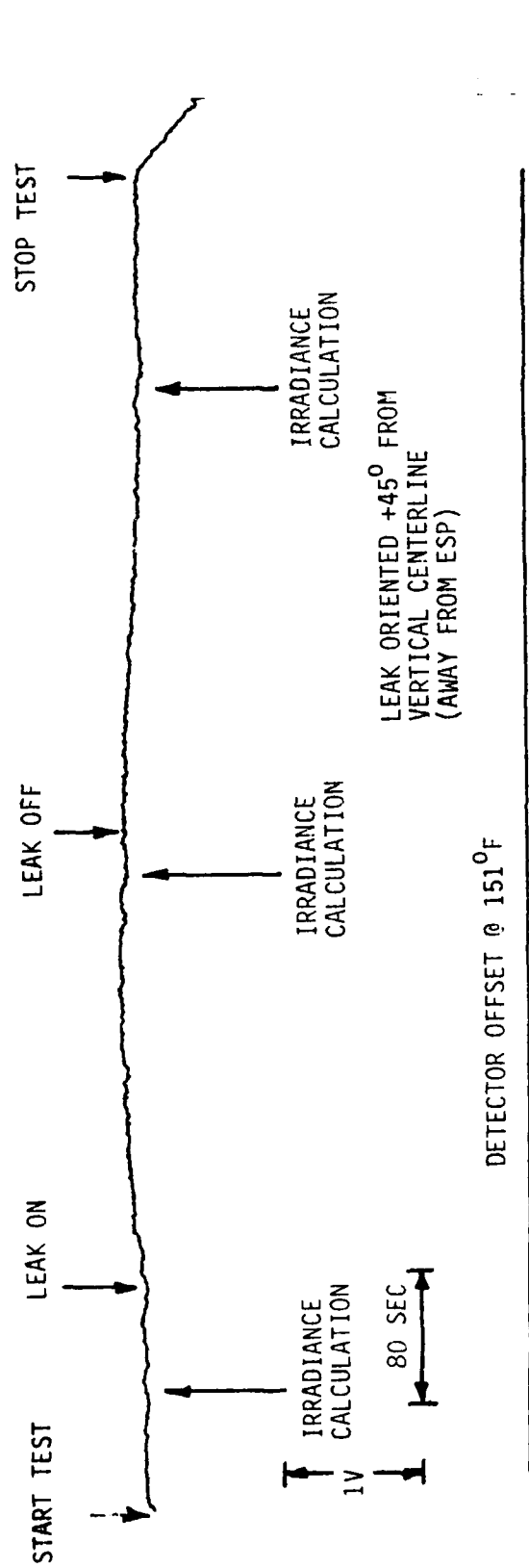Figure C-31. Output from Channel 5 (3.690± .317 μm) for Test 4A (M=1.2)

START TEST

LEAK ON

DETECTOR OFFSET @ 151°F

IRRADIANCE
CALCULATION

LEAK OFF

IRRADIANCE
CALCULATION

END TEST

LEAK ORIENTED -45° FROM
VERTICAL CENTERLINE
(TOWARD THE ESP).

40 SEC

1V

146

Figure C-32. Output of Channel 7 (9.597+ 2.113) for Test 4A (M=1.2)

Figure C-33. Output of Channel 9 (4.745± .244 μm) for Test 4A (M=1.2)

148

Figure C-34. Output of Channel 1 (Ge, 2-14 μm) for Test 7 (M=1.2)

Figure C-35. Output of Channel 5 (3.690± .317 μm) for Test 7 (M=1.2)

START TEST

LEAK ON

DETECTOR OFFSET @ 151°F

LEAK OFF

STOP TEST

IRRADIANCE CALCULATION

IRRADIANCE CALCULATION

IRRADIANCE CALCULATION

LEAK ORIENTED +45° FROM VERTICAL CENTERLINE (AWAY FROM ESP)

80 SEC

1V

150

Figure C-36. Output of Channel 7 (9.597+ 2.113 μm) for Test 7 (M=1.2)

151
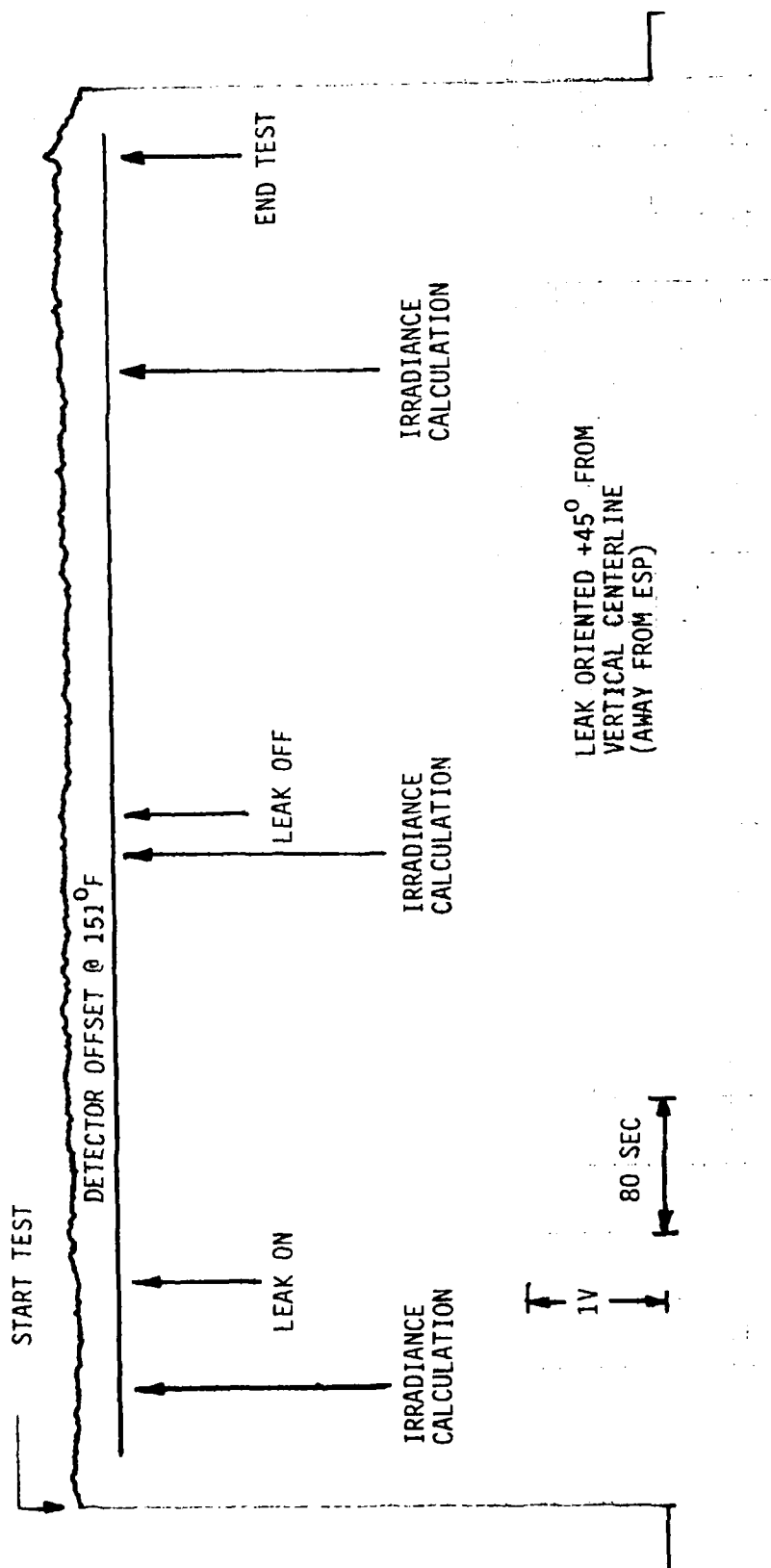
Figure C-37. Output of Channel 9 (4.745± .244 μm) for Test 7 (M=1.2)

APPENDIX D

ESP Detector Output Voltage Records
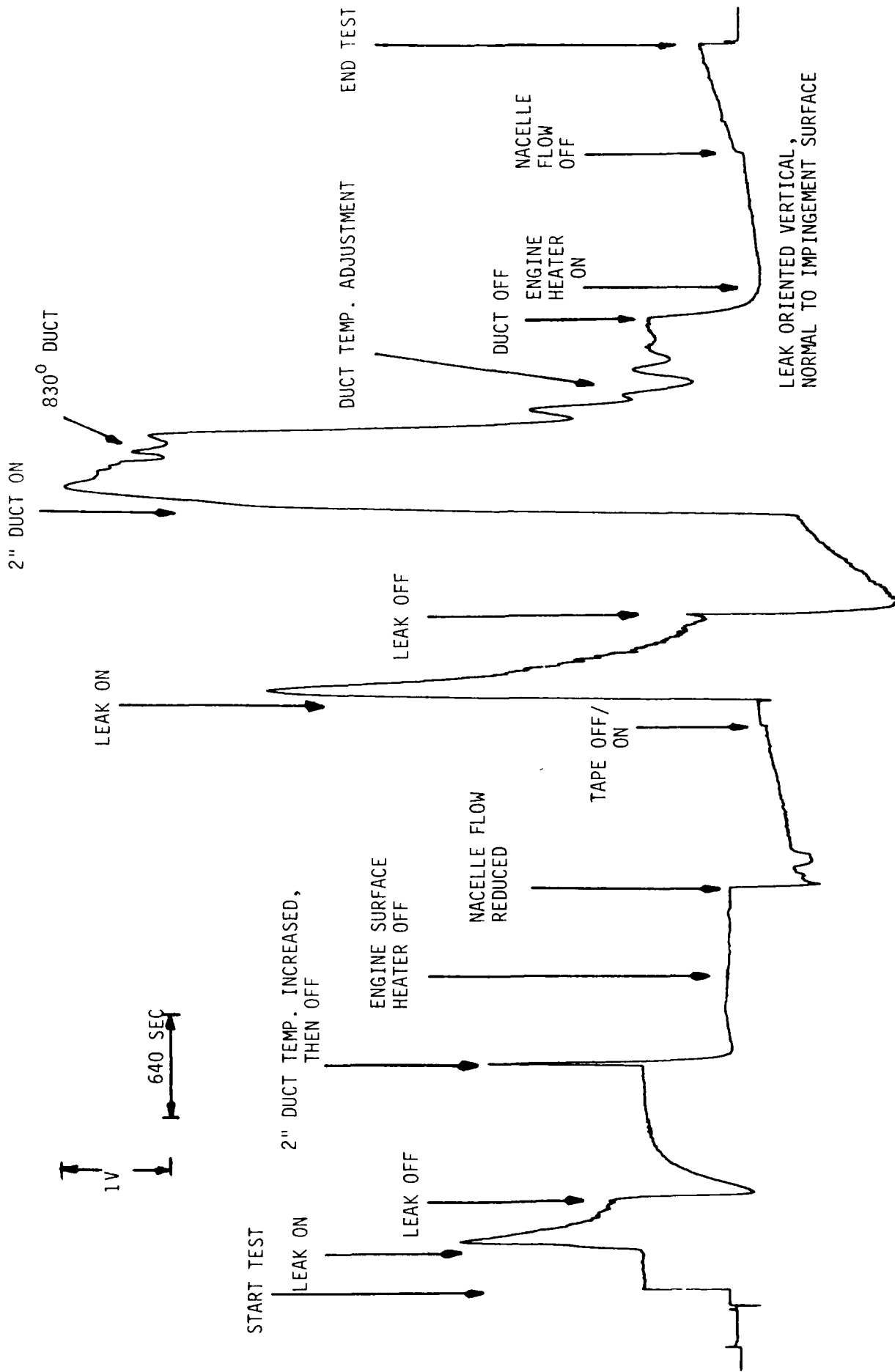
Figure D-1. Output of ESP (0.2 – 6 μm) for Tests 1D & 1E(M=1.2)

154
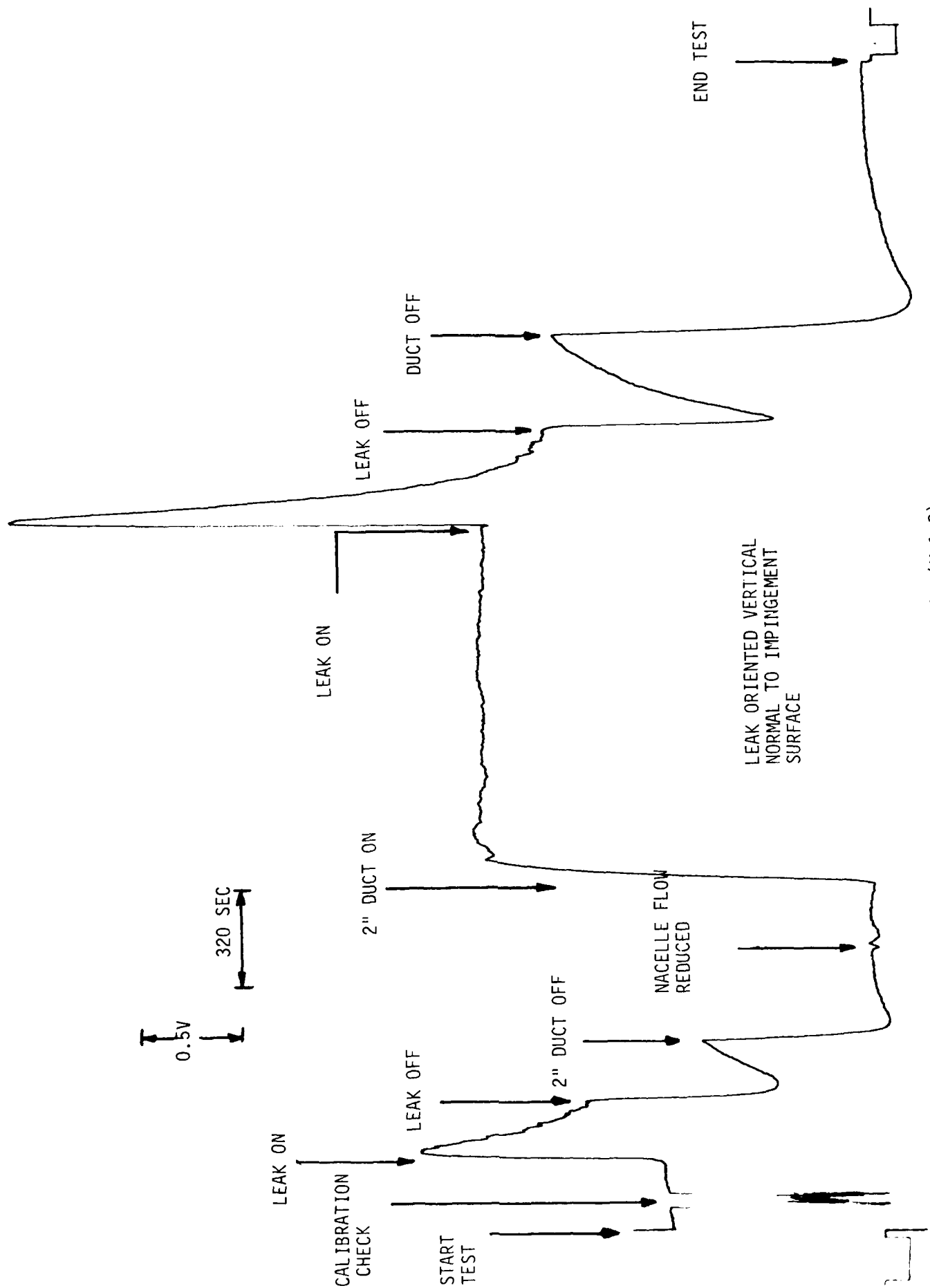
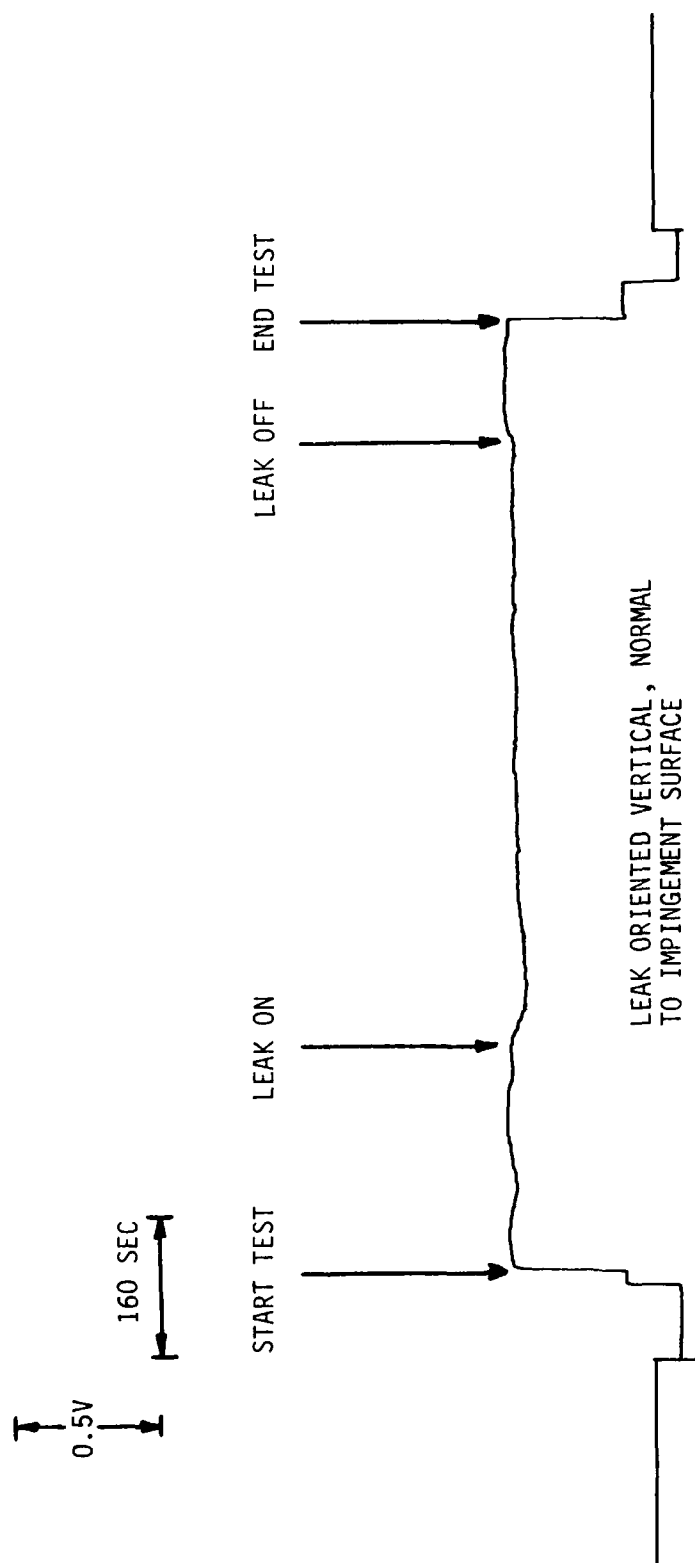Figure D-2. Output of ESP (0.2 - 6 μm) for Tests 1F & 1G (M=1.2)

155
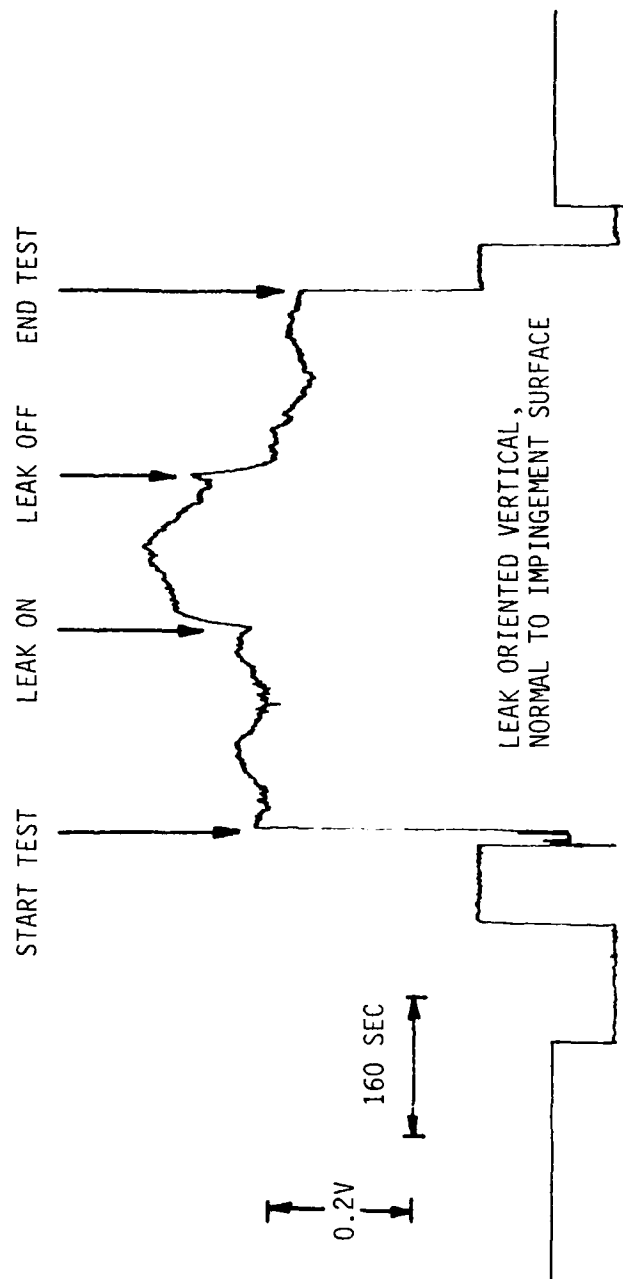
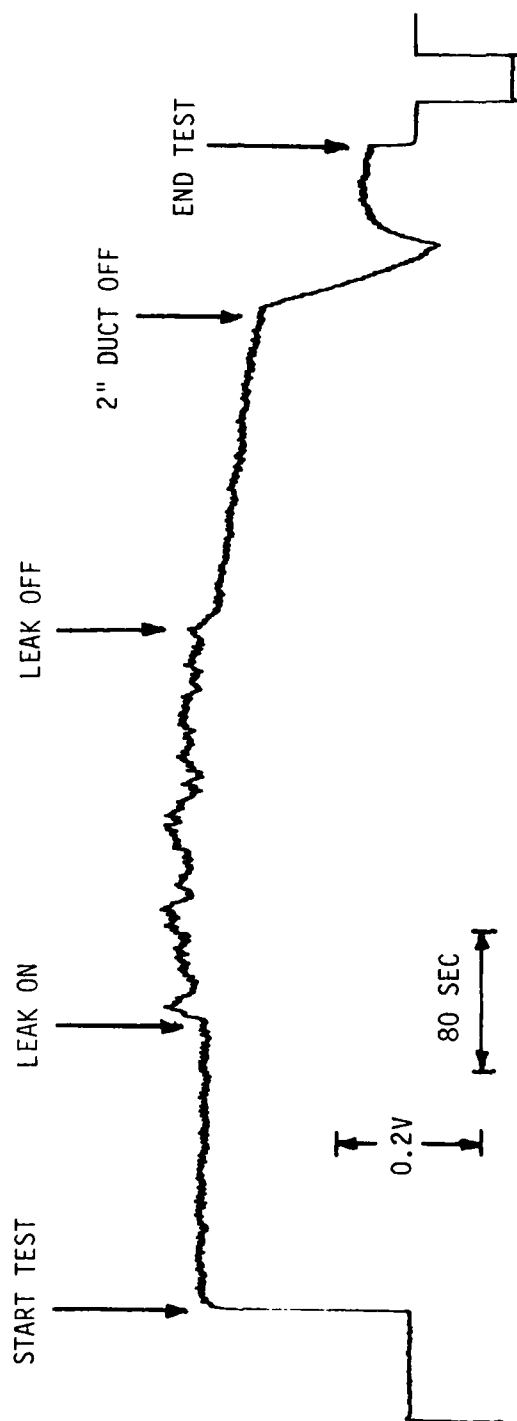Figure D-3. Output of ESP (0.2 - 6 μm) for Test 2 (M=0.75)

START TEST

LEAK ON

LEAK OFF

END TEST

160 SEC

0.5V

LEAK ORIENTED VERTICAL, NORMAL
TO IMPINGEMENT SURFACE

156

Figure D-4. Output of ESP (0.2 - 6 μm) for Test 3 (M=0.0)

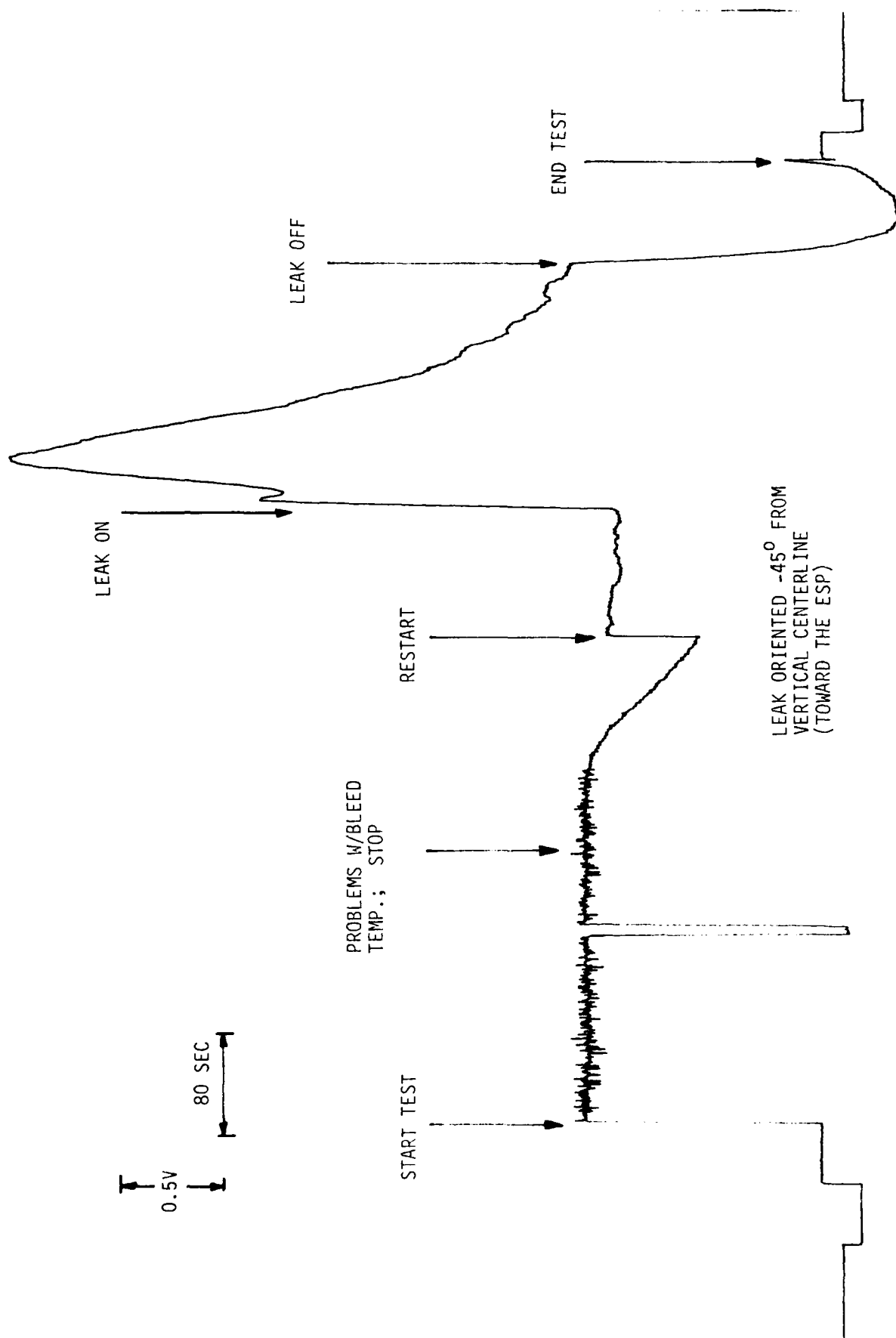Figure D-5. Output from ESP (0.2-6 μm) for Test 3A (M=0.0)

158

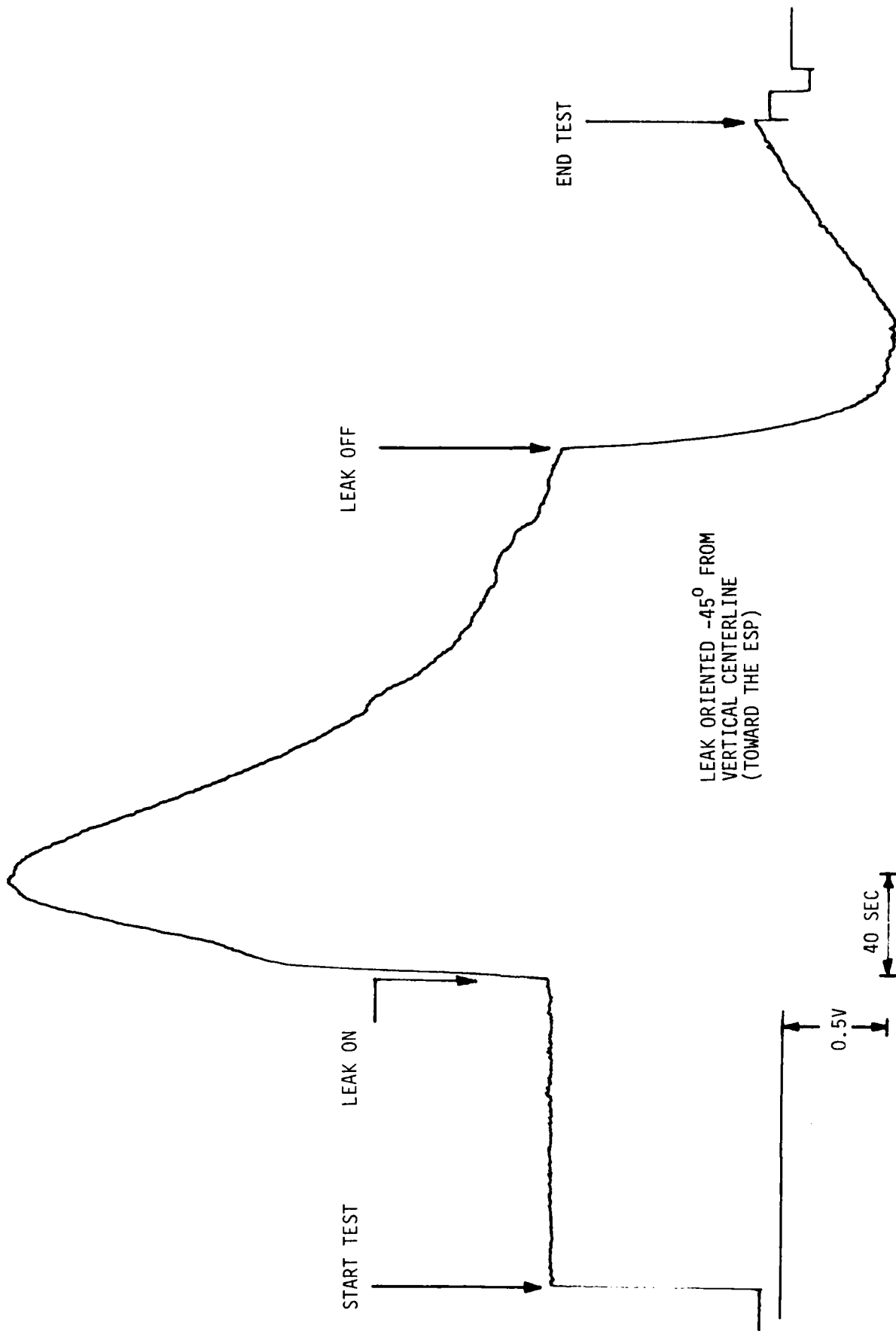Figure D-6. Output of ESP (0.2 - 6 μm) for Test 4 (M=1.2)

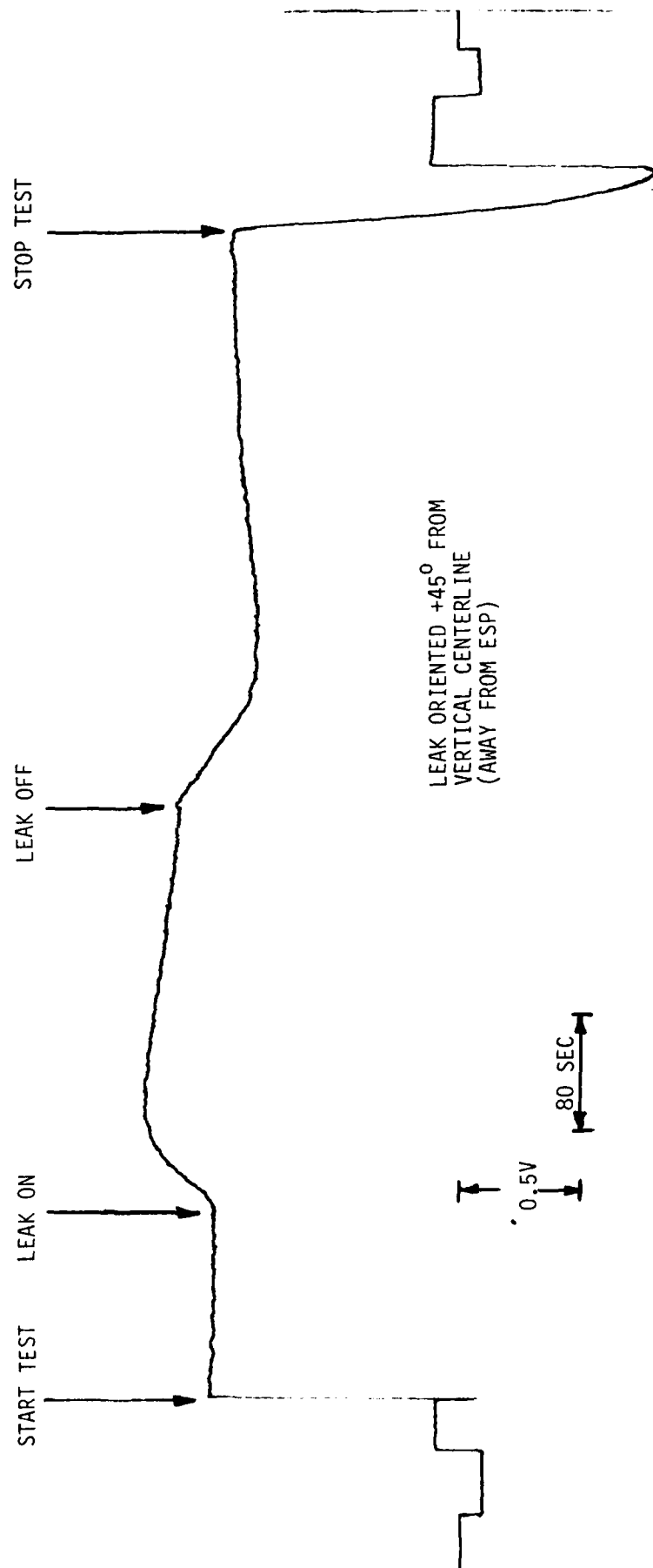Figure D-7. Output of ESP (0.2 - 6 μm) for Test 4A (M=1.2)

Figure D-8. Output of ESP (0.2 - 6 μm) for Test 7 (M=1.2)

STOP TEST

LEAK OFF

LEAK ORIENTED +45° FROM
VERTICAL CENTERLINE
(AWAY FROM ESP)

80 SEC

0.5V

LEAK ON

START TEST

☆U.S.Government Printing Office: 1986 — 748-061/60530

END

12-86

DTIC